UNIVERSITÉ DU LUXEMBOURG

PhD-FSTM-2022-83
The Faculty of Science, Technology and Medicine

DISSERTATION

Defense held on 27/07/2022 in Luxembourg

to obtain the degree of

DOCTEUR DE L'UNIVERSITÉ DU LUXEMBOURG

EN PHYSIQUE

by

Artem MALYEYEV
Born on 02 June 1989 in Simferopol (Ukraine)

MAGNETIC GUINIER LAW AND UNIAXIAL POLARIZATION ANALYSIS IN SMALL ANGLE NEUTRON SCATTERING

Dissertation defense committee

Dr Andreas Michels, dissertation supervisor
Professor, Université du Luxembourg

Dr Mael Guennou, Chairman
Professor, Université du Luxembourg

Dr Sebastian Mühlbauer, Vice Chairman
Heinz Maier-Leibnitz Zentrum (MLZ), Garching

Dr Daniele Brida
Professor, Université du Luxembourg

Dr Luis Fernandez Barquin
Professor, Universidad de Cantabria, Santander

Abstract

The present PhD thesis is devoted to the development of the use of the magnetic small-angle neutron scattering (SANS) technique for analyzing the magnetic microstructures of magnetic materials. The emphasis is on the three aspects: (i) analytical development of the magnetic Guinier law; (ii) the application the magnetic Guinier law and of the generalized Guinier-Porod model to the analysis of experimental neutron data on various magnets such as a Nd-Fe-B nanocomposite, nanocrystalline cobalt, and Mn-Bi rare-earth-free permanent magnets; (iii) development of the theory of uniaxial neutron polarization analysis and experimental testing on a soft magnetic nanocrystalline alloy.

The conventional "nonmagnetic" Guinier law represents the low-q approximation for the small-angle scattering curve from an assembly of particles. It has been derived for nonmagnetic particle-matrix-type systems and is routinely employed for the estimation of particle sizes in *e.g.*, soft-matter physics, biology, colloidal chemistry, materials science. Here, the extension of the Guinier law is provided for magnetic SANS through the introduction of the magnetic Guinier radius, which depends on the applied magnetic field, on the magnetic interactions (exchange constant, saturation magnetization), and on the magnetic anisotropy-field radius. The latter quantity characterizes the size over which the magnetic anisotropy field is coherently aligned into the same direction. In contrast to the conventional Guinier law, the magnetic version can be applied to fully dense random-anisotropy-type ferromagnets. The range of applicability is discussed and the validity of the approach is experimentally demonstrated on a Nd-Fe-B-based ternary permanent magnet and on a nanocrystalline cobalt sample.

Rare-earth-free permanent magnets in general and the Mn-Bi-based ones in particular have received a lot of attention lately due to their application potential in electronics devices and electromotors. Mn-Bi samples with three different alloy compositions were studied by means of unpolarized SANS and by very small-angle neutron scattering (VSANS). It turns out that the magnetic scattering of the Mn-Bi samples is determined by long-wavelength transversal magnetization fluctuations. The neutron data is analyzed in terms of the generalized Guinier-Porod model and the distance distribution function. The results for the so-called dimensionality parameter obtained from the Guinier-Porod model indicate that the magnetic

scattering of a $Mn_{45}Bi_{55}$ specimen has its origin in slightly shape-anisotropic structures and the same conclusions are drawn from the distance distribution function analysis.

Finally, based on Brown's static equations of micromagnetics and the related theory of magnetic SANS, the uniaxial polarization of the scattered neutron beam of a bulk magnetic material is computed. The theoretical expressions are tested against experimental data on a soft magnetic nanocrystalline alloy, and both qualitative and quantitative correspondence is discussed. The rigorous analysis of the polarization of the scattered neutron beam establishes the framework for the emerging polarized real-space techniques such as spin-echo small-angle neutron scattering (SESANS), spin-echo modulated small-angle neutron scattering (SEMSANS), and polarized neutron dark-field contrast imaging (DFI), and opens up a new avenue for magnetic neutron data analysis on nanoscaled systems.

Artem Malyeyev—Publication List

Entries marked with (*) are directly related to the present work.

2022

(*) Uniaxial polarization analysis of bulk ferromagnets: Theory and first experimental Results
A. Malyeyev, I. Titov, C. D. Dewhurst, K. Suzuki, D. Honecker, and A. Michels, *Journal of Applied Crystallography*, **2022** *55*
https://doi.org/10.1107/S1600576722003508

2021

Chemical vapor deposition of $CoFe_2O_4$ micropillar arrays with enhanced magnetic properties
B. Aspe, **A. Malyeyev**, A. Vakilinejad, K. Menguelti, A. Michels, and N. Bahlawane, *Journal of Alloys and Compounds*, **2021** *890*, 161758
https://doi.org/10.1016/j.jallcom.2021.161758

(*) Neutron study of magnetic correlations in rare-earth-free Mn-Bi magnets
A. Malyeyev, I. Titov, P. Bender, M. Bersweiler, V. Pipich, S. Mühlbauer, S. Ener, O. Gutfleisch, and A. Michels, *Physical Review Materials*, **2021** *5*, 034407
https://doi.org/10.1103/PhysRevMaterials.5.034407

2020

(*) Magnetic Guinier Law
A. Michels, **A Malyeyev**, I. Titov, D. Honecker, R. Cubitt, E. Blackburn, and K. Suzuki, *IUCrJ*, **2020** *7*, 136–142
https://doi.org/10.1107/S2052252519016439

2019

Evidence for the formation of nanoprecipitates with magnetically disordered regions in bulk $Ni_{50}Mn_{45}In_5$ Heusler alloys

G. Benacchio, I. Titov, **A. Malyeyev**, I. Peral, M. Bersweiler, P. Bender, D. Mettus, D. Honecker, E. P. Gilbert, M. Coduri, A. Heinemann, S. Mühlbauer, A. Cakir, M. Acet, and A. Michels, *Physical Review B*, **2019** *99*, 184422
http://dx.doi.org/10.1103/PhysRevB.99.184422

Microstructural-defect-induced Dzyaloshinskii-Moriya interaction

A. Michels, D. Mettus, I. Titov, **A. Malyeyev**, M. Bersweiler, P. Bender, I. Peral, R. Birringer, Y. Quan, P. Hautle, J. Kohlbrecher, D. Honecker, J. R. Fernández, L. F. Barquín, and K. L. Metlov, *Physical Review B*, **2019** *99*, 014416
http://dx.doi.org/10.1103/PhysRevB.99.014416

2014

Single Second Laser Annealed $CuInSe_2$ Semiconductors from Electrodeposited Precursors as Absorber Layers for Solar Cells

H. J. Meadows, A. Bhatia, V. Depredurand, J. Guillot, D. Regesch, **A. Malyeyev**, D. Colombara, M. A. Scarpulla, S. Siebentritt, and P. J. Dale, *The Journal of Physical Chemistry C*, **2014** *118*, 1451–1460
http://dx.doi.org/10.1021/jp409804s

Acknowledgements

First of all I would like to thank Prof. Dr. Andreas Michels, who gave me an opportunity to work on the forefront of science, with people from all over the world and for providing continuous advice and support.

Special thanks to Mael Guennou, Daniele Brida, Sebastian Mühlbauer and Luis Fernandez Barquin for being part of my defence jury.

I would like to thank all those that in one way or another helped me along the way, including but not limited to:

- all the members of the NanoMag group, current and former, without such nurturing environment my years here would have been much more difficult
- my family and friends, anything and everything I do depends heavily on your support
- Ivan Titov, for both scientific and life advice and continuous mentoring
- Oliver Gutfleisch, for pointing me to a larger picture on the enery transition. Without you, this project would have gone on a completely different route
- Semih Enner, for guiding me through the Mn – Bi preparation routines
- Dirk Honecker, for all your data I used, for all the instrumental and software know-how and for always fruitful discussions
- Astrid Tobias and all our administrative staff for being there when we needed them.

Finally, a special thanks to my best friend Tikaa, without you, I would have simply went crazy.

The financial and infrastructural support from the University of Luxembourg and National Research Fund of Luxembourg are gracefully acknowledged.

Table of contents

Nomenclature

Acronyms / Abbreviations

DMI Dzyaloshinskii–Moriya interaction

FT Fourier transform

SANS Small Angle Neutron Scattering

Greek Symbols and constants

μ_0 the permeability of free space also known as the vacuum permeability, $\mu_0 = 4\pi \times 10^{-7}$ Hm^{-1}, see section 2.5 for more details

μ_B the Bohr magneton, see section 2.5 for more details

$\mu_\mathbf{e}$ the magnetic dipole moment of the electron, see section 2.5 for more details

Δ the Laplace operator, the sum of all unmixed second partial derivatives

$\delta(\mathrm{r})$ the Dirac's delta function

δ_{kl} the Kronecker delta function, $\delta_{kl} = 0$ if $k \neq l$ and $\delta_{kl} = 1$ if $k = l$

$\hbar$ the reduced Plank's constant, $\hbar = \frac{h}{2\pi} \cong 1.055 \times 10^{-34}$ Js

Micromagnetics-specific Symbols

l_M the magnetostatic exchange length characterizing the competition between the exchange and magnetostatic interactions, defined as $l_\mathrm{M} = \sqrt{2A/(\mu_0 M_s^2)}$, see subsection 2.8.2 for more details

l_H the micromagnetic exchange length of the field characterizing the field-dependent size of perturbed regions around microstructural defects, defined as $l_\mathrm{M} = \sqrt{2A/(\mu_0 M_s H_i)}$, see subsection 2.8.2 for more details

l_{D} the micromagnetic exchange length of the DMI field, defined as $l_{\mathrm{D}} = 2D/(\mu_0 M_s^2)$, see subsection 2.8.2 for more details

A the exchange-stiffness constant, see subsection 2.8.2 for more details

D the DMI constant, see subsection 2.8.2 for more details

M_s the saturation magnetization, see subsection 2.8.2 for more details

H_{i} the internal magnetic field, $H_{\mathrm{i}} = H_0 - NM_s$ (N: demagnetizing factor), see subsection 2.8.2 for more details

M_0 the macroscopic saturation magnetization of the sample, $M_0 = V^{-1}\int_V M_{\mathrm{s}}(\mathbf{r})dV$, see subsection 2.8.2 for more details

$S_{\mathrm{H}}(\mathbf{q})$ the micromagnetic anisotropy-field scattering function, see subsection 2.11.1 and subsection 2.11.2 for more details

$S_{\mathrm{M}}(\mathbf{q})$ the micromagnetic longitudinal magnetization scattering function, see subsection 2.11.1 for more details

$R_{\mathrm{H}}(q,\theta,H_i)$ the dimensionless micromagnetic anisotropy-field response function, see subsection 2.11.1 and subsection 2.11.2 for more details

$R_{\mathrm{M}}(q,\theta,H_i)$ the dimensionless longitudinal magnetization response function, see subsection 2.11.1 for more details

$\mathbf{H}_{\mathrm{eff}}(\mathbf{r})$ the effective magnetic field, $\mathbf{H}_{\mathrm{eff}}(\mathbf{r}) = \mathbf{H}_0 + \mathbf{H}_{\mathrm{d}}(\mathbf{r}) + \mathbf{H}_{\mathrm{p}}(\mathbf{r}) + \mathbf{H}_{\mathrm{ex}}(\mathbf{r}) + \mathbf{H}_{\mathrm{DMI}}(\mathbf{r})$ see section 2.8 for more details

Neutron-specific symbols

m_n the neutron mass, $m_n = 1.675 \times 10^{-27}$ kg

μ_n the neutron's magnetic dipole moment, $\mu_n = -1.913\mu_{\mathrm{N}}$ (μ_{N} being the nuclear magneton)

μ_{N} the nuclear magneton, $\mu_{\mathrm{N}} = \frac{e\hbar}{2m_p} \cong 2.051 \times 10^{-27}$ JT^{-1}

$\mathbf{k}_0$ the wave vector of the incident neutron

$\mathbf{k}_1$ the wave vector of the scattered neutron

$\mathbf{q}$ the scattering vector, $\mathbf{q} = \mathbf{k}_0 - \mathbf{k}_1$

θ the scattering angle in the detector plane, see Figure 2.2 for more details

ψ the scattering angle in the forward direction (in the plane defined by $\mathbf{k}_0$ and $\mathbf{k}_1$), see Figure 2.2 for more details

Φ the incident beam flux, the number of neutrons per second per unit area perpendicular to the direction of neutron beam

$d\Omega$ the solid angle, $d\Omega = \sin\psi d\theta d\psi$

$\frac{d^2\sigma}{d\Omega dE'}$ the double differential scattering cross section, $\frac{d^2\sigma}{d\Omega dE'} = \frac{n'}{\Phi d\Omega dE'}$, see section 2.3 for more details

$\frac{d\sigma}{d\Omega}$ the differential scattering cross section, $\frac{d\sigma}{d\Omega} = \int_0^\infty (\frac{d^2\sigma}{d\Omega dE'})dE'$, see section 2.3 for more details

σ the total scattering cross section, $\sigma = \int_{4\pi}(\frac{d\sigma}{d\Omega})d\Omega$, see section 2.3 for more details

$\frac{d\Sigma}{d\Omega}$ the macroscopic SANS cross section, $\frac{d\Sigma}{d\Omega} = \frac{N}{V}\frac{d\sigma}{d\Omega}$

$V_{\text{nuc}}^{\text{int}}(\mathbf{r})$ the nuclear interaction pseudo-potential, see section 2.4 for more details

b the atomic scattering length, $b = b' - ib''$, where the real part b' can be both positive and negative and the imaginary part b'' describes the neutron capture or absorption by the given nucleus, see section 2.4 for more details

σ_{coh} the nuclear coherent scattering cross section, $\sigma_{coh} = 4\pi b_{coh}^2 = 4\pi\overline{b}^2$, see section 2.4 for more details

σ_{inc} the nuclear incoherent scattering cross section, $\sigma_{inc} = 4\pi b_{inc}^2 = 4\pi(\overline{b^2} - \overline{b}^2)$, see section 2.4 for more details

$\widetilde{N}(\mathbf{q})$ the Fourier Transform of scattering-length density $N(\mathbf{r})$, see section 2.4 for more details

$V_{\text{mag}}^{\text{int}}$ the magnetic interaction potential, see section 2.5 for more details

$\mathbf{M}(\mathbf{r})$ the magnetization vector field, see section 2.5 for more details

$\widetilde{Q}(\mathbf{q})$ the Halpern-Johnson (magnetic interaction) vector defined as $\widetilde{\mathbf{Q}} = \hat{\mathbf{q}}\left(\hat{\mathbf{q}}\cdot\widetilde{\mathbf{M}}\right) - \widetilde{\mathbf{M}}$, see subsection 2.5.1 for more details

$\frac{d\Sigma_{\text{tot}}}{d\Omega}$ the total unpolarized SANS cross section, $\frac{d\Sigma_{\text{tot}}}{d\Omega} = \frac{d\Sigma_{\text{nuc}}}{d\Omega} + \frac{d\Sigma_{\text{mag}}}{d\Omega}$, see section 2.6 for more details

$\frac{d\Sigma_{\text{nuc}}}{d\Omega}$ the nucleat unpolarized SANS cross section, $\frac{d\Sigma_{\text{nuc}}}{d\Omega} = \frac{8\pi^3}{V}|\widetilde{N}(\mathbf{q})|^2$, see section 2.6 for more details

$\frac{d\Sigma_{\text{mag}}}{d\Omega}$ the magnetic unpolarized SANS cross section, $\frac{d\Sigma_{\text{mag}}}{d\Omega} = \frac{8\pi^3}{V}b_H^2|\widetilde{Q}(\mathbf{q})|^2$, see section 2.6 for more details

List of figures

List of tables

Chapter 1

Introduction

Small-angle neutron scattering (SANS) is one of the most important techniques for microstructure determination, since it allows the investigation of both microstructural (chemical) and magnetic inhomogeneities in the *volume* of materials on a *mesoscopic length scale* between a few and a few hundred nanometers. SANS provides statistically-averaged information about a large number of scattering objects, in contrast to *e.g.*, electron-microscopy-based imaging methods. Figure 1.1 gives an overview on the microstructural size regimes which are accessible through various observational methods. When conventional SANS is combined with so-called ultra or very small-angle neutron scattering (USANS or VSANS) the spatial resolution can be extended up to the micrometer range [53, 52]. This is an important size regime in which many macroscopic material properties are realized. The standard references for nonmagnetic SANS and its x-ray counterpart, small-angle x-ray scattering (SAXS), are the well-known textbooks by Guinier and Fournet [36], Glatter and Kratky [32], Feigin and Svergun [27], Svergun, Koch, Timmins, and May [121], and by Gille [30]. Michels [79] has recently provided a detailed exposition of magnetic SANS; see also the recent review [92] for many examples, which highlight the versatility of the magnetic SANS technique for the study of a wide range of magnetic materials.

In this thesis, the focus is exclusively on the so-called "diffuse" magnetic SANS, *i.e.*, with magnetic neutron scattering at small scattering angles around the forward direction arising from quasi-non-periodic, continuous long-wavelength magnetization fluctuations (compare panel (A1) on the Figure 1.2). The term "diffuse magnetic SANS" is used here to distinguish it from the magnetic small-angle diffraction, which is the method of choice for investigating long-range-ordered periodic structures such as helical spin systems, spin-density waves, flux-line lattices in superconductors, or the recently discovered skyrmion crystals (compare panel (A2) on Figure 1.2) [92]. Since in "diffuse" experiments the wavelength of the incident neutrons is typically much larger than the Bragg cutoff of the material, the discrete atomic

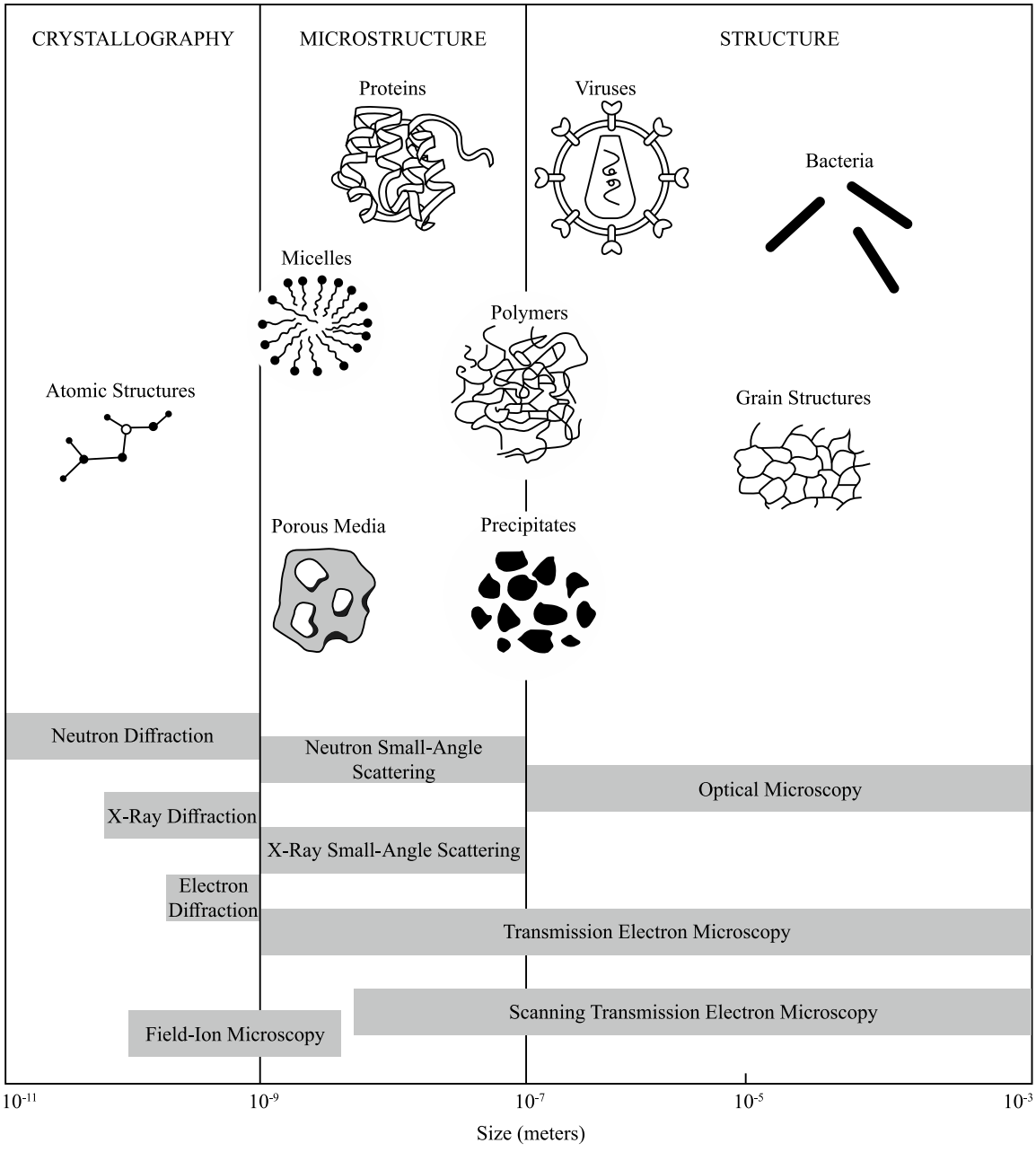

Fig. 1.1 Microstructural size regimes accessible by different observational methods. The techniques range from neutron diffraction, which is used to investigate atomic structures, to optical microscopy, which can be employed to image macroscopic objects such as bacteria or crystalline grain structures. Image courtesy of Roger Pynn, Indiana University, Bloomington, USA. Taken from [107, 79].

structure of matter is generally of no relevance for SANS. Therefore, diffuse magnetic SANS can be described within a *continuum approach*, where the three-dimensional magnetization

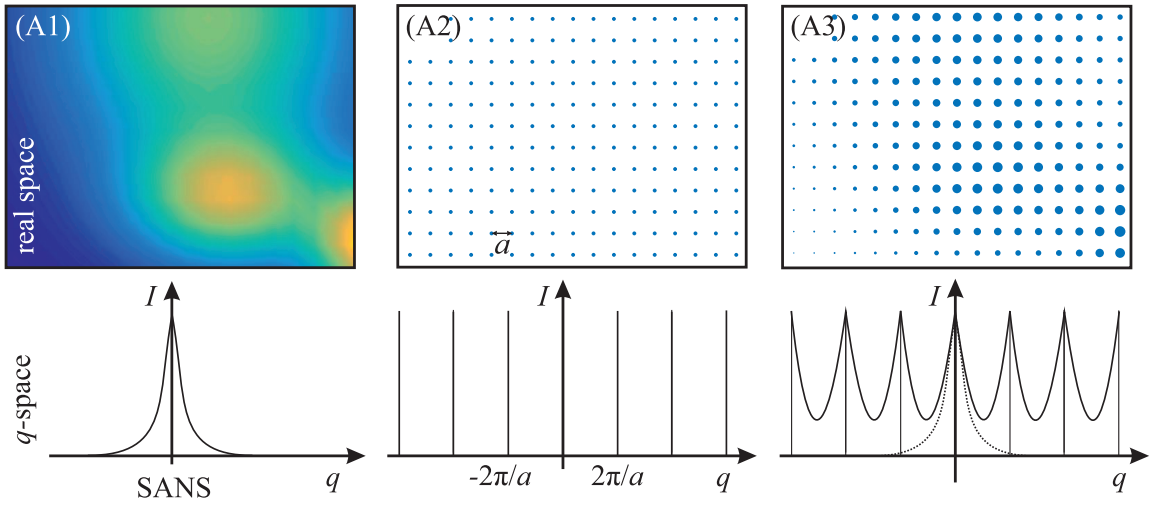

Fig. 1.2 Schematic illustration of the transformation from real space to reciprocal space for a smooth texture (A1), a discrete lattice with lattice spacing a (A2), and a smooth incommensurate modulation on top of a discrete lattice (A3). Image courtesy of Sebastian Mühlbauer, Technische Universität München, Germany. Taken from [107, 79].

vector field of the sample, $\mathbf{M}(\mathbf{r})$, is the relevant quantity that determines the elastic magnetic SANS cross section.

In [79], the theoretical framework for magnetic SANS has been established in terms of the continuum theory of micromagnetics. Micromagnetism is a mesoscopic phenomenological theory that in its quasi-static version is designed to compute the equilibrium magnetization state of an arbitrarily-shaped ferromagnetic body, provided the applied magnetic field, the geometry of the ferromagnet, and all the materials parameters are known [11, 2, 62]. Analytical expressions for the magnetic SANS cross section are provided in [79], which permit the analysis of the magnetic interactions, *e.g.*, the exchange-stiffness constant, the strength and spatial structure of the magnetic anisotropy field and of the magnetostatic field, and the field dependence of magnetic correlations. One central result of the present thesis – the magnetic Guinier law – has emerged from the desire to find a low-q approximation for the expression of the magnetic SANS cross section (at small scattering angles) [83], similar to the well-known "conventional" Guinier law in nonmagnetic SANS and SAXS, which allows for the quick determination of the particle size in the initial stages of the data analysis. This represents a fundamental result in magnetic neutron scattering theory. The derived magnetic Guinier law and the so-called generalized Guinier-Porod law have then also been experimentally tested on nanocrystalline Cobalt and on a rare-free Mn-Bi compound [72], which is a promising material for permanent-magnet applications. The second central result of this thesis – development and experimental testing of uniaxial polarization analysis proce-

dures [73] – is motivated by recent advances in neutron instrumentation, more specifically by the development of efficient ^{3}He spin filters [4, 101, 98], and by the concomitant availability of such polarization capabilities at neutron facilities worldwide. The polarization of the scattered neutron beam can be analyzed in terms of the micromagnetic theory and allows for the determination of magnetic interaction parameters.

Besides [79], this thesis largely relies on [83, 72, 73], which constitute the main results. The thesis is organized as follows: in chapter 2, the basic properties of the neutron are discussed and the expressions for the elastic nuclear (nonmagnetic) and magnetic neutron scattering cross sections, are established. Both the distinctness of SANS from conventional particle scattering and the origins of magnetic SANS are discussed, and the expressions for the magnetization Fourier components are linked to the micromagnetic theory. This results in a closed-form expression for the SANS cross section, which allows for a quantitative analysis of experimental data.

Chapter 3 discusses the magnetic Guinier law [83]. Small-angle scattering of X-rays and neutrons is a routine method for the determination of nanoparticle sizes. The conventional (nonmagnetic) Guinier law represents the low-q approximation for the small-angle scattering curve from an assembly of particles. The Guinier law has originally been derived for nonmagnetic particle-matrix-type systems and it is successfully employed for the estimation of particle sizes in various scientific domains. An important prerequisite for it to apply is the presence of a discontinuous interface separating particles and matrix. In this chapter, the Guinier law is introduced for the case of *magnetic* SANS and its applicability is experimentally demonstrated on the nanocrystalline cobalt sample. It is well known that the magnetic microstructure of nanocrystalline ferromagnets is highly nonuniform on the nanometre length scale and is characterized by a spectrum of continuously varying long-wavelength magnetization fluctuations, *i.e.*, these systems do not manifest sharp interfaces in their magnetization profile. The introduced quantity of the magnetic Guinier radius depends on the applied magnetic field, on the magnetic interactions (exchange, magnetostatics) and on the magnetic anisotropy-field radius, which characterizes the size over which the magnetic anisotropy field is coherently aligned into the same direction. In contrast to the nonmagnetic conventional Guinier law, the magnetic version can be applied to fully dense random-anisotropy-type ferromagnets.

Chapter 4 employs the generalized Guinier-Porod model to experimentally investigate a promising permanent magnet material [72]. More specifically, the results of an unpolarized VSANS study on Mn-Bi-based rare-earth-free permanent magnets are reported here. For this material, the magnetic SANS cross section is dominated by long-wavelength transversal magnetization fluctuations, and has been analyzed in terms of the Guinier-Porod model

and the distance distribution function. This provides the radius of gyration which, in the remanent state, ranges between about $220-240\,\mathrm{nm}$ for the three different alloy compositions investigated. Moreover, computation of the distance distribution function, in conjunction with results for the so-called *s* parameter obtained from the Guinier-Porod model, indicates that the magnetic scattering of a $Mn_{45}Bi_{55}$ sample has its origin in shape-anisotropic structures.

Chapter 5 is concerned with the development of the uniaxial polarization analysis technique, as it can be implemented on a SANS instrument [73]. Based on the solution of Brown's static equations of micromagnetics (see chapter 2), the uniaxial polarization of the neutron beam scattered off a bulk magnetic material is computed. The micromagneic approach takes into account the isotropic exchange interaction, the antisymmetric Dzyaloshinskii-Moriya interaction, magnetic anisotropy, the dipole-dipole interaction, as well as the effect of an applied magnetic field. In the high-field limit, the solutions for the magnetization Fourier components are used to obtain closed-form results for the spin-polarized SANS cross sections and the ensuing polarization. The theoretical expressions are compared to experimental data on a soft magnetic nanocrystalline alloy. Thus, a general framework for polarized real-space neutron methods is provided, and this approach may open up a new avenue for magnetic neutron data analysis on magnetic microstructures.

Finally, chapter 6 summarizes the main findings of this thesis and provides an outlook into future challenges.

Chapter 2

Theory of Magnetic Neutron Scattering

This chapter provides an overview of the theory of neutron scattering in general and magnetic small angle neutron scattering (SANS further) in particular. It aims to be self-sufficient, but the reader requiring more details is directed to: a summary lecture on neutrons and magnetism [25], recent reviews on magnetic neutron scattering [78, 92] or a recently published book dedicated to the subject [79] in order of the increasing detail.

2.1 Why neutrons?

Neutrons' particular interest as a probe arise from their key properties: mass, zero net electrical charge and spin angular momentum.

The value of the neutron mass of $m_n = 1.675 \times 10^{-27}$ kg results in the de Broglie wavelength on the order of interatomic distances in many crystaline and liquid materials, thus it allows to access the *structure of matter*. Moreover, the typical velocity of the research neutrons results in energy on the order of elementary excitations in solids, thus, *dynamic features* can be explored too – via the study of inelastic scattering which is beyond the scope of this work.

The spin angular momentum of the neutron $S = \pm\frac{1}{2}\hbar$ brings with it the associated magnetic dipole moment $\mu_n = -1.913\mu_\mathrm{N}$ (μ_N being the nuclear magneton and $\hbar$ the reduced Plank's constant) and allows a neutron to interact with unpaired electrons. Hence, magnetic structure and dynamics can be investigated.

The zero net charge implies that the neutron is not subject to the Coulomb barrier. Respectively, the scattering process can be analyzed within the Born approximation i.e. multiple scattering process can usually be ignored. This brings about very high penetration depth for most materials, which on the one hand allows for the use of complex sample environments, measurements on sealed samples (like batteries, [124]) and measurements on

large industrial samples (like a full wing of an aircraft [49]) but on the other hand implies that most neutrons interact very weakly with the majority of samples. Additionally, this implies that neutron measurements would be very non-destructive and, in case one considers typical transmission scattering experiment, non-sensitive to surface effects.

The neutron-nucleus interaction varies strongly across the periodic table and even between isotopes in a non-systematic manner. Thus, unlike in X-ray scattering, the light elements and even isotopes could be distinguished and, by varying the isotopic composition, the contrast-variation technique could be employed [43, 117].

All these render neutrons extremely attractive for investigating the structure and dynamics of matter on a wide range of length and time scales. It also makes them *irreplaceable* when bulk information needs to be obtained in a non-destructive manner. Naturally, this renders soft-matter science one of the primary interested parties in the neutron community.

Another major branch of the neutron community are the magnetism users, the reason being that magnetic neutron scattering is one of the few experimental techniques that allow to measure the magnetic microstructure in the bulk.

The average life-time of a neutron is about 900 seconds, thus there is no constraint on the measurement side, neutron can reach the sample, scatter and get to the detector. However, there is a constraint on storage – there is simply no way to "store neutrons" for a measurement. Respectively, they have to be generated continuously and this requires a large-scale facility. Furthermore, neutron sources have an inherently low (compared to X-ray) brightness.

Neutron sources

Neutrons are produced by either nuclear fission of heavy nuclei or by spallation of heavy metal targets [129]. Yet, thus produced neutrons are highly energetic and are “moderated” by a moderator like light water, heavy water or graphite to slow them down to the energy of the moderator. Then, the neutron-velocity spectrum is to a very good approximation described by a Maxwellian distribution [14].

Comparing the kinetic energy E_0 of the moderated neutrons to the thermal energy kT, research neutrons are commonly classified as hot, thermal, and cold (see Table 2.1.)

2.2 Neutron interactions

There are two types of interaction that neutrons can have with matter: either a very short-range one with a nucleus or a dipolar one with unpaired electrons (see Figure 2.1). In principle, both interactions are always going to be present and for the proper analysis of the data one would always need to consider both. Though, in non-magnetic systems, magnetic

	E_0 (meV)	T (K)	λ (Å)
Cold Neutrons	$0.1 - 10$	1-150	3-30
Thermal Neutrons	10-100	120-1200	1-3
Hot neutrons	100-500	1200-6000	0.4-1

Table 2.1 Classification of the research neutrons into cold, thermal and hot. The values indicated correspond to the spectra from the ILL. Adapted from [111, 79].

scattering is often considered to be orders of magnitude smaller than the nuclear one and hence is frequently omitted. Additionally, the dipolar nature of magnetic scattering implies that it would be highly anisotropic.

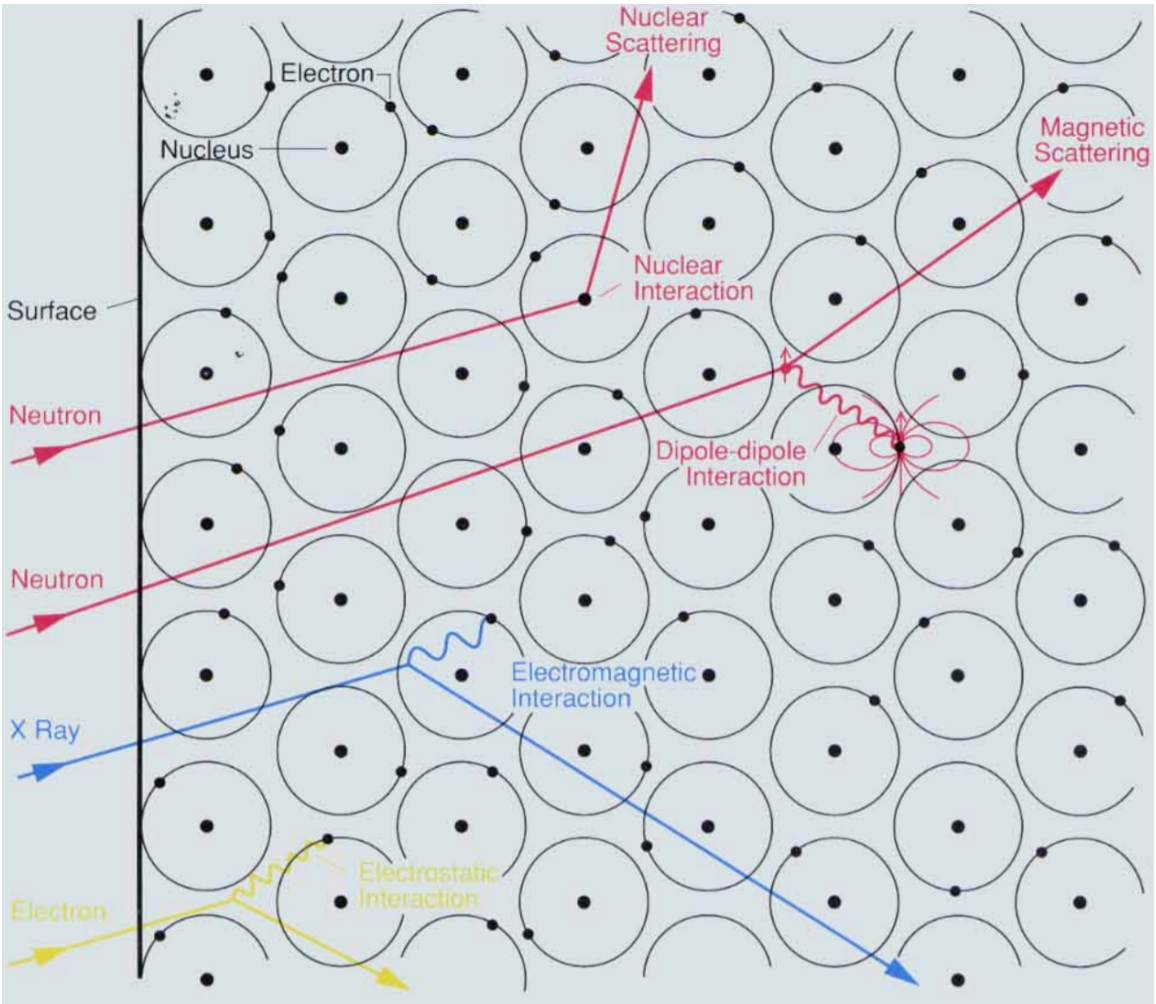

Fig. 2.1 Sketch of the penetration depth and interaction types for commonly used probes: electron, photon, and neutron. Taken from [107].

Neutron constraints

Notably, **both** interactions are quite weak, in a typical experiment in transmission geometry most ($> 90\%$) neutron simply pass through the sample. This brings in a constraint on the sample dimensions: it has to be thin enough to ensure high transmission and guarantee the the single scattering event approximation (also known as the Born approximation, see subsection 2.3.2 for more details) is valid, yet, the irradiated volume has to be as high as possible to ensure a good signal-to-noise ratio.

Thus, the weak interactions and low fluxes make neutron techniques signal-limited and they are practised only because they provide the information that is simply *unobtainable via other means* [107].

2.3 Scattering principle and quantities

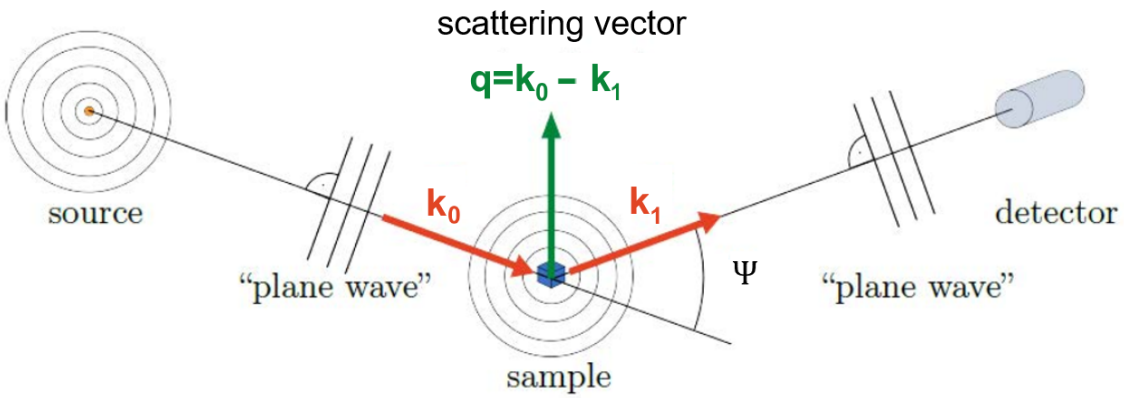

Fig. 2.2 A simplified sketch of a scattering experiment. Incident neutron is characterized by the wave vector $\mathbf{k}_0$, the scattered neutron by $\mathbf{k}_1$ and their difference is the scattering vector $\mathbf{q} = \mathbf{k}_0 - \mathbf{k}_1$. Adapted from [12].

Figure 2.2 provides a sketch for the scattering principle and allows to define the relevant quantities – scattering cross sections. The incident neutron is characterized by the wave-vector $\mathbf{k}_0$, scattering event takes place at the sample and after the scattered neutron is characterized by $\mathbf{k}_1$. The change in the wave-vector defines the momentum transfer or the scattering vector $\mathbf{q}$:

$$\mathbf{q} = \mathbf{k}_0 - \mathbf{k}_1. \tag{2.1}$$

Generally speaking, the energy of a neutron can change during the scattering event:

$$\Delta E = E_0 - E_1 = \frac{\hbar^2}{2m_n}(k_0^2 - k_1^2), \tag{2.2}$$

but this work is limited to elastic scattering only, i.e. the length of $\mathbf{k}_0$ and $\mathbf{k}_1$, respectively the neutron energies before and after the interaction with the sample are the same. Then, it is readily verified that:

$$q = |\vec{q}| = 2k_0 \sin(\psi/2) = \frac{4\pi}{\lambda}\sin(\psi/2) \cong k_0\psi \tag{2.3}$$

in the small angle approximation. Note, that in various sources different nomenclature is often employed, and the reader is directed to the nomenclature section in the beginning of this manuscript for the details on the notaion adopted here.

2.3.1 Microscopic scattering cross sections

The double differential scattering crossection is then defined as follows: the number of neutrons n' scattered per second into the solid angle $d\Omega = \sin(\psi)d\theta d\psi$ with final energy within dE' from the final neutron energy E' and normalized to the incident beam flux Φ (i.e. the number of neutrons per second per unit area perpendicular to the direction of neutron beam):

$$\frac{d^2\sigma}{d\Omega dE'} = \frac{n'}{\Phi d\Omega dE'}. \tag{2.4}$$

The energy-integrated quantity is then the differential scattering cross section:

$$\frac{d\sigma}{d\Omega} = \int_0^\infty \frac{n'}{d\Omega dE_1} dE_1 \tag{2.5}$$

and integrated over all the directions - the total scattering crossection

$$\sigma = 2\pi \int_0^\pi \frac{d\sigma}{d\Omega}\sin\psi d\psi. \tag{2.6}$$

It is worth noting, that in the domain of the small-angle scattering the detectors are usually position-sensitive (in contrast to energy-sensitive). Thus, the quantity of interest is the energy-integrated differential scattering cross section. Additionally, it is customary to display the *macroscopic* differential SANS crossection $d\Sigma/d\Omega$ per unit volume in cm^{-1} which relates to

the microscopic $d\sigma/d\Omega$ as [79]:

$$\frac{d\Sigma}{d\Omega} = \frac{N}{V}\frac{d\sigma}{d\Omega}. \tag{2.7}$$

2.3.2 Transition rate and the Born approximation

Quantum mechanically, the cross section can be computed via summing up all the scattering processes that allow transition from $\mathbf{k}_0$ to $\mathbf{k}_1$ state:

$$\frac{d\Sigma}{d\Omega} = \frac{1}{V}\frac{1}{\Phi}\frac{1}{d\Omega}\sum_{\mathbf{k}_1 \text{ in } d\Omega} W_{\mathbf{k}_0\to\mathbf{k}_1} \tag{2.8}$$

where $W_{\mathbf{k}_0\to\mathbf{k}_1}$ is the transition rate from $\mathbf{k}_0$ into $\mathbf{k}_1$ which can be evaluated using Fermi's golden rule [74, 111]:

$$\sum_{\mathbf{k}_1 \text{ in } d\Omega} W_{\mathbf{k}_0\to\mathbf{k}_1} = \frac{2\pi}{\hbar}\rho\mathbf{k}_1 |\langle \mathbf{k}_1 | V_{\text{int}} | \mathbf{k}_0 \rangle|^2 \tag{2.9}$$

where V_{int} is the interaction potential and $\rho\mathbf{k}_1$ is the density of final momentum states (in $d\Omega$).

Respectively, in an ideal world (*e.g.* the undegraduate Physics course) when the interaction potential is known, the matrix element can be evaluated and cross section computed in a straight-forward manner. In reality, however, the task is highly non-trivial, both computationally and due to the fact that the potential is *not* known. Thus, to simplify the procedure, the so-called Born approximation of both incident and scattered neutron being in a plane wave state is employed. Then, the matrix element reduces to the Fourier transform (FT further) of the interaction potential, respectively, the transition rate is proportional to the magnitude squared of the FT of the interaction potential.

Since this work mostly concerns with the magnetic neutron scattering, the magnetic interaction potential will be discussed in more detail further. Details on the nuclear interaction potential could be found elsewhere (*e.g.* [66, 116]) and are included here for completeness reasons only.

2.4 Nuclear interaction potential

The formal theory models the short-range and isotropic interaction between nucleus and neutron via Fermi's pseudopotential:

$$V_{\mathrm{nuc}}^{\mathrm{int}}(\mathbf{r}) = \frac{2\pi\hbar^2}{m_n} b\delta(\mathrm{r}), \tag{2.10}$$

where b is the atomic (nuclear) scattering length that measures both the amplitude of the scattering wave and the strength of the potential of a strongly bound nucleus at origin ($\mathbf{r} = 0$) and $\delta(\mathrm{r})$ is the Dirac's delta function. It should be noted that Equation 2.10 is *not* the actual physical interaction potential, however it is the only one that in the Born approximation yields the required isotropic scattering behavior [116, 66]. Likewise, the b is a phenomenological, experimentally measured and tabulated quantity (see [113]) rather then derived from first principles one.

In general, b is a complex quantity $b = b' - ib''$, where the real part b' can be both positive and negative and the imaginary part b'' describes the neutron capture or absorption by the given nucleus. In most elements and isotopes, the neutron capture is negligible, however there are a few exceptions (*e.g.* ^{3}He,^{10}B,^{113}Cd) which are of immense importance to neutron shielding and detectors.

It can be shown [128, 116] that by inserting the interaction potential of Equation 2.10 into Equation 2.8 and Equation 2.9 the elastic macroscopic nuclear differential scattering cross section for a collection of nuclei at positions $\mathbf{r}_k$ is:

$$\begin{aligned}\frac{d\Sigma_{\mathrm{nuc}}}{d\Omega}(\mathbf{q}) &= \frac{1}{V}\Big|\sum_{\mathrm{k=1}}^{\mathrm{N}} b_k \exp(-i\mathbf{q}\cdot\mathbf{r}_k\Big|^2 \\ &= \frac{1}{V}\sum_{\mathrm{k,l}} b_k b_l^* \exp(-i\mathbf{q}\cdot[\mathbf{r}_k - \mathbf{r}_l]),\end{aligned} \tag{2.11}$$

where V is the irradiated sample volume, b_k are the respective scattering lengths, (*) marks the complex-conjugated quantity and $i^2 = -1$. Another particularity about b is the fluctuations between different atoms of the same chemical element [111], related to the isotope variation and the nuclear spin state. Thus the summation in Equation 2.11 is performed not only over the atomic configuration, but over both the isotope distribution and the nuclear spin orientations, so that $\frac{d\Sigma_{\mathrm{nuc}}}{d\Omega}(\mathbf{q})$ is an explicitly ensemble-averaged quantity.

Obviously, there is no reasonable way to sum over all the atoms individually to account for isotope/spin variation. Thus, one assumes there is no correlation between b_k and b_l values

at any position pair and formally introduces an ensemble average [116] through:

$$\overline{b_k b_l} = \overline{b}^2 + \delta_{kl}(\overline{b^2} - \overline{b}^2), \tag{2.12}$$

where δ_{kl} is the Kronecker delta function and re-writes Equation 2.11 as:

$$\frac{d\Sigma_{\text{nuc}}}{d\Omega}(\mathbf{q}) = \frac{N}{V}(\overline{b^2} - \overline{b}^2) + \frac{1}{V}\overline{b}^2 \sum_{\text{k,l}}^{\text{N}} \exp(-i\mathbf{q}\cdot[\mathbf{r}_k - \mathbf{r}_l]). \tag{2.13}$$

The first term collects the self-scattering contributions ($k = l$) and is denoted as the nuclear *incoherent* scattering cross section, since it adds a q-independent background to the elastic SANS signal:

$$\frac{d\Sigma^{inc}_{\text{nuc}}}{d\Omega}(\mathbf{q}) = \frac{N}{V}(\overline{b^2} - \overline{b}^2) = \frac{N}{V} b^2_{inc} = \frac{N}{V}\frac{\sigma_{inc}}{4\pi}. \tag{2.14}$$

The second term in Equation 2.13 collects all the $k \neq l$ and is denoted as *coherent* scattering cross section since it contains the information about the positional correlations of the sample, *i.e.* its structure:

$$\begin{aligned}
\frac{d\Sigma^{coh}_{\text{nuc}}}{d\Omega}(\mathbf{q}) &= \frac{1}{V}\overline{b}^2 \sum_{\text{k,l}}^{\text{N}} \exp(-i\mathbf{q}\cdot[\mathbf{r}_k - \mathbf{r}_l]) \\
&= \frac{1}{V} b^2_{coh} \sum_{\text{k,l}}^{\text{N}} \exp(-i\mathbf{q}\cdot[\mathbf{r}_k - \mathbf{r}_l]) \\
&= \frac{1}{V}\frac{\sigma_{coh}}{4\pi} \sum_{\text{k,l}}^{\text{N}} \exp(-i\mathbf{q}\cdot[\mathbf{r}_k - \mathbf{r}_l]).
\end{aligned} \tag{2.15}$$

The quantities

$$\sigma_{inc} = 4\pi b^2_{inc} = 4\pi(\overline{b^2} - \overline{b}^2) \tag{2.16}$$

$$\sigma_{coh} = 4\pi b^2_{coh} = 4\pi\overline{b}^2 \tag{2.17}$$

define the (per-atom) nuclear incoherent/coherent scattering cross sections and their values are determined experimentally and tabulated. Values for most isotopes could be found in [113] or online at the NIST website [93].

In the SANS context, the discrete nature of matter becomes mostly irrelevant, since the commonly used wavelengths are generally at least twice larger than the lattice plane distance,

thus the scattering is above the Bragg cut-off. So, it is only natural to replace the sum in the Equation 2.13 by the integral and continue the discussion in terms of a coarse-grained approach where atomic scattering length b becomes scattering-length density $N(\mathbf{r})$ which is assumed to be continuous and smooth function of the position $\mathbf{r}$. Moreover, since incoherent scattering just adds a flat, q-independent background, accounting for it explicitly is omitted further.

Thus, the nuclear scattering cross section in the context of this work can be expressed as:

$$\frac{d\Sigma_{\text{nuc}}}{d\Omega} = \frac{8\pi^3}{V}|\widetilde{N}(\mathbf{q})|^2, \tag{2.18}$$

where $\widetilde{N}(\mathbf{q})$ is the FT of $N(\mathbf{r})$.

2.5 Magnetic interaction potential

Magnetic neutron scattering is rooted in the dipolar interaction of the neutron's spin (*i.e.* its magnetic moment) with the magnetic fields due to the electron spin or to electron's orbital motion. The generalized magnetic field $\mathbf{B}(\mathbf{r})$ at the position $\mathbf{r}$ due to the spin ($\mathbf{B}_{\text{S}}$) and orbital motion ($\mathbf{B}_{\text{L}}$) of the electron with the magnetic moment μ_e and linear momentum $\mathbf{p}$ is:

$$\mathbf{B}(\mathbf{r}) = \mathbf{B}_{\text{S}} + \mathbf{B}_{\text{L}} = \frac{\mu_0}{4\pi}\left(\nabla \times \frac{\mu_e \times \mathbf{r}}{r^3} - \frac{2\mu_{\text{B}}}{\hbar}\frac{\mathbf{p}\times\mathbf{r}}{r^3}\right), \tag{2.19}$$

where μ_B is the Bohr magneton and $\hbar$ is the reduced Plank's constant.

Respectively, the leading term in the magnetic interaction potential could be expressed as [116]:

$$V_{\text{mag}}^{\text{int}} = -\mu_{\mathbf{n}} \cdot \mathbf{B}(\mathbf{r}), \tag{2.20}$$

where $\mu_{\mathbf{n}} = -\gamma_n \mu_{\text{N}} \sigma_{\mathbf{P}}$ is the neutron's magnetic moment, $\gamma_n = 1.913$ is the magnetic moment of a neutron in units of nuclear magneton μ_{N} [112] and $\sigma_{\mathbf{P}}$ is the Pauli matrix describing the orientation of the neutron spin.

Higher order contributions (*e.g.* the atomic electric field) are usually neglected since they are several orders of magnitude smaller then $-\mu_{\mathbf{n}} \cdot \mathbf{B}(\mathbf{r})$ [14].

Similarly to the nuclear cross section discussion, inserting the interaction potential into the transition rate Equation 2.9 and computing the quantum mechanical cross section (Equation 2.8) one obtains the discrete elastic differential scattering cross section [116, 90,

112]:

$$\frac{d\Sigma_{mag}}{d\Omega}(\mathbf{q}) = \frac{1}{V}|\sum_{k=1}^{N} b_{m,k}\mathbf{Q}_k \exp(-i\mathbf{q}\cdot\mathbf{r}_k)|^2 \tag{2.21}$$

$$= \frac{1}{V}\sum_{\mathrm{k,l}} b_{m,k}b_{m,l}\mathbf{Q}_k\mathbf{Q}_l^* \exp(-i\mathbf{q}\cdot[\mathbf{r}_k - \mathbf{r}_l]), \tag{2.22}$$

where b_m is the atomic magnetic scattering length and $\mathbf{Q}$ is the magnetic interaction vector defined as (see below, subsection 2.5.1 for more details):

$$\mathbf{Q_k} = \hat{\mathbf{q}} \times (\hat{\mathbf{q}} \times \hat{\mathbf{m}}_\mathbf{k}) = \hat{\mathbf{q}}\,(\hat{\mathbf{q}} \cdot \hat{\mathbf{m}}_\mathbf{k}) - \hat{\mathbf{m}}_\mathbf{k}, \tag{2.23}$$

where $\hat{\mathbf{q}} = \mathbf{q}/q = \{\hat{q_x}, \hat{q_y}, \hat{q_z}\}$ is the unit scattering vector and $\hat{\mathbf{m}}_\mathbf{k} = \boldsymbol{\mu}_{a,k}/\mu_{a,k}$ is the unit vector in the direction of the atomic magnetic moment $\boldsymbol{\mu}_{a,k}$ at the position $\boldsymbol{r}_k$.

The atomic magnetic stattering length b_m is given by:

$$b_m = \frac{\gamma_n r_e}{2}\frac{\mu_a}{\mu_B} f(\mathbf{q}) \cong b_H \mu_a, \tag{2.24}$$

where $r_e = 2.818 \times 10^{15}$ m is the classical electron radius and $f(\mathbf{q})$ is the normalized atomic magnetic form factor, which, in the small-angle regime, is $f(\mathbf{q}) \cong 1$. The constant $b_H = 2.70 \times 10^{-15}\mathrm{m}\mu_B^{-1} = 2.91 \times 10^8 \mathrm{A}^{-1}\mathrm{m}^{-1}$ relates the atomic magnetic moment μ_a to the atomic magnetic scattering length $b_m \cong b_H\mu_a$ (in the small-angle approximation, μ_B being the Bohr magneton) given by [90]. Notably, b_m can be if the same order of magnitude as the nuclear scattering length and is exceptionally large for the heavy rare-earth metals (see Figure 2.3).

Exactly as in the case of nuclear analysis, the discrete picture has to be transformed into the continuum, the quantity of interest here being the magnetization vector field $\mathbf{M}(\mathbf{r})$, which, again is assumed to be a smooth and continuous function of $\mathbf{r}$. Replacing the sum by the integral over the sample volume in Equation 2.21 and the discrete terms in Equation 2.23 by the corresponding continuum expression, the unpolarized differential SANS cross section becomes:

$$\begin{aligned}\frac{d\Sigma_{mag}}{d\Omega}(\mathbf{q}) &= \frac{1}{V}b_H^2|\int_V \mathbf{Q}(\mathbf{r})\exp(-i\mathbf{q}\cdot\mathbf{r})d^3r|^2 \\ &= \frac{8\pi^3}{V}b_H^2|\widetilde{\mathbf{Q}}|^2 \\ &= \frac{8\pi^3}{V}b_H^2|\hat{\mathbf{q}} \times \left(\hat{\mathbf{q}} \times \widetilde{\mathbf{M}}\right)|^2\end{aligned} \tag{2.25}$$

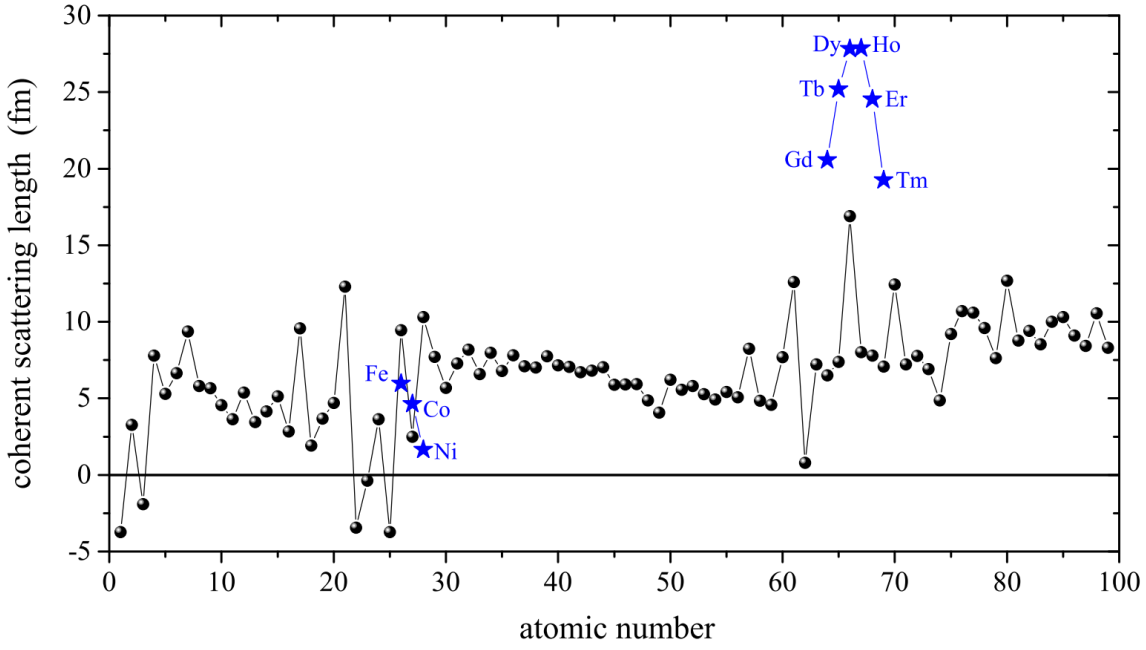

Fig. 2.3 Graphical representation of the nuclear coherent (•) and magnetic (⋆) scattering lengths versus atomic number. Taken from [79].

Thus, the magnetic scattering cross section in the context of this work can be expressed through the magnetic interaction vector $\widetilde{Q}(\mathbf{q})$ (also known as the Halpern-Johnson vector [40]) as:

$$\frac{d\Sigma_{mag}}{d\Omega} = \frac{8\pi^3}{V} b_H^2 |\widetilde{Q}(\mathbf{q})|^2. \tag{2.26}$$

2.5.1 Halpern-Johnson (magnetic interaction) vector

Halpern-Johnson vector $\widetilde{\mathbf{Q}}$ (sometimes also denoted as the magnetic interaction or magnetic scattering vector, HJ-vector further) [40] is defined as:

$$\widetilde{\mathbf{Q}} = \hat{\mathbf{q}} \times \left(\hat{\mathbf{q}} \times \widetilde{\mathbf{M}}\right) = \hat{\mathbf{q}} \left(\hat{\mathbf{q}} \cdot \widetilde{\mathbf{M}}\right) - \widetilde{\mathbf{M}}, \tag{2.27}$$

where $\hat{\mathbf{q}}$ is the unit scattering vector, and $\widetilde{\mathbf{M}}(\mathbf{q}) = \{\widetilde{M}_x(\mathbf{q}), \widetilde{M}_y(\mathbf{q}), \widetilde{M}_z(\mathbf{q})\}$ represents the Fourier transform of the magnetization vector field $\mathbf{M}(\mathbf{r}) = \{M_x(\mathbf{r}), M_y(\mathbf{r}), M_z(\mathbf{r})\}$.

Thus, essentially, the Halpern-Johnson vector captures the perpendicular component of $\widetilde{\mathbf{M}}$ with respect to the scattering vector $\mathbf{q}$ (compare Figure 2.4), emphasizing the dipolar origin of magnetic neutron scattering. Respectively, $\widetilde{\mathbf{Q}}$ is a linear vector function of the components of $\widetilde{\mathbf{M}}$.

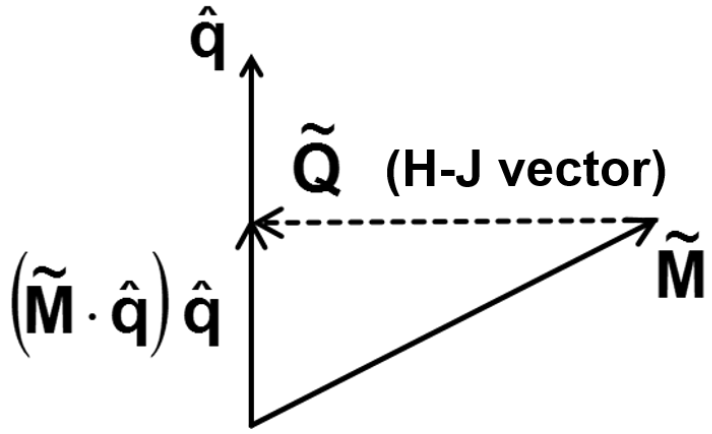

Fig. 2.4 Graphical representation of the Halpern-Johnson vector [92], emphasizing the fact that the only components of $\widetilde{\mathbf{M}}$ relevant for the magnetic neutron scattering are those *perpendicular* to $\hat{\mathbf{q}}$. Adapted from [79].

Note that different symbols for the Halpern-Johnson vector can be found in the literature. Examples include $\mathbf{M}_\perp$, $\mathbf{Q}_\perp$, $\mathbf{S}_\perp$, or $\mathbf{q}$, as in the original paper by Halpern and Johnson [40]. Additionally, in many textbooks (*e.g.* [66, 116]) $\widetilde{\mathbf{Q}}$ is defined with a minus sign and normalized by the factor $2\mu_\mathrm{B}$, which makes it dimensionless.

Finally, the essential take-away is that *only* the components of $\mathbf{M}$ which are *perpendicular* to $\mathbf{q}$ are relevant for magnetic neutron scattering.

2.6 Formal unpolarized SANS cross section

Respectively, formally the unpolarized SANS cross section could be expressed as:

$$\begin{aligned}\frac{d\Sigma_\mathrm{tot}}{d\Omega} &= \frac{d\Sigma_\mathrm{nuc}}{d\Omega}+\frac{d\Sigma_\mathrm{mag}}{d\Omega}\\ &= \frac{8\pi^3}{V}\left(|\widetilde{N}(\mathbf{q})|^2+b_H^2|\widetilde{Q}(\mathbf{q})|^2\right)\\ &= \frac{8\pi^3}{V}b_H^2\left(b_H^{-2}|\widetilde{N}(\mathbf{q})|^2+|\widetilde{Q}(\mathbf{q})|^2\right),\end{aligned} \tag{2.28}$$

where $|\widetilde{N}(\mathbf{q})|^2$ term accounts for the nuclear structure-related scattering processes and $|\widetilde{Q}(\mathbf{q})|^2$ collects all the magnetic contributions.

2.7 Description of the SANS setup

Having covered the underlying scattering principles, the particularities of the typical experimental Small Angle Neutron Scattering (SANS) setup and experimental nomenclatures need to be discussed.

2.7.1 Experimental geometries

The neutron source, the sample and the detector are a necessary minimum as per Figure 2.2, yet a real instrument will have much more in terms of guiding optics, means to discriminate neutrons on the basis of their energy (i.e. velocity) or their spin. Figure 2.5 presents a simplified sketch of a typical SANS setup: an initially polychromatic beam is monochromatized by a velocity selector, follows a shielded beam-guide up to a sample under a certain external bias. Scattered neutrons are then captured by a two-dimensional detector. Optionally, the beam is subjected to polarization manipulations before and/or after the sample. The detailed description of all the elements, albeit interesting, is beyond the scope of this thesis, for the details on implementation on different instruments the reader is referred to [48, 103, 58, 24] and references therein.

The essential moment is the bias applied to the sample - in the present work it is exclusively the applied magnetic field $\mathbf{H}_0$. Thus, a relative orientation of the $\mathbf{H_0}$ and incident neutron wave vector $\mathbf{k}_0$ needs to be discussed.

The first intuitive case is the parallel orientation: $\mathbf{H}_0 \parallel \mathbf{k}_0$ (see Figure 2.5(b)). Yet, remembering that SANS is the volume-averaged technique and that the source of the magnetic contrast is the perpendicular component of the magnetisation one would expect a largely isotropic, θ-independent magnetic scattering in this orientation (in case of an isotropic sample). Compounded with the technical difficulties of delivering a horizontal field magnet that fulfils the demands of the logistics of scattering experiments (large solid angle access, flexibility on the sample exchange) while delivering a high and uniform magnetic fields the result is that the most common design for beamline magnets is a perpendicular one [44].

The second case is the perpendicular orientation: $\mathbf{k}_0 \perp \mathbf{H}_0$ (see Figure 2.5(a)). Notably, there is no physical difference in the actual local field orientation ("top-to-bottom"/"vertical" or "left-to-right"/"horizontal"), since the Cartesian coordinate frame could be easily rotated to accommodate either case. Most commonly, such an experimental arrangement is referred to as the "perpendicular geometry", though it is not uncommon to see terms "transversal field"/"pependicular orientation" or a combination of thereof. Note, that the term "horizontal field" could refer to both $\mathbf{k}_0 \perp \mathbf{H}_0$ and $\mathbf{H}_0 \parallel \mathbf{k}_0$ and usually implies that both orientations are possible (as is the case with [44]).

Additionally, the reader should not be confused by the use of the right-handed coordinate frame in Figure 2.5(a) and left-handed coordinate frame in Figure 2.5(b), this is merely a representation convention to have the positive direction of $\mathbf{e}_z$ in the forward direction for the parallel geometry. Again, the coordinate frame could be rotated to accommodate either case without the loss of generality. Similarly, it is not uncommon to see the $\mathbf{q}$ having its origin at the origin of the coordinate frame. This potential spatial confusion is one of the reasons one the explicit orientation of the field is usually present on 2D images and, by convention, the detector images are usually oriented with positive directions to the right and to the top, regardless if they in q_z-q_y (for perpendicular) or q_x-q_y (for parallel) coordinate frame. Yet, $\mathbf{H}_0$ *always* defines the e_z direction.

For clarity, the nomenclature of Figure 2.5(a) is used further, i.e. $\theta = 0$ if $\mathbf{q} \uparrow\downarrow \mathbf{H}_0$ and the terms "parallel/perpendicular geometry" are used further in this work.

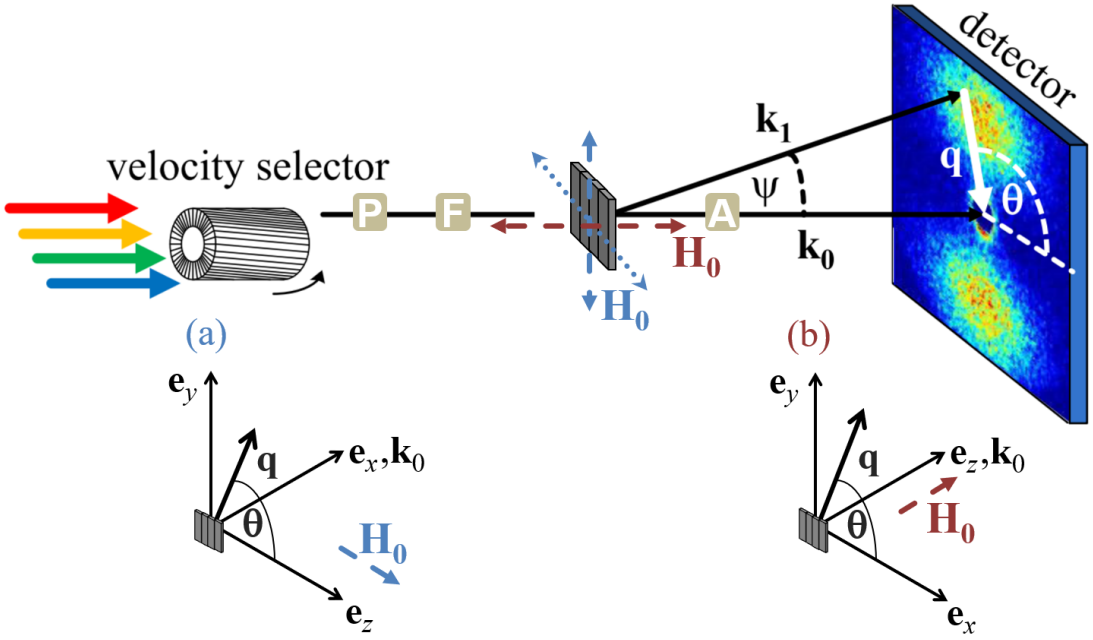

Fig. 2.5 Sketch of the neutron setup. "P", "F", "A" denote the polarizer, spin flipper and analyzer respectively. In the small-angle approximation the momentum-transfer or scattering vector $\mathbf{q} = \mathbf{k}_1 - \mathbf{k}_0$ varies in the plane perpendicular to $\mathbf{k}_0$, i.e., $\mathbf{q} \cong \{q_x, q_y, 0\} = q\{\cos\theta, \sin\theta, 0\}$. The magnitude of $\mathbf{q}$ for elastic scattering is given by $q = \frac{4\pi}{\lambda}\sin(\psi/2)$, where λ denotes the mean neutron wavelength (selected by the velocity selector) and ψ is the scattering angle. The angle θ specifies the orientation of $\mathbf{q}$ on the two-dimensional detector. (a) The external magnetic field $\mathbf{H}_0 \parallel \mathbf{e}_z$ is applied perpendicular to the wave vector $\mathbf{k}_0$ of the incident neutrons. (b) The external magnetic field $\mathbf{H}_0 \parallel \mathbf{e}_z$ is applied parallel to the wave vector $\mathbf{k}_0$ of the incident neutrons. Adapted from [79].

In the perpendicular case ($\mathbf{k}_0 \perp \mathbf{H}_0$; $\mathbf{k}_0 \parallel \mathbf{e}_x$ (compare Figure 2.5(a)), the scattering vector $\mathbf{q}$ has the norm of $|\mathbf{q}| = q$ and, since we are dealing with elastic scattering ($|\mathbf{k}_0| = |\mathbf{k}_1|$) throughout this thesis, $q = 2|\mathbf{k}_0|\sin(\psi/2) = \frac{4\pi}{\lambda}\sin(\psi/2)$.

Thus, bearing in mind that the angle θ specifies the orientation of $\mathbf{q}$ on the detector, $\mathbf{q}$ becomes (in Cartesian components):

$$\mathbf{q}_\perp = \left\{ \begin{array}{c} q_x \\ q_y \\ q_z \end{array} \right\} = q \left\{ \begin{array}{c} -\sin(\psi/2) \\ \cos(\psi/2)\sin(\theta) \\ \cos(\psi/2)\cos(\theta) \end{array} \right\} = \mathrm{k}_0 \left\{ \begin{array}{c} \cos(\psi)-1 \\ \sin(\psi)\sin(\theta) \\ \sin(\psi)\cos(\theta) \end{array} \right\}, \tag{2.29}$$

and, respectively, for the parallel case ($\mathbf{k}_0 \parallel \mathbf{H}_0$; $\mathbf{k}_0 \parallel \mathbf{e}_z$ (compare Figure 2.5(b)),

$$\mathbf{q}_\parallel = \left\{ \begin{array}{c} q_x \\ q_y \\ q_z \end{array} \right\} = q \left\{ \begin{array}{c} \cos(\psi/2)\cos(\theta) \\ \cos(\psi/2)\sin(\theta) \\ -\sin(\psi/2) \end{array} \right\} = \mathrm{k}_0 \left\{ \begin{array}{c} \sin(\psi)\cos(\theta) \\ \sin(\psi)\sin(\theta) \\ \cos(\psi)-1 \end{array} \right\}. \tag{2.30}$$

2.7.2 Small angle approximation

For small angles - *i.e.* $\psi << 1$ or, rather, $\psi \leq 5-10^\circ$ the component of $\mathbf{q}$ along the incident beam direction is much smaller than the other two. Thus, q is approximated by a two-dimensional vector in the plane perpendicular to the incident beam direction. Respectively, for $\mathbf{k}_0 \perp \mathbf{H}_0$ and $\mathbf{k}_0 \parallel \mathbf{H}_0$ one finds (subscripts $\perp$ and $\parallel$ refer to the respective scattering geometry, compare Figure 2.5):

$$\hat{\mathbf{q}}_\perp = \{0, \sin\theta, \cos\theta\}, \tag{2.31}$$

$$\hat{\mathbf{q}}_\parallel = \{\cos\theta, \sin\theta, 0\}. \tag{2.32}$$

Inserting these expressions into the Equation 2.27 yields:

$$\widetilde{\mathbf{Q}}_\perp = \left\{ \begin{array}{c} -\widetilde{M}_x \\ -\widetilde{M}_y\cos^2\theta + \widetilde{M}_z\sin\theta\cos\theta \\ \widetilde{M}_y\sin\theta\cos\theta - \widetilde{M}_z\sin^2\theta \end{array} \right\}, \tag{2.33}$$

$$\widetilde{\mathbf{Q}}_\parallel = \left\{ \begin{array}{c} -\widetilde{M}_x\sin^2\theta + \widetilde{M}_y\sin\theta\cos\theta \\ \widetilde{M}_x\sin\theta\cos\theta - \widetilde{M}_y\cos^2\theta \\ -\widetilde{M}_z \end{array} \right\}. \tag{2.34}$$

In general, $\widetilde{\mathbf{M}}(\mathbf{q})$ and likewise $\widetilde{\mathbf{Q}}(\mathbf{q})$ are complex vectors.

2.8 Micromagnetic theory

The further analysis of the magnetic SANS cross section (Equation 2.26) relies on the simplified expressions of the HJ-vector for a given geometry (Equation 2.33/Equation 2.34), which, in turn, require expressions for the magnetization Fourier amplitudes $\widetilde{M}_{x,y,z}$.

In Refs. [80, 84] a general theory of magnetic SANS based on the continuum theory of micromagnetics has been developed. The representation here is included for completeness sake only and aims at sketching the path rather then guiding the reader through all the steps. It does, however, aim to be complete in all the necessary logical steps.

2.8.1 Fields and the balance of torques

The micromagnetic theory takes into account the isotropic and symmetric exchange interaction, magnetic anisotropy, as well as the Zeeman and the magnetodipolar interaction energies. As detailed in the pertinent textbooks [11, 2, 62, 33], variational calculus leads to a set of nonlinear partial differential equations for the equilibrium magnetization configuration $\mathbf{M}(\mathbf{r})$. For the static case, the equations of micromagnetics (so-called Brown's equations) can be expressed as a balance-of-torques equation:

$$\mathbf{M}(\mathbf{r}) \times \mathbf{H}_{\text{eff}}(\mathbf{r}) = 0. \tag{2.35}$$

Equation 2.35 expresses the fact that at static equilibrium the torque on the magnetization $\mathbf{M}(\mathbf{r})$ due to an effective magnetic field $\mathbf{H}_{\text{eff}}(\mathbf{r})$ vanishes at each point $\mathbf{r}$ inside the material. The effective field is obtained as:

$$\mathbf{H}_{\text{eff}}(\mathbf{r}) = \mathbf{H}_0 + \mathbf{H}_{\text{d}}(\mathbf{r}) + \mathbf{H}_{\text{p}}(\mathbf{r}) + \mathbf{H}_{\text{ex}}(\mathbf{r}) + \mathbf{H}_{\text{DMI}}(\mathbf{r}), \tag{2.36}$$

where $\mathbf{H}_0$ is a uniform applied magnetic field, $\mathbf{H}_{\text{d}}(\mathbf{r})$ denotes the magnetostatic field, $\mathbf{H}_{\text{p}}(\mathbf{r})$ is the magnetic anisotropy field, $\mathbf{H}_{\text{ex}}(\mathbf{r}) = l_{\text{M}}^2 \Delta \mathbf{M}(\mathbf{r})$ represents the exchange field (with Δ the Laplace operator), and $\mathbf{H}_{\text{DMI}}(\mathbf{r})$ is the asymmetric field due to the Dzyaloshinskii–Moriya Interaction (DMI further).

2.8.2 Characteristic length scales

Each of the fields mentioned above could be characterized by a certain length scale which measures the spacial extent of correlataions due to the given field. The applied field being homogeneous around the sample, its correlation length is, effectively infinite.

In the context of micromagnetics, the characteristic length scales are:

- l_{M}, the magnetostatic exchange length, characterizes the competition between the exchange and magnetostatic interactions, defined as:

$$l_{\mathrm{M}} = \sqrt{\frac{2A}{\mu_0 M_s^2}} \tag{2.37}$$

  l_{M} is of the order of a few nanometers for many magnetic materials ($l_M \sim 3 - 10\,\mathrm{nm}$ [62]).

- l_{H}, the micromagnetic exchange length of the field, characterizes field-dependent size of perturbed (inhomogeneously magnetized) regions around microstructural defects [77] and is defined as:

$$l_{\mathrm{H}}(\mathrm{H}_i) = \sqrt{\frac{2A}{\mu_0 M_s H_i}} \tag{2.38}$$

  $l_{\mathrm{H}}(\mathrm{H}_i)$ varies between few and few hundred nanometers [79]. For typical values for the material parameters of *e.g.* Co ($A = 2.8 \times 10^{-11}\,\mathrm{J/m}$ and $\mu_0 M_s = 1.80\,\mathrm{T}$ [87]), the l_H varies between about $200 - 2\,\mathrm{nm}$ when the internal field is changed between $0.001 - 10\,\mathrm{T}$. This length scale falls well into the resolution regime of the SANS technique.

- l_{D}, the exchange length of the DMI, characterizes the DMI field $\mathbf{H}_{\mathrm{DMI}}(\mathbf{r})$ and defined as:

$$l_{\mathrm{D}} = \frac{2D}{\mu_0 M_s^2} \tag{2.39}$$

  typically, $l_{\mathrm{D}} \cong 1 - 2\,\mathrm{nm}$, however, due to the lack of an established database for D-values, this estimate should be considered with some care [79].

In all of the above, A is the exchange-stiffness constant, D is the DMI constant, M_s is the saturation magnetization, $H_{\mathrm{i}} = H_0 - NM_s$ is the internal magnetic field (N: demagnetizing factor) and μ_0 is the permeability of free space.

The values for the DMI constant D and for the exchange-stiffness constant A are assumed to be uniform throughout the material, in contrast to the local saturation magnetization $M_{\mathrm{s}}(\mathbf{r})$, which is assumed to depend explicitly on the position $\mathbf{r}$ (see also [75]). Since the Fourier coefficient of the longitudinal magnetization $\widetilde{M}_z(\mathbf{q})$, is proportional to the abrupt change in the magnitude of the magnetization at internal particle-matrix interfaces ΔM (for further details see [47]), it is strongly coupled to $M_{\mathrm{s}}(\mathbf{r})$.

The Figure 2.6 graphically represents typical values for the micromagnetic lengths at a typical range of fields. Clearly, all these fall perfectly into the SANS regime of several to several hundred nanometres, thus it often becomes the technique of choice.

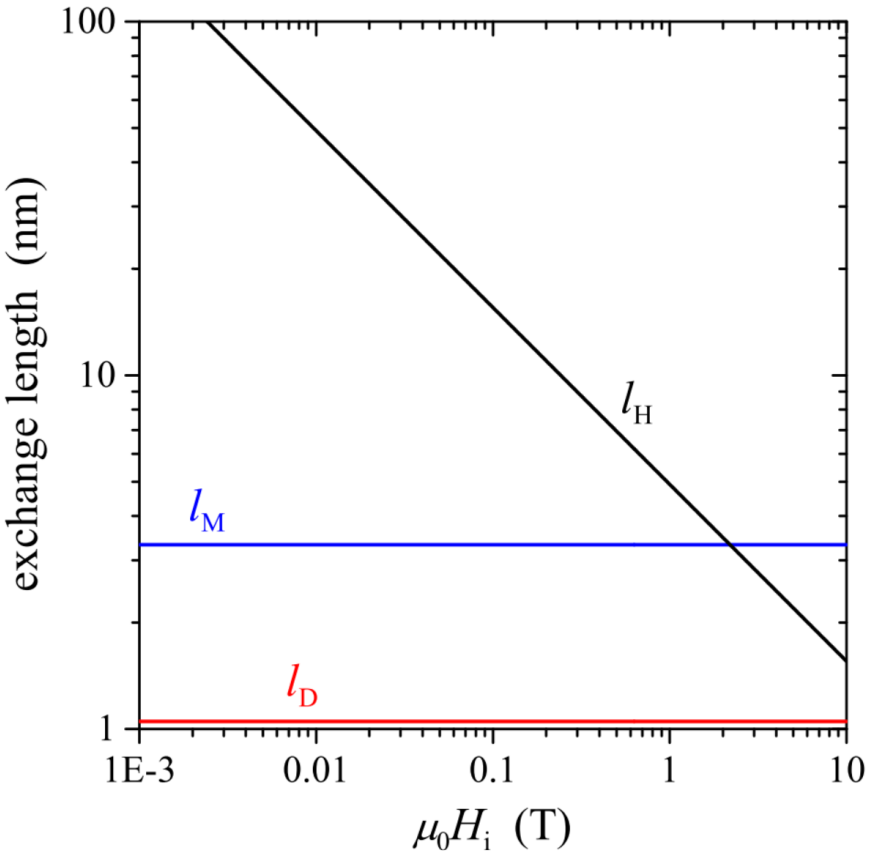

Fig. 2.6 Micromagnetic length scales l_M, l_H and l_D as a function of the internal magnetic field $\mu_0 H_i$ (log-log scale). Material parameters for iron at 300K were used [62]. Adapted from [79].

Note, that occasionally one encounters the notation with M_0 in stead of M_s quoted here. The former is defined as $M_0 = V^{-1} \int_V M_s(\mathbf{r}) dV$ and denotes the macroscopic saturation magnetization of the sample, which can be measured with a magnetometer.

In the approach-to-saturation regime, the micromagnetic equations can be linearised and closed-form expressions for the magnetization Fourier components $\widetilde{M}_x(\mathbf{q})$ and $\widetilde{M}_y(\mathbf{q})$ can be obtained (see [80, 84] for details).

2.8.3 Closed-form solutions in the approach to saturation

In the approach-to-saturation regime the $M_z \cong M_s$ is assumed, M_z being the the longitudinal magnetization in the direction of the applied field $\mathbf{H}_0$.

The solution of the linearised version of the Equation 2.35 (see [84, 79] for details) provides closed-form expressions for the transversal Fourier components $\widetilde{M}_x(\mathbf{q})$ and $\widetilde{M}_y(\mathbf{q})$:

$$\widetilde{M}_x = \frac{p\left(\widetilde{H}_{\mathrm{p}x}\left[1+p\frac{q_y^2}{q^2}\right]-\widetilde{M}_z\frac{q_x q_z}{q^2}\left[1+pl_{\mathrm{D}}^2q^2\right]-\widetilde{H}_{\mathrm{p}y}p\frac{q_x q_y}{q^2}\right)}{\left(1+p\frac{q_{\mathrm{x}}^2+q_{\mathrm{y}}^2}{q^2}-p^2l_{\mathrm{D}}^2q_{\mathrm{z}}^2\right)} - i\frac{p\left(\widetilde{M}_{\mathrm{z}}\left[1+p\right]l_{\mathrm{D}}q_y-\widetilde{H}_{\mathrm{p}y}pl_{\mathrm{D}}q_z\right)}{\left(1+p\frac{q_{\mathrm{x}}^2+q_{\mathrm{y}}^2}{q^2}-p^2l_{\mathrm{D}}^2q_{\mathrm{z}}^2\right)}, \tag{2.40}$$

$$\widetilde{M}_y = \frac{p\left(\widetilde{H}_{\mathrm{p}y}\left[1+p\frac{q_{\mathrm{x}}^2}{q^2}\right]-\widetilde{M}_z\frac{q_y q_z}{q^2}\left[1+pl_{\mathrm{D}}^2q^2\right]-\widetilde{H}_{\mathrm{p}x}p\frac{q_{\mathrm{x}}q_{\mathrm{y}}}{q^2}\right)}{\left(1+p\frac{q_{\mathrm{x}}^2+q_{\mathrm{y}}^2}{q^2}-p^2l_{\mathrm{D}}^2q_{\mathrm{z}}^2\right)} - i\frac{p\left(\widetilde{M}_z\left[1+p\right]l_{\mathrm{D}}q_x-\widetilde{H}_{\mathrm{p}x}pl_{\mathrm{D}}q_z\right)}{\left(1+p\frac{q_{\mathrm{x}}^2+q_{\mathrm{y}}^2}{q^2}-p^2l_{\mathrm{D}}^2q_{\mathrm{z}}^2\right)}. \tag{2.41}$$

The dimensionless function $p(q,H_{\mathrm{i}})$ is defined as

$$p(q,H_{\mathrm{i}}) = \frac{M_0}{H_{\mathrm{eff}}(q,H_{\mathrm{i}})} = \frac{M_0}{H_{\mathrm{i}}\left(1+l_{\mathrm{H}}^2q^2\right)}, \tag{2.42}$$

where $H_{\mathrm{eff}}(q,H_i)$ is the the effective magnetic field defined as $H_{\mathrm{eff}}(q,H_{\mathrm{i}}) = H_{\mathrm{i}}\left(1+l_{\mathrm{H}}^2q^2\right)$. p depends on the internal magnetic field H_{i}, on q, and on the exchange length of the field l_{H}.

Averaging over the directions of the magnetic anisotropy field in the plane perpendicular to the applied field, the magnetic terms are:

For the transversal magnetic field geometry ($\mathbf{k}_0 \perp \mathbf{H}_0$):

$$|\widetilde{M}_x|^2 = \frac{p^2}{2}\frac{\widetilde{H}_{\mathrm{p}}^2\left(\left[1+p\sin^2\theta\right]^2+p^2l_{\mathrm{D}}^2q^2\cos^2\theta\right)+2\widetilde{M}_z^2(1+p)^2l_{\mathrm{D}}^2q^2\sin^2\theta}{\left(1+p\sin^2\theta-p^2l_{\mathrm{D}}^2q^2\cos^2\theta\right)^2}, \tag{2.43}$$

$$|\widetilde{M}_y|^2 = \frac{p^2}{2}\frac{\widetilde{H}_{\mathrm{p}}^2\left(1+p^2l_{\mathrm{D}}^2q^2\cos^2\theta\right)+2\widetilde{M}_z^2\left(1+pl_{\mathrm{D}}^2q^2\right)^2\sin^2\theta\cos^2\theta}{\left(1+p\sin^2\theta-p^2l_{\mathrm{D}}^2q^2\cos^2\theta\right)^2}, \tag{2.44}$$

For the parallel field geometry ($\mathbf{k}_0 \parallel \mathbf{H}_0$):

$$|\widetilde{M}_x|^2 = \frac{p^2}{2}\frac{\widetilde{H}_\mathrm{p}^2\left(1+p(2+p)\sin^2\theta\right)+2\widetilde{M}_z^2(1+p)^2 l_\mathrm{D}^2 q^2\sin^2\theta}{(1+p)^2}, \tag{2.45}$$

$$|\widetilde{M}_y|^2 = \frac{p^2}{2}\frac{\widetilde{H}_\mathrm{p}^2\left(1+p(2+p)\cos^2\theta\right)+2\widetilde{M}_z^2(1+p)^2 l_\mathrm{D}^2 q^2\cos^2\theta}{(1+p)^2}. \tag{2.46}$$

In the Equation 2.43 and Equation 2.46, $\widetilde{H}_\mathrm{p}^2$ denotes the magnitude-square of the Fourier transform of the magnetic anisotropy field. Respectively, it characterizes the strength and spatial structure of the magnetic anisotropy field $\mathbf{H}_\mathrm{p}(\mathbf{r})$.

By inserting Equation 2.43 and Equation 2.46 into the magnetic SANS cross section (Equation 2.26) and summing magnetic and nuclear (Equation 2.18) cross sections the total SANS cross section could be obtained.

2.8.4 Origin of the magnetic scattering contrast

As mentioned above, in the context of the micromagnetic theory the sample is always in the approach to saturation regime. There is no formal, quantitative definition of the lower limit of the "approach to saturation", yet commonly a value of net magnetization of 80-95% of the saturation magnetisation value is used. Thus, there is always a sufficiently high external magnetic field H_0 applied which defines the quantization axis and most atomic spins are aligned in the direction of H_0. Since all the physical information about the magnetic sample properties extracted in a scattering experiment is contained in the Halpern-Johnson vector $\widetilde{\mathbf{Q}}(\mathbf{q})$ through the magnetization vector field $\mathbf{M}(\mathbf{r})$, the origins of the magnetic contrast should be discussed.

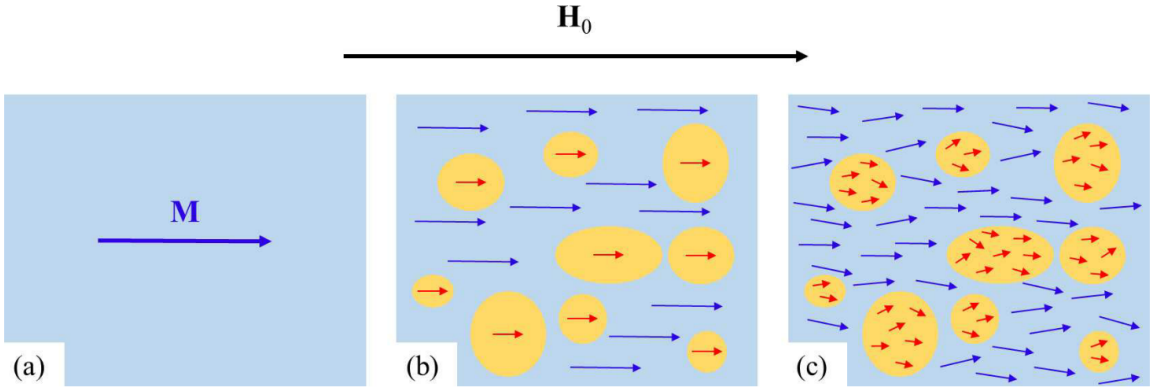

Fig. 2.7 Simplified magnetization distribution scetches. (a) Homogeneous and uniformely magnetized (saturated) ferromagnet; (b) inhomogeneous and uniformly magnetized magnet; (c) an inhomogeneous and non-uniformly magnetized magnet. Taken from [79].

Figure 2.7 schematically represents simple magnetization distribution cases. (a) is a completely homogeneous saturated case, *i.e.* $\mathbf{M}(\mathbf{r}) = \mathbf{const} = \{0,0,M_s\}$ is a constant vector aligned with the applied field $\mathbf{H_0}$. A prototypical example of such a system would be a saturated ferromagnet or a single-domain nanoparticle. Respectively, the FT of the $\mathbf{M}(\mathbf{r})$ is a delta function at the origin of the reciprocal space and, essentially, there is no magnetic SANS contrast.

(b) is a completely saturated (uniformly magnetized) multiphase case, where the direction is constant throughout, but the magnitude depends on the position, *i.e.* $\mathbf{M}(\mathbf{r}) = \{0,0,M_s(\mathbf{r})\}$. A prototypical example of such a system would be a saturated ferromagnet with pores or a distribution of single-domain nanoparticles in a non-magnetic or saturated matrix. Respectively, the FT of the $\mathbf{M}(\mathbf{r})$ is a q-dependent scalar function and the magnetic SANS signal could be expressed as:

$$\frac{d\Sigma_{mag}}{d\Omega} = \frac{8\pi^3}{V} b_H^2 |\widetilde{Q}(\mathbf{q})|^2 \propto |\widetilde{M_s}(\mathbf{q})|^2. \tag{2.47}$$

Finally, (c) is the most general case of an inhomogenious non-uniformly magnetized specimen, where both the magnitude and direction of $\mathbf{M}$ depend on $\mathbf{r}$, *i.e.* $\mathbf{M}(\mathbf{r}) = \{M_x(\mathbf{r}, M_y(\mathbf{r}, M_z(\mathbf{r})\}$. A prototypical example of such a system would be a polycrystalline elemental magnet (with crystallites in the nanometer size) or a multi-phase magnetic nanocomposite which includes most engineering materials like magnetic steels, shape-memory alloys and permanent magnets. Respectively, the FT of the $\mathbf{M}(\mathbf{r})$ is a q-dependent vector function with the constraint of the constant magnitude $|\mathbf{M}(\mathbf{r})| = M_s$.

Note, that at a complete saturation the case (c) reduces to (b).

Thus, in the following two origins of magnetic scattering/spin misalignment are considered:

- (i) Spatial variations of the saturation magnetization $M_s(\mathbf{r})$
- (ii) Spatial nanometer-scale variations in the local magnetization profile.

Whereas (i) is intuitively understood via multiphase material or pores, (ii) deserves a closer look.

A large number of magnetic materials studied using SANS are polycrystalline in nature, *i.e.* their macroscopic properties (and the magnetic SANS signal) are largely determined by the lattice defects, pores and grain/phase boundaries. The local magnetization is coupled to the disturbance via magnetoelastic coupling energy, *i.e.* the stress field related to the inhomogeneity couples to the $\mathbf{M}(\mathbf{r})$, resulting in a (small) local deviation from the mean magnetization. The ferromagnetic exchange interaction with its energy contribution aiming to

avoid gradients in $\mathbf{M}(\mathbf{r})$, extends the stress field further into the material, creating a perturbed region over many lattice sites around the defect. The extent of this region is quantified via the (micro)magnetic exchange length l_{H}. Naturally, higher external field H_0 reduces the extent of the perturbed region thus suppressing the fluctuations.

Thus, the orientation and/or magnitude of the magnetic anisotropy field $\mathbf{H}_p(\mathbf{r})$ (*e.g.*, at a grain boundary in a single-phase nanocrystalline ferromagnet) is largely (but not solely) responsible for the (ii), since anisotropy field fluctuations give rise to torques on the $\mathbf{M}(\mathbf{r})$ and result in a deviation from the mean magnetization direction given by a large H_0.

Essentially, the source of the magnetic scattering contrast is either due to variations in the magnitude of the saturation magnetization or the lack of alignment of the local magnetization profile to the external field. Thus, it is not uncommon to see the magnetic scattering to be referred to as the "spin-missalignment" scattering, while the saturated state (Figure 2.7(b)) is commonly used as a reference.

2.9 SANS cross section at complete saturation

As mentioned above, the total cross section consists of nuclear and magnetic part. Compactly, it could be written as

$$\begin{aligned}\frac{d\Sigma_{\mathrm{tot}}}{d\Omega} &= \frac{d\Sigma_{\mathrm{nuc}}}{d\Omega}+\frac{d\Sigma_{\mathrm{mag}}}{d\Omega}\\ &= \frac{8\pi^3}{V}\left(|\widetilde{N}(\mathbf{q})|^2+b_H^2|\widetilde{Q}(\mathbf{q})|^2\right)\\ &= \frac{8\pi^3}{V}b_H^2\left(b_H^{-2}|\widetilde{N}(\mathbf{q})|^2+|\widetilde{Q}(\mathbf{q})|^2\right).\end{aligned} \tag{2.48}$$

In the case of complete saturation, the magnetization vector field is $\mathbf{M}(\mathbf{r})=\{0,0,M_s\}$, *i.e.* all the moments are aligned in the direction of the applied magnetic field H_0. This state is commonly used as a reference for the analysis of the measurements at lower applied fields [79], since in this case the problem is reduced to finding the scalar function M(r) which is determined by the microstructure. This is fully analogous to the problem encountered in nuclear SANS and SAXS thus the well-known procedures can be applied.

Respectively, conceptually, the magnetization profile at lower fields can be expressed as the saturated case with an added disturbance. It is worth noting, that given the isotropic material(*i.e.* a non-textured material), the nuclear contribution is usually isotropic (*i.e.* $\theta-$independent). Similarly, the component of Mz parallel to the applied field would be isotropic as well given the approach-to-saturation regime. Thus, it is not uncommon to unite both nuclear scattering term and Mz term into the so-called residual scattering $\frac{d\Sigma_{\mathrm{res}}}{d\Omega}$.

The remaining terms are then united under the term "spin-missalignement scattering" $\frac{d\Sigma_{\mathrm{SM}}}{d\Omega}$. Note, that there is no single standard, and one might encounter the subdivision into nuclear and magnetic scattering rather then residual and spin-missalignment scattering. Thus, alternatively the cross section is expressed as:

$$\frac{d\Sigma_{\mathrm{tot}}}{d\Omega} = \frac{d\Sigma_{\mathrm{res}}}{d\Omega} + \frac{d\Sigma_{\mathrm{SM}}}{d\Omega}.$$

For the sake of clarity, since arbitrarily high saturated fields often can not be achieved, the term "magnetic SANS crossection" denoted as $\frac{d\Sigma_{\mathrm{M}}}{d\Omega}$ can also be encountered in the literature. Practically, it is still the same difference, but the "completely saturated state" is, explicitly, the state at the highest available field. Respectively, sometimes the terms $\frac{d\Sigma_{\mathrm{SM}}}{d\Omega}$ (which denotes the difference between a completely saturated state SANS and the signal at a lower field) and $\frac{d\Sigma_{\mathrm{M}}}{d\Omega}$ (which denotes the difference between the state at the highest available field and the signal at a lower field) are used interchangeably.

2.10 SANS cross section in the approach to saturation

Thus, it is a common practice [78, 92, 79] to separate magnetic contribution by subtracting the scattering data at the highest available (or saturation) field from the scattering data at the lower field.

To be more precise, the subtraction procedure results in a magnetic SANS cross section which depends on the *differences* of the magnetization Fourier components at the two fields considered, e.g., $\Delta|\widetilde{M}_x|^2 = |\widetilde{M}_x|^2(H_0) - |\widetilde{M}_x|^2(H_{\max})$ (and similarly for the other Fourier components). The field dependence of the transversal magnetization Fourier components $\widetilde{M}_x$ and $\widetilde{M}_y$ is different from, and usually much larger than, the longitudinal component $\widetilde{M}_z$ (see Fig. 8 in [81]); more specifically, $\widetilde{M}_{x,y}$ are usually larger at lower field than at higher field, whereas $\widetilde{M}_z$ may weakly increase with increasing field. Effectively, this entails that for many materials (and for all materials appearing later in this work) the difference SANS cross section is non-negative at all $\mathbf{q}$ and H_0 investigated.

Additionally, the magnetization of a bulk ferromagnet is a function of the position $\mathbf{r} = \{x, y, z\}$ inside the material, i.e., $\mathbf{M} = \mathbf{M}(x, y, z)$, and that, consequently, $\widetilde{\mathbf{M}} = \widetilde{\mathbf{M}}(q_x, q_y, q_z)$. However, the Fourier components in subsection 2.8.3 represent projections into the plane of the two-dimensional detector, i.e., the q_y-q_z-plane for $\mathbf{H}_0 \perp \mathbf{k}_0$ ($q_x \cong 0$) (compare Figure 2.5(a)) and the q_y-q_x-plane for $\mathbf{H}_0 \parallel \mathbf{k}_0$ ($q_z \cong 0$) (compare Figure 2.5(b)) since in the small-angle approximation the component of $\mathbf{q}$ along the incident beam ($\mathbf{k}_0 \parallel \mathbf{e}_z$ in the parallel geometry and $\mathbf{k}_0 \parallel \mathbf{e}_x$ in the perpendicular geometry) is negligible as compared to

the other two components. This explicitly demonstrates that SANS predominantly measures correlations in the plane *perpendicular* to the incident neutron beam.

2.11 Unpolarized cross sections

In the following, V is the scattering volume, $b_{\mathrm{H}} = 2.70 \times 10^{-15}\,\mathrm{m}\,\mu_{\mathrm{B}}^{-1} = 2.91 \times 10^{8}\,\mathrm{A^{-1}m^{-1}}$ relates the atomic magnetic moment μ_a to the atomic magnetic scattering length $b_m \cong b_H \mu_a$ (in small-angle approximation, μ_{B} being the Bohr magneton) given by [90]:

$$b_{\mathrm{m}} = \frac{\gamma_{\mathrm{n}} r_0}{2} \frac{\mu_{\mathrm{a}}}{\mu_{\mathrm{B}}} f(\mathbf{q}) \cong 2.70 \times 10^{-15}\,\mathrm{m} \frac{\mu_{\mathrm{a}}}{\mu_{\mathrm{B}}} f(\mathbf{q}) \cong b_{\mathrm{H}} \mu_{\mathrm{a}},$$

where $\gamma_{\mathrm{n}} = 1.913$ denotes the neutron magnetic moment expressed in units of the nuclear magneton, $r_0 = 2.818 \times 10^{-15}\,\mathrm{m}$ is the classical radius of the electron, and $f(\mathbf{q})$ is the normalized atomic magnetic form factor, which we set to unity, $f \cong 1$, along the forward direction.

$\widetilde{N}(\mathbf{q})$ and $\widetilde{\mathbf{M}}(\mathbf{q})$ denote, respectively, the Fourier transforms of the nuclear scattering length density $N(\mathbf{r})$ and of the magnetization vector field $\mathbf{M}(\mathbf{r})$, the angle θ is measured between $\mathbf{q}$ and $\mathbf{e}_z \parallel \mathbf{H}_0$ in the perpendicular and between $\mathbf{q}$ and $\mathbf{e}_x$ in the parallel geometry and the asterisk (*) marks the complex-conjugated quantity.

2.11.1 $\mathbf{k}_0 \perp \mathbf{H}_0$

For the perpendicular scattering geometry ($\mathbf{H}_0 \perp \mathbf{k}_0$) the unpolarized elastic differential SANS cross section $d\Sigma/d\Omega$ at momentum-transfer vector $\mathbf{q}$ can be written as [78, 92]:

$$\frac{d\Sigma}{d\Omega}^{\perp}_{\mathbf{H}_0}(\mathbf{q}) = \frac{8\pi^3}{V} b_H^2 \Big(b_H^{-2} |\widetilde{N}|^2 + |\widetilde{M}_x|^2 + |\widetilde{M}_y|^2 \cos^2\theta + |\widetilde{M}_z|^2 \sin^2\theta - (\widetilde{M}_y \widetilde{M}_z^* + \widetilde{M}_y^* \widetilde{M}_z) \sin\theta\cos\theta \Big). \tag{2.49}$$

As noted in section 2.9, in a typical magnetic SANS data analysis routine the total nuclear and magnetic SANS cross section at the highest available field is subtracted from the data at lower fields. So, assuming the applied field $\mathbf{H}_{\mathrm{sat}}$ saturates the sample and $\widetilde{M}_z \cong \widetilde{M}_{\mathrm{s}}$, the saturated cross section in the perpendicular geometry is:

$$\frac{d\Sigma}{d\Omega}^{\perp}_{\mathbf{H}_{\mathrm{sat}}}(\mathbf{q}) = \frac{d\Sigma}{d\Omega}^{\perp}_{\mathrm{res}}(\mathbf{q}) = \frac{8\pi^3}{V} b_H^2 \Big(b_H^{-2} |\widetilde{N}|^2 + |\widetilde{M}_z|^2 \sin^2\theta \Big). \tag{2.50}$$

Respectively, at a finite non-saturating field $\mathbf{H}_0$ subtracting Equation 2.50 from Equation 2.49 eliminates the nuclear SANS contribution and longitudinal magnetic SANS contribution in Equation 2.49 and yields the purely magnetic (or spin-misalignment) SANS cross section $\frac{d\Sigma_{\mathrm{SM}}}{d\Omega}$:

$$\begin{aligned}\frac{d\Sigma}{d\Omega}^{\perp}_{\mathrm{SM}}(\mathbf{q},\mathbf{H}_0) &= \frac{d\Sigma}{d\Omega}^{\perp}_{\mathbf{H}_0}(\mathbf{q}) - \frac{d\Sigma}{d\Omega}^{\perp}_{\mathrm{res}}(\mathbf{q}) \\ &= \frac{8\pi^3}{V} b_H^2 \Big(|\widetilde{M}_x|^2 + |\widetilde{M}_y|^2 \cos^2\theta - (\widetilde{M}_y \widetilde{M}_z^* + \widetilde{M}_y^* \widetilde{M}_z) \sin\theta \cos\theta \Big) \end{aligned} \tag{2.51}$$

Micromagnetic representation

Alternatively, decomposing the spin-misalignment cross section into contributions due to:

- perturbing magnetic anisotropy fields by accounting for the local variations in easy-axis orientation through the anisotropy-field scattering function S_{H},
- magnetostatic fields by accounting for the spatial variations in the saturation magnetization through the longitudinal magnetization scattering function S_{M},

Equation 2.51 can be expressed in terms of the micromagnetic functions [47, 125]:

$$\frac{d\Sigma}{d\Omega}^{\perp}_{\mathrm{SM}}(\mathbf{q},\mathbf{H}_0) = S_{\mathrm{H}}(\mathbf{q}) R_{\mathrm{H}}(q,\theta,H_i) + S_{\mathrm{M}}(\mathbf{q}) R_{\mathrm{M}}(q,\theta,H_i), \tag{2.52}$$

where $R_{\mathrm{H/M}}$ are the dimensionless response functions defined as:

$$R_{\mathrm{H}}(q,\theta,H_i) = \frac{p^2}{2}\left(1 + \frac{\cos^2\theta}{(1+p\sin^2\theta)^2}\right), \tag{2.53}$$

$$R_{\mathrm{M}}(q,\theta,H_i) = \frac{p^2 \sin^2\theta \cos^4\theta}{(1+p\sin^2\theta)^2} + \frac{2p\sin^2\theta\cos^2\theta}{1+p\sin^2\theta}, \tag{2.54}$$

with $p(q,H_i)$ being related to the ratio of saturation magnetization M_s to the effective magnetic field $H_{\mathrm{eff}}(q,H_i)$ defined in Equation 2.42.

While the behaviour of S_{H} and S_{M} depends on the microstructural model chosen, in case the Fourier coefficients $|\widetilde{N}|^2$, $|\widetilde{M}_z|^2 \cong |\widetilde{M}_s|^2$ and $|\widetilde{\mathbf{H}_p}|^2$ depend only on the magnitude of the scattering vector q (i.e., in case of a statistically isotropic magnetic material), after performing 2π radial averages one finds that the response functions vary asymptotically

as [79]:

$$R_{\mathrm{H}}(q,\theta,H_i) \propto q^{-4}, \tag{2.55}$$

$$R_{\mathrm{M}}(q,\theta,H_i) \propto q^{-2}. \tag{2.56}$$

2.11.2 $\mathbf{k}_0 \parallel \mathbf{H}_0$

For the parallel scattering geometry ($\mathbf{H}_0 \parallel \mathbf{k}_0$) the unpolarized elastic differential SANS cross section $d\Sigma/d\Omega$ at momentum-transfer vector $\mathbf{q}$ can be written as [78, 92]:

$$\frac{d\Sigma}{d\Omega}^{\parallel}(\mathbf{q}) = \frac{8\pi^3}{V} b_H^2 \Big(b_H^{-2}|\widetilde{N}|^2 + |\widetilde{M}_x|^2 \sin^2\theta + |\widetilde{M}_y|^2 \cos^2\theta + |\widetilde{M}_z|^2 - (\widetilde{M}_x \widetilde{M}_y^* + \widetilde{M}_x^* \widetilde{M}_y) \sin\theta\cos\theta \Big). \tag{2.57}$$

Respectively, the residual cross section takes the form of:

$$\frac{d\Sigma}{d\Omega}^{\parallel}_{\mathbf{H}_{\mathrm{sat}}}(\mathbf{q}) = \frac{d\Sigma}{d\Omega}^{\parallel}_{\mathrm{res}}(\mathbf{q}) = \frac{8\pi^3}{V} b_H^2 \Big(b_H^{-2}|\widetilde{N}|^2 + |\widetilde{M}_z|^2 \Big). \tag{2.58}$$

Following the same logics as the perpendicular geometry case, at a finite non-saturating field $\mathbf{H}_0$ the spin-misalignment SANS cross section $\frac{d\Sigma_{\mathrm{SM}}}{d\Omega}$ is:

$$\frac{d\Sigma}{d\Omega}^{\parallel}_{\mathrm{SM}}(\mathbf{q},\mathbf{H}_0) = \frac{8\pi^3}{V} b_H^2 \Big(|\widetilde{M}_x|^2 \sin^2\theta + |\widetilde{M}_y|^2 \cos^2\theta - (\widetilde{M}_x \widetilde{M}_y^* + \widetilde{M}_x^* \widetilde{M}_y) \sin\theta\cos\theta \Big). \tag{2.59}$$

Micromagnetic representation

Equation 2.59 can be compactly written in terms of micromagnetic functions as [79, 47]:

$$\frac{d\Sigma}{d\Omega}^{\parallel}_{\mathrm{SM}}(\mathbf{q},\mathbf{H}_0) = S_{\mathrm{H}}(\mathbf{q}) R_{\mathrm{H}}(q,\theta,H_i), \tag{2.60}$$

where the response function simplifies to

$$R_{\mathrm{H}}(q,H_i) = \frac{p^2}{2}. \tag{2.61}$$

The quantity S_{H} again denotes the anisotropy-field scattering function, which is proportional to the magnitude square of the Fourier transform $\widetilde{\mathbf{H}}_p(\mathbf{q})$ of the magnetic anisotropy field $\mathbf{H}_p(\mathbf{r})$, i.e., $S_H \propto \widetilde{\mathbf{H}}_p^2(\mathbf{q})$. This function contains information on the strength and spatial

structure of the magnetic anisotropy field. In the approach-to-saturation regime, S_H is independent of the applied magnetic field.

Notably, in this geometry, $\frac{d\Sigma}{d\Omega}^{\parallel}_{\mathrm{SM}}(\mathbf{q}, \mathbf{H}_0)$ does not depend on $\widetilde{M}_z$ fluctuations, in other words, the inhomogeneities in the saturation magnetization are contained in the residual ($\frac{d\Sigma}{d\Omega}^{\parallel}_{\mathrm{res}}(\mathbf{q})$) scattering cross section. Additionally, even though the individual Fourier components ($|\widetilde{M}_x|$ and $|\widetilde{M}_y|$) are highly anisotropic, their sum in Equation 2.59 is isotropic (i.e. θ-independent) for statistically isotropic ferromagnets.

DMI contributions

Additionally, it should be noted that up to the transition to the micromagnetic functions (Equation 2.52 and Equation 2.60) one could explicitly account for the DMI (refer to Equation 2.40 and Equation 2.41 as well as Equation 2.43/Equation 2.44 and Equation 2.45/Equation 2.46 for perpendicular and parallel geometry respectively).

2.12 Summary

Essentially, the take-away from this chapter is the tool-kit necessary to tackle the data analysis in the following chapters. The micromagnetic theory provides a robust way of analyzing any and all neutron scattering data - provided the condition of the approach-to-saturation. Moreover, the different contributions to the effective field (Equation 2.36) can be explored both individually and in conjunction with one another which naturally opens a plethora of simulation work. The rest of this work will rely heavily on the results of this chapter to provide insights into the material properties by always combining the analysis of the experimental data with numerical analysis stemming from the micromagnetic theory. Note that, even though the details on the data reduction are not explicitly discussed unless absolutely necessary, the rigorous measurements of references and all the equipment-related corrections are of enormous importance to the successful - and reliable - data analysis. Thus, every (cm^{-1}) unit of the cross section hides cumulative years of efforts of dozens of contributors to the data processing software packages such as [23, 56, 102, 63].

In the next chapter, the micromagnetic functions in the parallel geometry would be analyzed in detail to yield a completely new way of treating magnetic SANS data through the introduction of the magnetic Guinier law.

Chapter 3

Magnetic Guinier Law

This chapter presents the newly established theory of the magnetic Guinier law and provides the experimental results. It expands on the [83] and adds to both the discussion and the data presented in the original paper.

3.1 Particle size and Guinier law

The determination of particle sizes is one of the most important daily tasks in many branches of the natural sciences [27]. Particle sizes in the micrometer regime and above can be routinely determined using optical microscopy, yet the nanoparticles (with $D \simeq 1 - 100\,\mathrm{nm}$) require electron microscopy (scanning and/or transmission) or scattering methods (such as dynamic light, x-ray or neutron scattering). While the former microscopy techniques inherently suffer from low statistics and a small probed area, the latter scattering ones have the advantage of providing statistically-averaged information over a large volume and a considerable number of particles. Small-angle scattering, using either x-rays or neutrons, is one of the most popular methods for analyzing structures on this mesoscopic length scale, widely employed in a broad range of research topics from condensed-matter and soft-matter physics, physical chemistry, biology, and materials science [121].

A typical 2π-radially averaged result of a scattering experiment appears on Figure 3.1(a). Two asymptotic regimes - a high-q (also known as the Porod regime) and a low-q (also known as the Guinier regime) are often the focus of the data analysis [104, 27]. The Porod regime gives information on the particle surfaces and the low-q Guinier regime, which is the focus of the present study, gives the information on the particle size.

If the scattering is from a dilute and monodisperse set of particles with sharp interfaces, then the Guinier law describing the (elastic) small-angle scattering of x-rays and neutrons near the origin ($q < 1.3/R_G$) of the reciprocal space applies [37], and the macroscopic

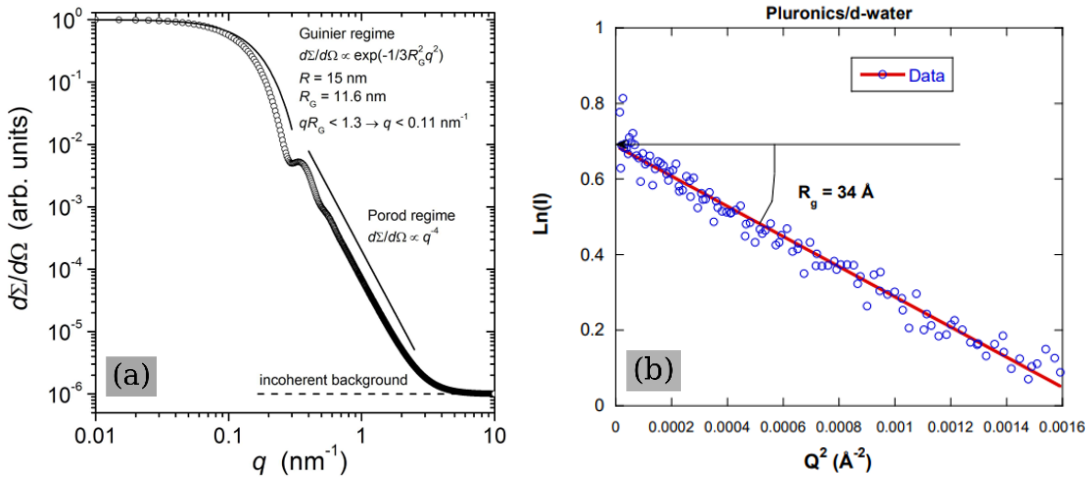

Fig. 3.1 (a) A sample SANS data with the asymptotic Guinier and Porod regimes marked (taken from [71]). (b) A sample Guinier plot (adapted from [41]).

differential scattering cross section $d\Sigma/d\Omega$ can be expressed as [104, 27]:

$$\frac{d\Sigma}{d\Omega}(q) \cong \frac{d\Sigma}{d\Omega}(q=0)\, e^{-\frac{q^2 R_G^2}{3}}, \tag{3.1}$$

where the forward scattering cross section $\frac{d\Sigma}{d\Omega}(0)$ is proportional to the squared total excess scattering length of the particle, and R_G denotes the particle's radius of gyration. Notably, the Equation 3.1 is valid for arbitrary particle shapes.

The (linear) Guinier plot of $\ln(d\Sigma/d\Omega)$ *vs.* q^2 can be easily constructed (see Figure 3.1(b)) and the R_G, which is related to the particle size, (*e.g.*, $R_G^2 = \frac{3}{5}R^2$ for a sphere of radius R) easily determined. The Guinier law is often the first stage of the data analysis and is of outstanding importance for the analysis of small-angle scattering data, particularly in soft matter physics [35].

3.2 Magnetic Guinier law – the concept

Conceptually, the magnetic characteristic length is represented on Figure 3.2: the distortion of the anisotropy field due to the defect extends into the material over many lattice sites. Magnetic SANS is one of the few techniques that could map such spin disorders in the bulk. Conceptually, the situation is not far dissimilar from the flow disturbance introduced by a stationary particle into a flowing liquid matrix. Thus, one might attempt to represent the extent of the spin disorder through a "magnetic radius of gyration".

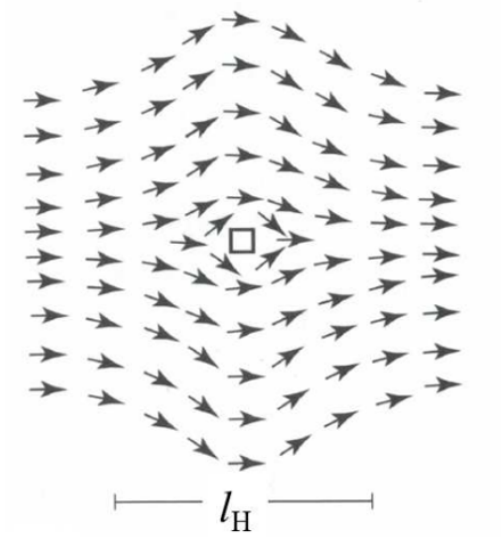

Fig. 3.2 Schematic depiction of the spin disorder around a point defect (vacancy) and associated characteristic micromagnetic exchange lenght l_H. Adapted from [79].

From the discussion in the section 3.1, it should be clear that originally the Guinier law has been derived in the context of the developments of the small-angle x-ray scattering [37] for the determination of the particle size in the *nonmagnetic* particle-matrix-type systems. Therefore, its application to the magnetic materials has never been tried before the work in [79] and should be considered with special care.

The Guinier law should be applicable to systems consisting of saturated and homogeneous magnetic particles in a nonmagnetic and homogeneous matrix or, similarly, to pores in a saturated matrix. In this context Burke [13] investigated the influence of magnetic shape anisotropy on the Guinier law of fine ferromagnetic *single-domain* particles. Yet, when the sample is *inhomogeneously* magnetized, i.e., when the magnitude and orientation of the magnetization vector field $\mathbf{M}$ varies continuously with the position $\mathbf{r}$ inside the material on the nanometer scale, then a central assumption of the Guinier law - that of domains (particles) are separated by sharp interfaces from the matrix - is violated. Thus, the Equation 3.1, with a constant (and field-independent) R_G, cannot describe the low-q region of the magnetic SANS cross section.

Intuitively, an effective magnetic Guinier radius is expected to depend on the applied magnetic field as well as on the magnetic interactions (e.g., exchange, anisotropy, magnetostatics). In the following the magnetic Guinier law is derived on the basis of the micromagnetic theory and the analysis of the experimental SANS data of the nanocrystalline Co is provided.

3.3 Magnetic Guinier law in the context of the micromagnetic theory

Here and in [83] the discussion is limited to the parallel geometry only, mostly due to the simplicity of the micromagnetic representation (compare Equation 2.60 and Equation 2.61). The same approach could be applied in the perpendicular case if one were to consider a narrow section around $\theta = 0$ or $\theta = 180$, since then the longitudinal magnetization scattering function $S_{\mathrm{M}}(\mathbf{q})$ tends to zero (compare Equation 2.60 and Equation 2.54), but, at the moment, this is beyond the scope of this work.

Further, the spin-misalignment SANS cross section

$$\frac{d\Sigma_{SM}^{\parallel}}{d\Omega} = S_{\mathrm{H}}(\mathbf{q}) R_{\mathrm{H}}(q, \theta, H_i)$$

is analyzed in the low-q regime to derive a Guinier expression for the magnetic SANS analogous to the Equation 3.1.

3.3.1 Response function R_{H}

Inserting the definition of $p(q, H_i)$ (see Equation 2.42) into the response function $R_{\mathrm{H}}(q, H_i)$ (see Equation 2.61) yields:

$$R_{\mathrm{H}}(q, H_i) = \frac{p^2(q, H_i)}{2} = \frac{1}{2}\left(\frac{M_s}{H_i(1 + l_{\mathrm{H}}^2 q^2)}\right)^2.$$

Respectively, a simple way of analyzing $R_{\mathrm{H}}(q, H_i)$ in the low-q range would be to take the Taylor expansion around $q = 0$:

$$\begin{aligned} R_{\mathrm{H}}(q, H_i)\Big|_{q\to 0} &\cong \frac{p_0^2}{2}\left(1 - 2l_{\mathrm{H}}^2 q^2\right) \cong \frac{p_0^2}{2}\exp\left(-2l_{\mathrm{H}}^2 q^2\right) \\ &= \frac{p_0^2}{2}\exp\left(-\frac{q^2}{3} 6 l_{\mathrm{H}}^2\right) \end{aligned} \tag{3.2}$$

where $p_0 = p(q = 0) = M_s/H_i$. The validity range of this approximation as well as the deviations from the exact form are demonstrated on Figure 3.3.

3.3.2 Scattering function S_{H}

The low-q expansion of the scattering function is a more involved process. As per micromagnetic theory, $S_{\mathrm{H}}(\mathbf{q})$ is proportional to the magnitude square of the FT of the anisotropy field (see the discussion in subsection 2.11.2):

$$S_H \propto \widetilde{\mathbf{H}}_p^2(\mathbf{q}),$$

and contains the information on the vectorial structure (i.e., the variations in amplitude and direction) of the magnetic anisotropy field $\mathbf{H}_p(\mathbf{r})$. Respectively, it depends on the sample's microstructure.

In the following, the discussion is limited to the isotropic case only, i.e., there are no correlations between the individual defects (*e.g.*, crystallites separated by grain boundaries) and there is a statistical distribution in orientation and/or magnitude of the magnetic anisotropy field. This assumption is definitely applicable to an idealized nanocrystalline ferromagnet, where the crystallites (*i.e.*, "magnetic defects") have random crystallographic orientation and where the anisotropy field arises exclusively from the magnetocrystalline anisotropy. Additionally, the sample volume probed by the neutrons typically contains many such defects.

A further assumption is that the total magnetic anisotropy field of the sample $\mathbf{H}_p(\mathbf{r})$, is the sum of the anisotropy fields of individual defects "*i*" [125, 126], *i.e.*:

$$\mathbf{H}_p(\mathbf{r}) = \sum_{i=1}^{N} \mathbf{H}_{p,i}(\mathbf{r}). \tag{3.3}$$

Then, the same summation applies to the Fourier transform $\widetilde{\mathbf{H}}_p(\mathbf{q})$ of $\mathbf{H}_p(\mathbf{r})$:

$$\widetilde{\mathbf{H}}_p(\mathbf{q}) = \sum_{i=1}^{N} \widetilde{\mathbf{H}}_{p,i}(\mathbf{q}). \tag{3.4}$$

Thus,

$$S_H \propto \widetilde{\mathbf{H}}_p^2(\mathbf{q}) = \left| \sum_{i=1}^{N} \widetilde{\mathbf{H}}_{p,i}(\mathbf{q}) \right|^2.$$

Respectively, assuming the $\widetilde{\mathbf{H}}_{p,i}$ are real-valued quantities, the square of Equation 3.4 yields:

$$\widetilde{\mathbf{H}}_p^2 = \sum_{i=1}^{N} \widetilde{\mathbf{H}}_{p,i}^2 + \sum_{i \neq j}^{N} \widetilde{\mathbf{H}}_{p,i} \cdot \widetilde{\mathbf{H}}_{p,j}. \tag{3.5}$$

If the $\widetilde{\mathbf{H}}_{p,i}$ of the individual defects are statistically uncorrelated (isotropic case), then terms $\widetilde{\mathbf{H}}_{p,i} \cdot \widetilde{\mathbf{H}}_{p,j}$ with $i \neq j$ take both signs with equal probability. Thus, the sum over these mixed terms vanishes, and:

$$\widetilde{\mathbf{H}}_p^2(\mathbf{q}) = \sum_{i=1}^{N} \widetilde{\mathbf{H}}_{p,i}^2(\mathbf{q}), \tag{3.6}$$

and

$$S_H \propto \widetilde{\mathbf{H}}_p^2(\mathbf{q}) = \left| \sum_{i=1}^{N} \widetilde{\mathbf{H}}_{p,i}(\mathbf{q}) \right|^2 = \sum_{i=1}^{N} \left| \widetilde{\mathbf{H}}_{p,i}(\mathbf{q}) \right|^2.$$

Equation 3.6 implies that given the solution for the single-defect case $\widetilde{\mathbf{H}}_{p,i}(\mathbf{q})$, the total anisotropy contribution $\widetilde{\mathbf{H}}_p^2$, and hence $S_H \propto \widetilde{\mathbf{H}}_p^2$, can be computed for an arbitrary arrangement of defects.

In an idealized nanocrystalline ferromagnet each grain is a single crystal and the anisotropy field in the grain is a constant vector, i.e., $\mathbf{H}_{p,i} \neq \mathbf{H}_{p,i}(\mathbf{r})$, and the single grain anisotropy field Fourier amplitude is obtained by the following form-factor integral [126]:

$$\widetilde{\mathbf{H}}_{p,i}(\mathbf{q}) = \frac{\mathbf{H}_{p,i}}{(2\pi)^{3/2}} \int_{V_{p,i}} e^{-i\mathbf{q}\cdot\mathbf{r}} d^3 r, \tag{3.7}$$

where the integral extends over the volume of the grain i. For an example of a spherical grain shape ($V_{p,i} = \frac{4\pi}{3} R_i^3$), the well-known result:

$$\widetilde{\mathbf{H}}_{p,i}(\mathbf{q}) = \widetilde{\mathbf{H}}_{p,i}(qR_i) = \frac{\mathbf{H}_{p,i}}{(2\pi)^{3/2}} 3V_{p,i} \frac{j_1(qR_i)}{qR_i}, \tag{3.8}$$

is obtained, where $j_1(z)$ denotes the spherical Bessel function of the first order.

The square of Equation 3.8) is identical (except for the prefactor) to the nuclear SANS cross section of an array of noninterfering spherical particles[126], and asymptotic results at small and large q are applicable; in particular, introducing the "radius of gyration of the magnetic anisotropy field" R_{GH}, in the low-q Guinier regime:

$$S_{\mathrm{H}}(q)\Big|_{q\to 0} \cong S_{\mathrm{H}}(0) \exp\left(-\frac{q^2}{3} R_{GH}^2\right). \tag{3.9}$$

Notably, R_{GH} may be seen as a measure for the size of regions over which the magnetic anisotropy field $\mathbf{H}_p(\mathbf{r})$ is homogeneous, similar to nuclear SANS and SAXS, where R_G is a measure for the particle size.

In the special case of an idealized nanocrystalline ferromagnet (random anisotropy and magnetocrystalline anisotropy only), R_{GH} is closely related to the crystallite size[83].

3.3.3 Magnetic SANS cross section in the low-q limit

Inserting the low-q expansions of the response function (Equation 3.2) and the scattering function (Equation 3.9) into the SANS cross section $d\Sigma_{SM}/d\Omega = S_{\mathrm{H}} R_{\mathrm{H}}$ yields:

$$\begin{aligned}
\left.\frac{d\Sigma_{SM}}{d\Omega}^{\parallel}\right|_{q\to 0} &\cong S_{\mathrm{H}}(0)\ \exp\left(-\frac{q^2}{3}R_{GH}^2\right)\frac{p_0^2}{2}\exp\left(-\frac{q^2}{3}6l_{\mathrm{H}}^2\right) \\
&= S_{\mathrm{H}}(0)\frac{p_0^2}{2}\exp\left((-\frac{q^2}{3}R_{GH}^2)+(-\frac{q^2}{3}6l_{\mathrm{H}}^2)\right) \\
&= S_{\mathrm{H}}(0)\frac{p_0^2}{2}\exp\left(-\frac{q^2}{3}(R_{GH}^2+6l_{\mathrm{H}}^2)\right) \\
&= \left.\frac{d\Sigma_{SM}}{d\Omega}\right|_{(q=0)}\exp\left(-\frac{q^2R_{GSM}^2}{3}\right),
\end{aligned} \tag{3.10}$$

where R_{GSM}^2 is defined as (see Equation 2.38 for l_{H} definition):

$$R_{GSM}^2(H_i) = R_{GH}^2 + 6l_{\mathrm{H}}^2(H_i) = R_{GH}^2 + \frac{12A}{\mu_0 M_s H_i} \tag{3.11}$$

and represents the field-dependent magnetic Guinier radius.

The observation that R_{GSM} depends on R_{GH} and on the micromagnetic exchange length l_{H} is a manifestation of the fact that the magnetic microstructure in real space corresponds to the convolution of the nuclear grain microstructure (R_{GH}) with field-dependent micromagnetic response functions (l_H).

Note that since $\frac{d\Sigma_{SM}}{d\Omega}(0) \propto p_0^2 \propto H_i^{-2}$ [compare Eq. (2.42)], $\frac{d\Sigma_{SM}}{d\Omega}(0,H_i)$ can be used to test the validity of the present derivation in a given q-range.

3.4 Validity range of the magnetic Guinier law

Prior to the look at the actual experimental data, the validity range and the potential caveats in the Magnetic Guinier Law analysis need to be discussed.

3.4.1 Larger-q deviations

The "conventional" Guinier Law has a distinct cut-off at $q > 1.3/R_G$ [104, 27, 59, 106]. Notably, it is not a hard cut-off but merely a point where deviations become considerable. Also, the value of 1.3 is not universal, the values from 1.1 [9] up to 2 [133] are quoted, depending on the system and additional corrections. Within the magnetic Guinier law there is no established cut-off as of yet. The Figure 3.3 points to purely mathematical deviation (*i.e.*, on the basis of Taylor expansion) from the expected behavior.

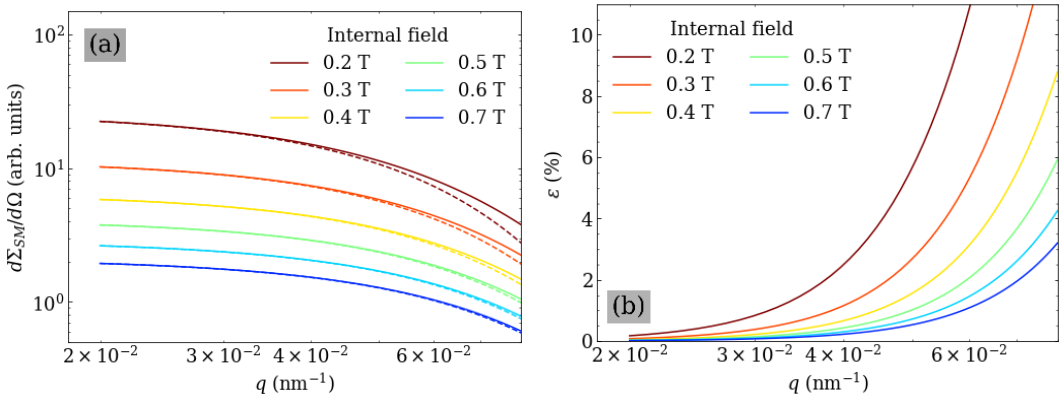

Fig. 3.3 Larger-q limits of the magnetic Guinier theory approximations for the material parameters of $R_{GH} = 20.5\,\text{nm}$, $A = 1.5\times10^{-11}\,\text{J/m}$, $\mu_0 M_s = 1.80\,\text{T}$ [83]. (a) Comparison between $d\Sigma_{SM}/d\Omega$ (solid lines, Equation 2.59) and the Guinier approximation [dashed lines, Equation 3.10] at selected internal-field values (see inset) (log-log scale). (b) Relative error of the Guinier approximation. Plotted is the quantity $\varepsilon(q,H_i) = \sqrt{(f-f_G)^2}/f$, where $f = d\Sigma_{SM}/d\Omega$ (Equation 2.59 and Equation 2.60) and f_G is the Guinier approximation (Equation 3.10). Taken from the Supplementary Material of [83].

Naturally, this is but a narrow selection of fields and material parameters, yet this error is in-built in the Taylor expansion (see Equation 3.2) and it would be pointless to extend the Guinier analysis to larger q values given the same material parameters.

3.4.2 l_H variations

The second potential problem might arise if the field-dependent part ($\propto l_\text{H}^2$) of the R_{GSM} is small compared to the field-independent part R_{GH}. Figure 3.4 represents the variation of the micromagnetic exchange length l_H over a typical range of applied fields in a SANS experiment *not* designed with the intention of performing the Guinier analysis (based on the data in [7]). Clearly, since there is very little variation in the l_H in the experimentally-accessed high-field regime, the R_{GSM} variations extracted would be small as well and, potentially, well within the error bars after the final analysis.

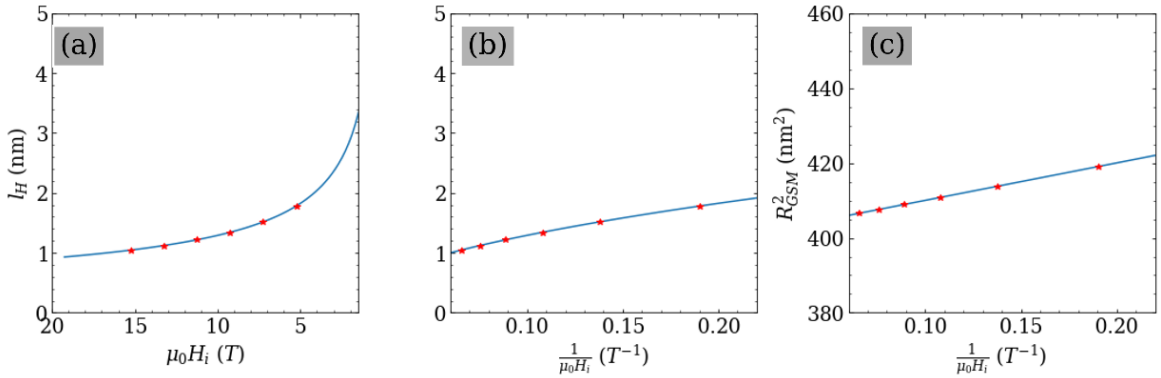

Fig. 3.4 Expected l_H variation in a typical SANS experiment. Plots of l_H as a function of the internal field $\mu_0 H_i$ (a) and its inverse (b) indicate that the variation of l_H is very small in the experimentally accessed range of fields (represented with "★")[7]. Respectively, the variation of R^2_{GSM} (c) is small as well. ($A = 12.5$ pJ/m; $\mu_0 M_s = 1.5$ T; $N = 0.5$ were used). Taken from [71].

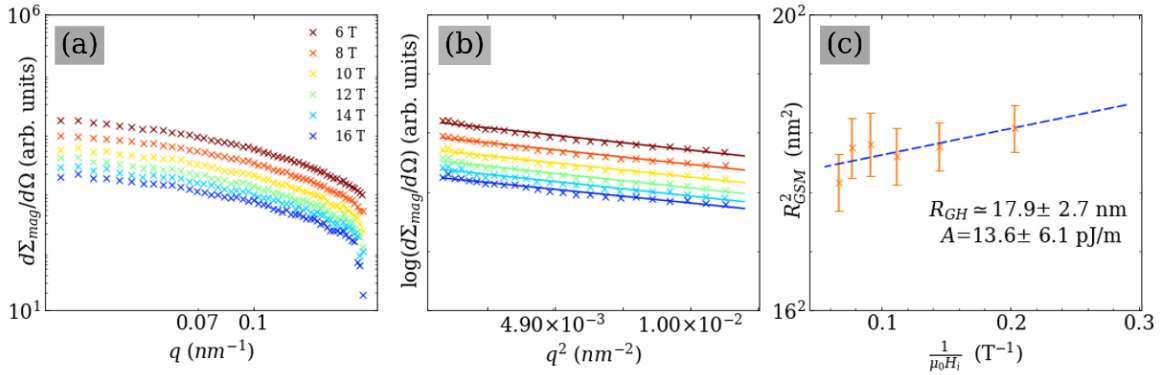

Fig. 3.5 Summary plots of the Nd-Fe-B-based hard magnetic composite. (a) Magnetic SANS cross sections at the selection of applied field. (b) Guinier plots of the same data. (c) Plot of R^2_{GSM} *vs.* H_i^{-1} and fit (dashed line) to Equation 3.11. Taken from [71].

Consequently, the Figure 3.5 presents the magnetic Guinier law analysis of such data from [7] on a Nd-Fe-B-based hard magnetic composite. Yet, even with such a small variation, where the relative differences between the R_{GSM} values at the highest and lowest field are, arguably, comparable to their errors, the Magnetic Guinier analysis results in exchange stiffness constant $A \simeq 13.6 \pm 6.2$ pJ/m which coincides with the value obtained *via* the micromagnetic route ($A_{\mu mag} \simeq 13.1 \pm 3.2$ pJ/m) and the radius of gyration is comparable with the particle size $d \simeq 22$ nm [7].

3.5 Experimental results on nanocrystalline Co

This section briefly summarizes the results of [83].

3.5.1 Samples and neutron experimental details

The nanocrystalline Co sample under study was synthesized via pulsed electrodeposition and was kindly provided by Professor Uwe Erb from the University of Toronto. This particular sample has been extensively studied in the past using magnetometry, wide-angle X-ray diffraction, as well as both unpolarized and spin-polarized SANS (e.g., [88, 126, 86, 45, 78, 77]). Notably, it is a fully dense polycrystalline bulk metal with a nanometer grain size (average crystallite size: $D = 9.5 \pm 3.0\,\mathrm{nm}$ [126]).

The SANS sample consisted of a single circular disk. Based on the thickness ($80\,\mu\mathrm{m}$) and the diameter ($2\,\mathrm{cm}$) of the disk, a demagnetizing factor of $N \cong 0.994$ was computed for the $\mathbf{k}_0 \parallel \mathbf{H}_0$ geometry as per [99]. In the following, all the reported field values are corrected for demagnetizing effects.

The SANS experiment was conducted at $300\,\mathrm{K}$ at the instrument D11 at the Institut Laue-Langevin, Grenoble. The unpolarized incident neutrons with a mean wavelength of $\lambda = 6.0$ and a bandwidth of $\Delta\lambda/\lambda = 10\,\%$ (FWHM) were used. The instrument offers access to a low q-range of $0.016\,\mathrm{nm}^{-1} \lesssim q \lesssim 0.2\,\mathrm{nm}^{-1}$. The external magnetic field $\mathbf{H}_0$ (with $\mu_0 H_0^{\max} = 16.5\,\mathrm{T}$) was provided by a 17 T cryomagnet [44] and was applied parallel to the wave vector $\mathbf{k}_0$ of the incoming neutron beam (see the Figure 2.5(b) for a sketch of the neutron setup). To reduce the influence of inhomogeneous demagnetizing fields at the outer perimeter of the circular sample, the neutron beam was collimated to a diameter of $0.8\,\mathrm{cm}$. The neutron transmission was larger than $90\,\%$ in all measurements, indicating a negligible influence of multiple scattering.

3.5.2 Unpolarized SANS results and discussion

Although the individual scattering contributions to the scattering cross section in Equation 2.57 are highly anisotropic[1], their sum results in an isotropic cross section for a statistically isotropic sample [79]. Thus, the two-dimensional SANS intensity distributions of the nanocrystalline Co sample are isotropic (θ-independent) at all fields investigated (Figure 3.6). This supports the assumption made earlier in the micromagnetic theory of a statistically-isotropic grain microstructure.

[1] Due to the trigonometric functions and the fact that magnetization Fourier components themselves may depend on the angle θ explicitly (see Equation 2.45 and Equation 2.46).

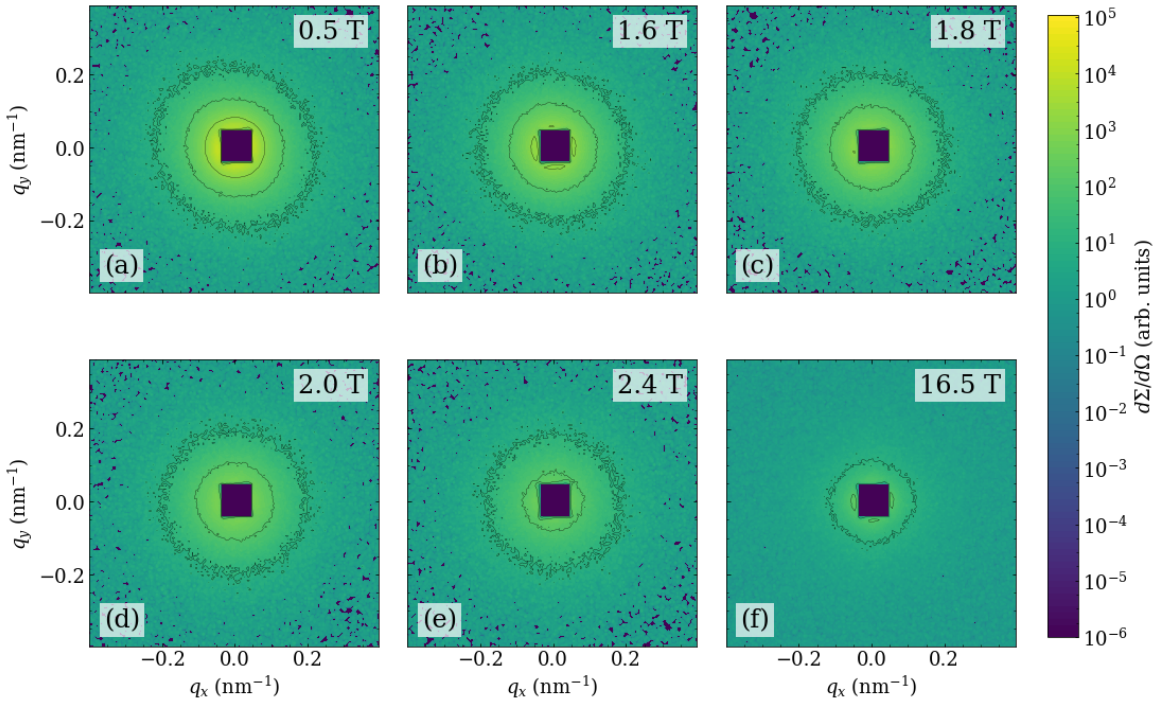

Fig. 3.6 Two-dimensional unpolarized total (nuclear and magnetic) SANS cross section $d\Sigma/d\Omega$ of nanocrystalline cobalt at selected applied magnetic fields $\mathbf{H}_0$ (see insets) (logarithmic color scale). $\mathbf{H}_0 \parallel \mathbf{e}_z$ is applied parallel to the wave vector $\mathbf{k}_0$ of the incident neutrons. Taken from the supplementary material of [83].

These two-dimensional total (nuclear and magnetic) SANS intensity maps were azimuthally-averaged over an angle of 2π. To apply Equation 3.10 and Equation 3.11 to $d\Sigma_{SM}/d\Omega$ data (compare Equation 2.59)), the residual SANS cross section $d\Sigma_{\text{res}}/d\Omega$ was subtracted from the total $d\Sigma/d\Omega$ at lower fields. In this experiment, the highest internal field achieved was 14.71 T. This procedure removes any background scattering contribution as well as the nuclear and the longitudinal magnetic scattering, leaving only the magnetic scattering cross section (see section 2.10 and section 2.11 for more details). The subtraction procedure (for the radially-averaged data) along with the room-temperature magnetization curve is depicted on Figure 3.7.

As seen from the Figure 3.7(c), the magnetization state of the specimen used in the SANS experiment (indicated by "⬢") is mostly within the approach-to-saturation regime defined here as the $\mu_0 H_i \gtrsim 0.27\,\text{T}$ ($M/M_s \gtrsim 96\,\%$. The strong field dependence of $d\Sigma_{SM}/d\Omega$ supports the notion that scattering due to transversal spin misalignment represents by far the dominant contribution to $d\Sigma/d\Omega$ (see also Figure 3 in [78]).

The magnetic Guinier analysis is represented on Figure 3.8. The Guinier plots, i.e., $\ln[d\Sigma_{SM}/d\Omega]$ *vs.* q^2, along with the weighted linear least-squares fits to Equation 3.10

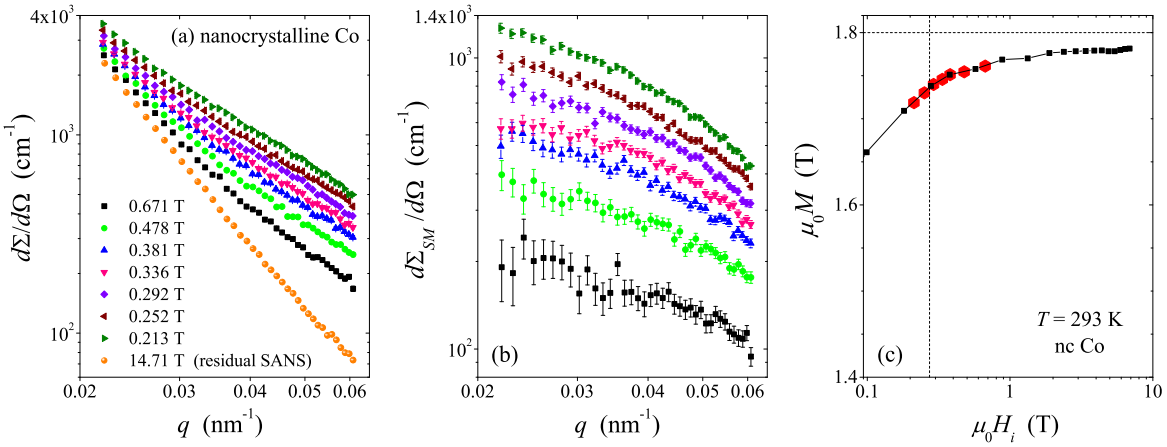

Fig. 3.7 (a) 2π-azimuthally-averaged total (nuclear and magnetic) SANS cross section $d\Sigma/d\Omega$ of nanocrystalline Co *vs.* momentum transfer q at a series of internal magnetic fields (see inset) (log-log scale) ($\mathbf{k}_0 \parallel \mathbf{H}_0$). (b) Corresponding spin-misalignment SANS cross section $d\Sigma_{SM}/d\Omega$ obtained by subtracting the $d\Sigma/d\Omega$ data at 14.71 T [orange data points in (a)] from the $d\Sigma/d\Omega$ at lower fields. (c) Upper right quadrant of the hysteresis loop of nanocrystalline Co measured at decreasing fields from saturation as in the neutron experiment. "⬢" indicate the internal-field values where the SANS data were taken. Horizontal dashed line indicates the saturation-magnetization value of $\mu_0 M_s = 1.80\,\mathrm{T}$. Vertical dashed line indicates the approach-to-saturation regime ($M/M_s \gtrsim 96\,\%$). Taken from [83].

are shown in Figure 3.8(a), whereas Figure 3.8(b) presents the obtained R^2_{GSM} together with a weighted linear least-squares fit to Equation 3.11 (as a function of H_i^{-1}). In Figure 3.8(c) the field dependence of $d\Sigma_{SM}/d\Omega(q=0)$ is displayed as an afore-mentioned (see subsection 3.3.3) consistency check.

Under careful scrutiny of Figure 3.8(a) a slight upward curvature becomes visible at the smallest q at the two smallest internal fields of 0.213 T and 0.252 T. In line with this observation the data set in Figure 3.8(c) starts to deviate from the expected linear behavior for these two smallest internal fields (open symbols). This discrepancy is explained with growing deviations from the small-misalignment (*i.e.*, approach to saturation) approximation for decreasing fields, and can be taken as a criterion for the validity range of the approach. Therefore, the two data points at 0.213 T and 0.252 T were excluded from the subsequent Guinier analysis. The values of $R_{GH} = 20.5 \pm 1.2\,\mathrm{nm}$ and $A = (1.5 \pm 0.2) \times 10^{-11}\,\mathrm{J/m}$ were thus obtained. The A-value perfectly fits within the range of values reported in the literature [62, 115], while the R_{GH}-value corresponds to a spherical particle radius of $R \cong 26.5\,\mathrm{nm}$, assuming the monodisperse particles relation $R^2_{GH} = \frac{3}{5}R^2$. This value is larger than

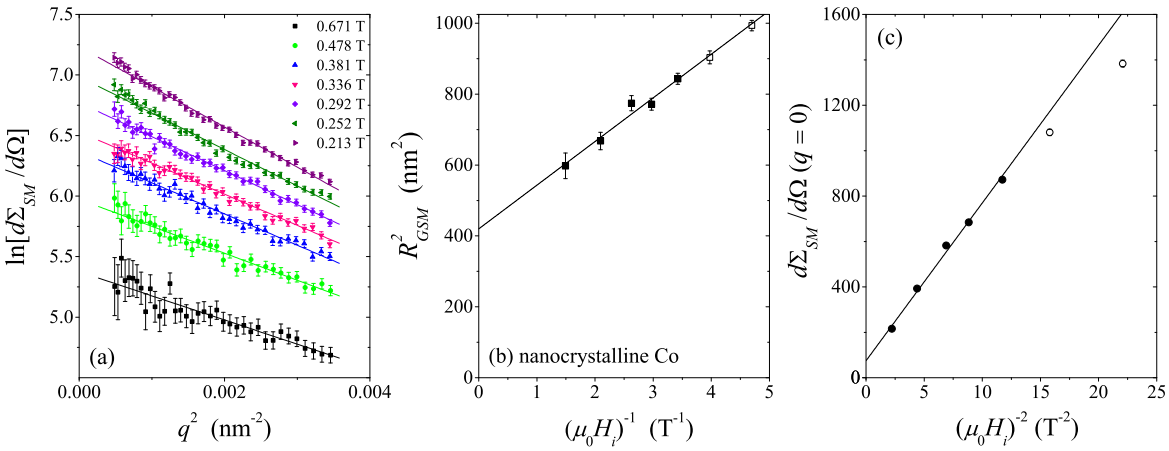

Fig. 3.8 Magnetic Guinier analysis on nanocrystalline Co. (a) Guinier plot $\ln[d\Sigma_{SM}/d\Omega]$ *vs.* q^2 and fits (solid lines) to Eq. (3.10) at selected values of the internal magnetic field (see inset). (b) Plot of R^2_{GSM} *vs.* H_i^{-1} and fit (solid line) to Eq. (3.11). In the fitting routine R_{GH} and A were treated as adjustable parameters. (c) Field dependence of $\frac{d\Sigma_{SM}}{d\Omega}(q=0)$. Solid line: $\frac{d\Sigma_{SM}}{d\Omega}(q=0) \propto H_i^{-2}$. In (b) and (c) the last two data points (open symbols), corresponding to internal fields of 0.213 T and 0.252 T, have been excluded from the fit analysis. Taken from [83].

the average crystallite size of 10 nm (determined by the X-ray diffraction), which can be naturally explained by the presence of a particle-size distribution in the Co sample[2].

Lastly, as can be seen in Figure 3.8(c), the extrapolated forward-scattering cross section $\frac{d\Sigma_{SM}}{d\Omega}(q=0)$ also obeys the predicted $\frac{d\Sigma_{SM}}{d\Omega}(q=0) \propto H_i^{-2}$ scaling (compare Equation 3.2).

3.6 Summary

Based on the continuum theory of micromagnetics the magnetic Guinier law for random-anisotropy-type ferromagnets (Equation 3.10 and Equation 3.11) was established. The key variable of the theory - the magnetic Guinier radius R_{GSM} - depends on both the sample microstructure (via nuclear grain structure and the resulting anisotropy-field) and on the magnetic interactions (exchange-stiffness constant, saturation magnetization, applied field). R_{GSM} can be quite straight-forwardly determined by analyzing the magnetic SANS cross section at a range of applied fields.

[2]It is well-known from the nuclear SANS theory that a size distribution strongly weighs the R_G-value towards the largest features in the distribution; for instance, for spherical particles and point collimation, R_G^2 is then related to the ratio of the eighth over the sixth moment of the size distribution [61, 27]. Therefore, for the determination of the scaling relation between R_{GH} and the average crystallite size, knowledge on the particle-size distribution is required.

The validity range of the magnetic Guinier law was discussed, the methodology was tested against the data of [7] and the derived material constants and parameters agreed very well with the results of the original study obtained via the complete micromagnetic routine. Finally, the approach was subject to a rigorous testing by analyzing experimental data on nanocrystalline cobalt [79].

Thus, this method is easily applicable to magnetic materials using unpolarized neutrons.

Chapter 4

Magnetic Correlations in Rare-Earth-Free Mn – Bi Magnets

4.1 Mn – Bi — a promising rare-earth-free permanent magnet

Permanent magnets, being of a paramount importance to any electric motor, are of utmost importance in the modern society. It was estimated in 2010s [67] that in a developed country over 60% of electricity consumed is due to electric motor drives. Now, with the undeniable increase in demand for the electric transportation, this figure will keep rising. Thus, any improvement in efficiency of motors, generators and power converters will have a net positive impact.

The dominant permanent magnets are the NdFeB-based performance hard magnets and the Ferrite-based soft magnets. The high-performance ones contain both light rare earth (Nd, Pr) and a small amount of heavy rare earth (Dy, Tb) elements. Thus, the increased demand for the raw magnetic materials brings about geopolitical strain, since the majority of rare-earth production (over 90% as per 2011 [38]) are either in or owned by a single country.

Moreover, there is a significant performance gap (see Figure 4.1) between the ferrites and rare-earth magnets. Thus, the prospect to fill the gap with something cheap and effective is a lucrative one [18]. Such a material could be used as a substitute in both ferrite-based applications (to reduce the size and weight or enhance performance) and in rare-earth-based applications (to reduce the cost at the expense of the increased size and weight).

All these combined drive the acceleration of research of rare-earth free (RE-free further) permanent magnet candidates [39, 114, 109, 64, 97, 3, 19].

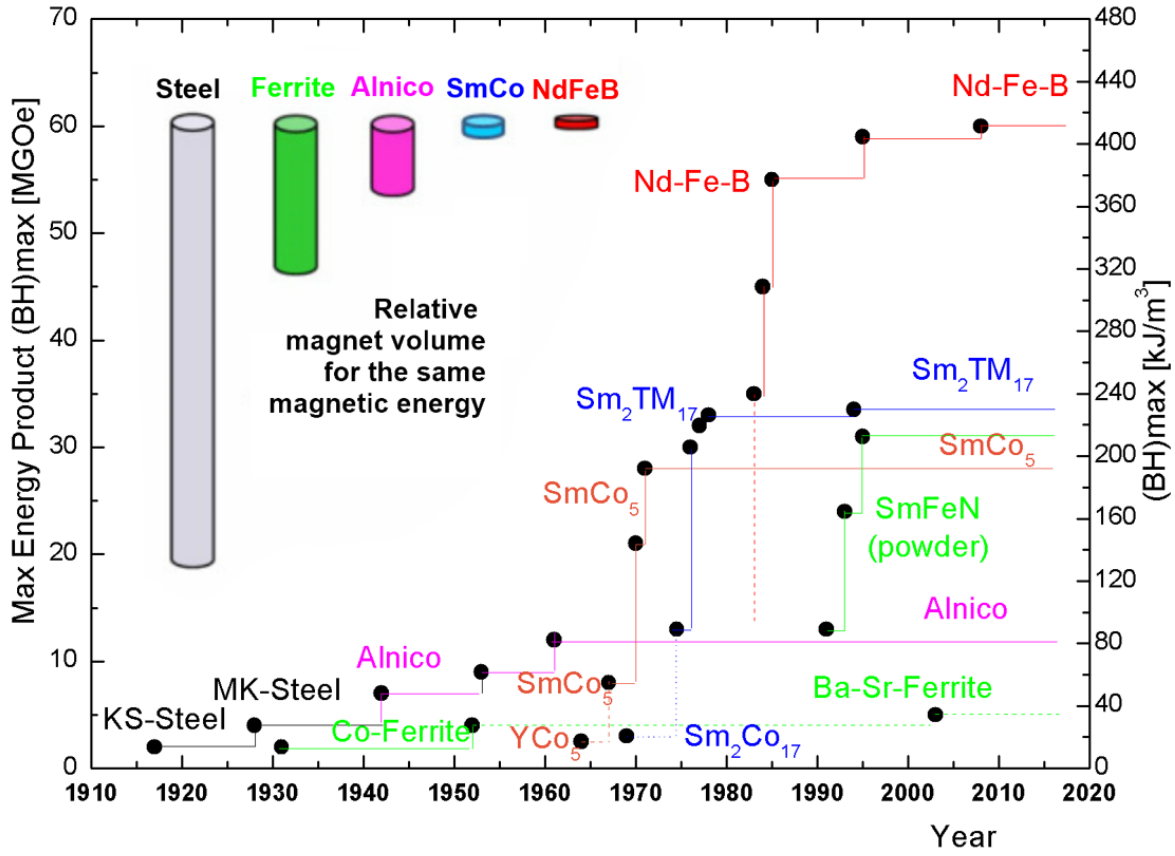

Fig. 4.1 Development in the energy density (BH_{max}) at room temperature of hard magnetic materials in the 20th century and presentation of different types of materials with comparable energy density (each magnet is designed so that at a reference point 5 mm from the surface of the pole, a field of 100 mT is produced). Adapted from [39].

4.1.1 Mn-based abundance

Mn-based magnets are a potential candidate for "plugging the gap" [19, 26, 55, 54] partially due to the ability of manganese to carry a large magnetic moment in some of its compounds [19] and partially due to its availability and cost. Figure 4.2(a) presents several such Mn-based magnets [114].

The low-temperature phase of Mn – Bi binary alloy [100, 68, 3, 16, 60, 95] has received a lot of attention lately, partially because of a positive temperature coefficient of the magnetic anisotropy rendering high-temperature applications attractive [16] and partially because Bi, being a by-product of lead production, is fairly inexpensive at present [19]. Yet, the natural rarity of Bi might result in a considerable increase in prices were the Mn – Bi demand increase, though the total cost is still expected to be lower than that of a NdFeB magnet [122]. The highest reported $(BH)_{max}$ value is 62.1 kJm^{-3} (7.8 MGOe), from the pre-aligned

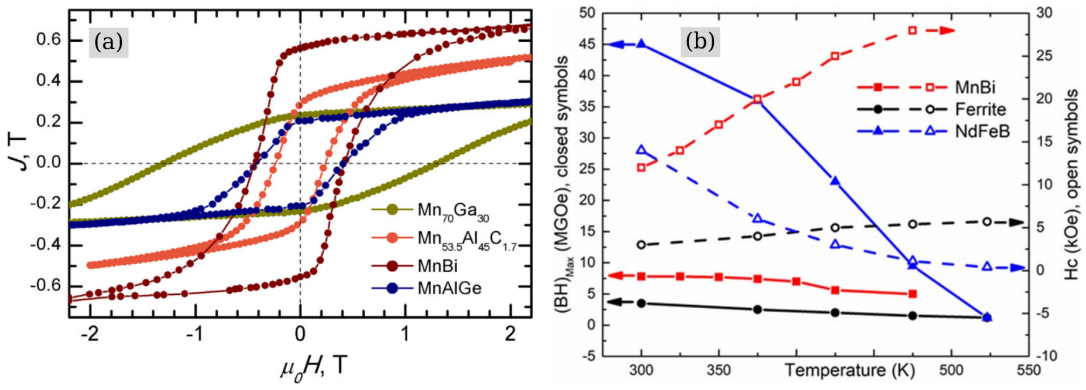

Fig. 4.2 (a) Hysteresis loops for Mn-based $Mn_{70}Ga_{30}$, $Mn_{53.5}Al_{45}C_{1.7}$, MnBi and MnAlGe RE-free permanent magnets. Adapted from [114]. (b) Comparison of magnetic properties of MnBi, Nd-Fe-B, and ferrite at different temperatures. Taken from [122].

sintered magnets [20]; however, it is less than half of the theoretical value of 143.3 kJm^{-3} (18 MGOe) [1].

The Figure 4.2(b) provides the performance context for the Mn – Bi in terms of current dominant magnets present on the market: rare-earth-based hard permanent NdFeB magnets and soft ferrites (see [122]). Clearly, the overall figure of merit, the energy product (BH_{max}) is far below the values demonstrated by NdFeB, yet the increase of coercivity with the increasing temperature might carve a place for Mn – Bi in the high-temperature applications, since NdFeB starts dropping rapidly and requires heavy rare-earth dopants to operate at elevated temperatures.

4.1.2 Engineering versus physics approach

Most of the published studies on Mn-Bi-based magnets have focused on integral measurement techniques and on engineering aspects *e.g.* [96, 21, 105, 89, 130, 131, 51, 15]. Yet, the macroscopic magnetic properties arise, from spatial variations in the magnitude and orientation of the magnetization vector field $\mathbf{M}(\mathbf{r})$ on a mesoscopic length scale (a few nm up to the micron scale). Therefore, a deeper understanding of the correlations and long-wavelength magnetization fluctuations is of paramount importance both from the basic science point of view as well as from a materials science perspective aiming to optimize the properties of the material. These correlations and fluctuations were the main focus of [72]. The following section details on the main findings and furnishes more details.

Notably, the focus of [72] was on the first ever results of the unpolarized magnetic small-angle neutron scattering (SANS) experiments on cold-compacted isotropic Mn – Bi magnets. It is known [79] that the magnetic SANS is ideally suited to characterize the

magnetic structure and interactions on the mesoscopic length scale, providing insights on both variations of the magnitude and orientation of the magnetization $\mathbf{M}(\mathbf{r})$ in the bulk of the material.

Additionally, throughout measurements it became necessary to extend the conventional SANS into the very small-angle neutron scattering, as the real-space length scale of this material revealed to range from a few hundred nanometers up to the micron regime. The aim was to estimate the characteristic size of microstructural-defect-induced spin perturbations in the polycrystalline microstructure of Mn – Bi magnets and to provide first insights into this material via the SANS technique, not necessarily to advance the current Mn – Bi performance records. Moreover, the technical challenges throughout the whole process - from the sample manufacturing to its transport to the beamline to the temporal constraints on neutron measurements to post-beam sample activation and disposal were carefully assessed and are presented below.

4.2 Neutron samples and results

All Mn – Bi samples were synthesized using the conventional melting and milling, similar to [17, 94, 16]. Initial ingots were prepared by arc melting high-purity elements (99.8 % for Mn and 99.99 % for Bi) and annealed under Ar atmosphere for 24 h at 300 °C followed by quenching in water at room temperature. Subsequently, the resulting ingots were hand crushed under N_2 atmosphere into powder (with a particle size $< 60\,\mu$m) and ball milled for 2 h in hexane with a ball-to-powder weight ratio of 1:10 at 150 RPM, as detailed in [15]. The ball milled powder was washed in ethanol, magnetically separated, dried under N_2 atmosphere and cold compacted at a pressure of ~ 1.0 GPa into $10 \times 5 \times 1$ mm pellets. Magnetization isotherms were recorded using a vibrating sample magnetometer (Cryogenic, $\mu_0 H_{\max} = 14$ T, Figure 4.3).

The coercivity H_c of the samples varies between $0.47-0.56$ T for the compositions investigated, while the saturation magnetization M_s varies from about 33 $\mathrm{Am^2kg^{-1}}$ ($Mn_{55}Bi_{45}$) to 36 $\mathrm{Am^2kg^{-1}}$ ($Mn_{50}Bi_{50}$) to 34 $\mathrm{Am^2kg^{-1}}$ ($Mn_{45}Bi_{55}$). These values are far below the theoretical saturation magnetization of the low-temperature Mn – Bi phase (80 $\mathrm{Am^2kg^{-1}}$) and indicate a magnetic content of $\sim 40-45$ %[1].

[1] No single processing route alone has been reported to yield LTP-MnBi with purity> 90 wt % [110]. Moreover, the reader is reminded here that the emphasis of the current work was on the neutron analysis rather then on optimising the synthesis procedure.

A field larger than 1.8 T is sufficient to close the hysteresis loop and to reach the reversible part of the $M(H_0)$ curve. This observation is of relevance since in the neutron-data analysis the measurement at 2.2 T is used for subtraction to eliminate the nuclear scattering.

For more details on sample preparation and characterization using x-ray diffraction and scanning electron microscopy see [17].

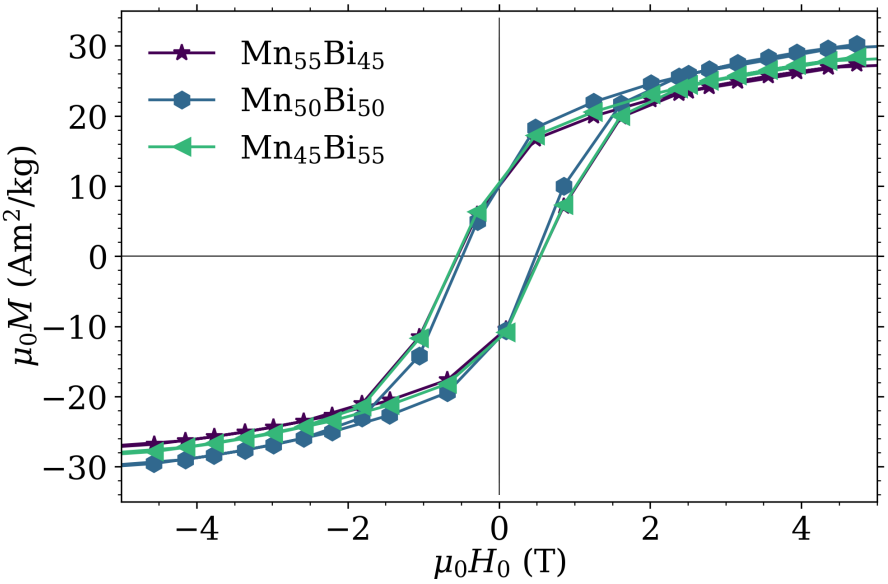

Fig. 4.3 Room-temperature hysteresis loops $M(H_0)$ of $Mn_{45}Bi_{55}$, $Mn_{50}Bi_{50}$ $Mn_{55}Bi_{45}$. (see inset). Taken from [72].

4.2.1 Preliminary SANS measurements on SANS-1

First, preliminary set of the neutron measurements was performed on the instrument SANS-1 at MLZ [91] were performed (see Figure 4.4 and Figure 4.5 for details). Three observations are of notice here:

1. The total scattering cross sections $d\Sigma/d\Omega$ (which include nuclear and magnetic scattering, see section 2.9 and section 2.10 for more details) appear to be isotropic for all the fields investigated (compare (a)−(d) Figure 4.4).

2. The magnetic SANS cross section $d\Sigma_M/d\Omega$ exhibits a slight elongation in the direction of the field (compare (e)−(h), which points to the existence of long-range spin perturbations on a scale of at least several tens and at most few hundreds of nanometers. Figure 4.4).

3. The 2π-azimuthal-averages of the data of Figure 4.4 is virtually featureless and exhibits only a very small field-dependence.

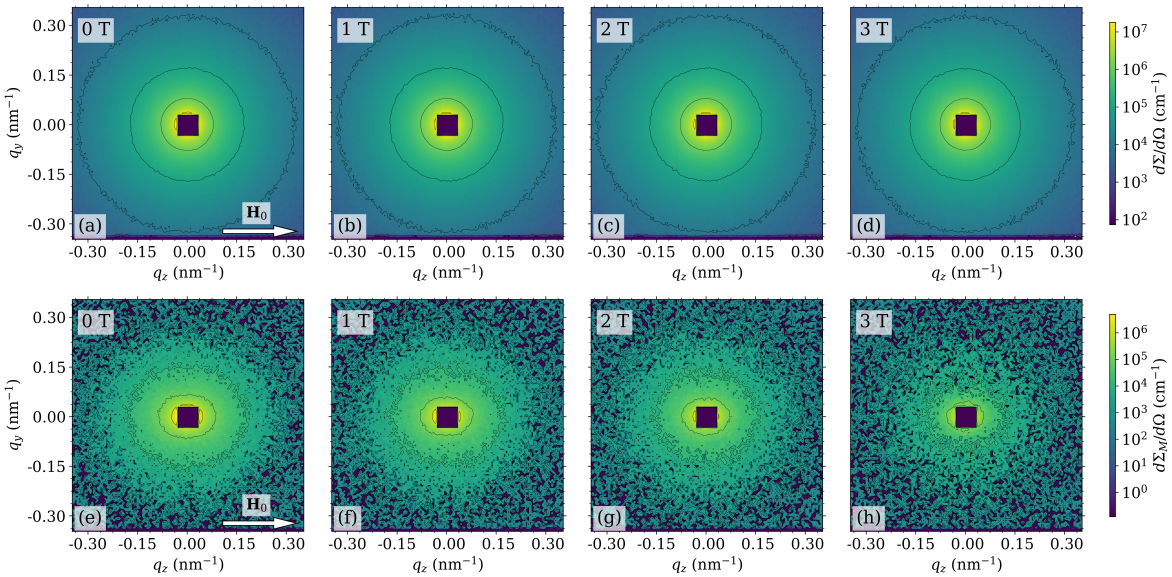

Fig. 4.4 Field dependence of the two-dimensional SANS cross section of $Mn_{55}Bi_{45}$ rare-earth-free permanent magnet ($\mathbf{H}_0 \perp \mathbf{k}_0$; logarithmic color scale; data measured at SANS-1, MLZ). (a)−(d) Total nuclear and magnetic $d\Sigma/d\Omega$. (e)−(h) Magnetic SANS cross section $d\Sigma_M/d\Omega$, obtained by subtracting the $d\Sigma/d\Omega$ at 4 T from the data at lower fields. Taken from the Supplementary Material of [72].

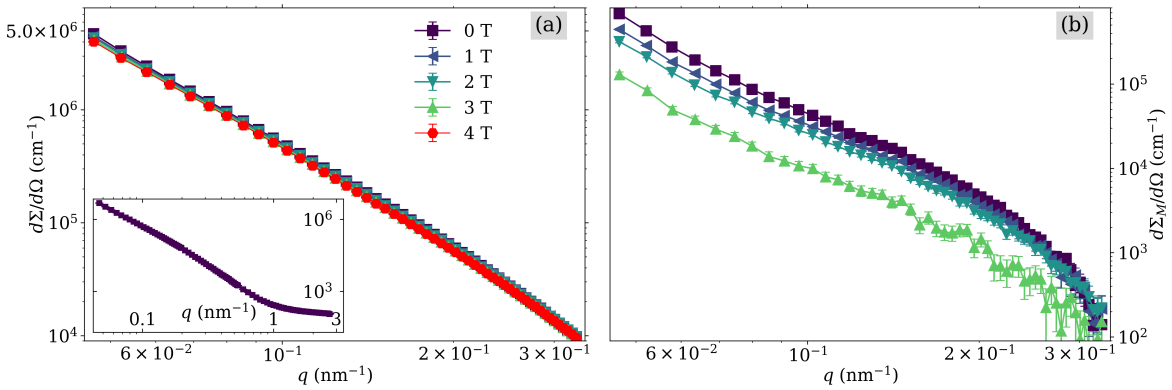

Fig. 4.5 2π-azimuthal-average of the data shown in Fig. 4.4 (log-log scale). (a) $d\Sigma/d\Omega$; (b) $d\Sigma_M/d\Omega$. Lines are guide to the eyes. Inset in (a) shows the full q-dependence of $d\Sigma/d\Omega$. Taken from the Supplementary Material of [72].

An essential experimental feature was the fact that even 1mm thick samples demonstrated quite low transmission values, potentially hinting at the multiple scattering effects. This

feature was not investigated further and the samples for the subsequent measurements were ground down to the the thickness of 0.1 mm. Another critical feature - the oxidation of Mn and the resulting reduction in the magnetic Mn – Bi phase content on a fairly quick time scale [50, 20] - necessitated in sample storage under Ar or N_2 atmosphere up to the measurement itself. No detailed study of the degradation dynamics was conducted, for a comparative XRD patterns and magnetisation curves the reader is referred to the Figure A.1 in the Appendix A which indicate the considerable decline in the magnetic phase content over a course of several weeks. Yet, since the measurement series on a single sample takes at most several days, SANS is the bulk technique and oxidation is most pronounced at the surface the effects of the sample degradation, even though undeniably there, were considered negligible further.

4.2.2 VSANS measurements on KWS-3

The lack of features in the 2π-azimuthal-averages of the data brought the attempt to extend the q-range to lower values to capture larger real-space correlations. This extension, together with a generalised Guinier-Porod model (see below) formed the basis of [72].

The bulk of the unpolarized SANS experiments presented in [72] were performed at the room temperature at the very small-angle neutron scattering instrument KWS-3 [103] at the Heinz Maier-Leibnitz Zentrum (MLZ), Garching, Germany. The external magnetic field $\mathbf{H}_0$ was applied perpendicular to the incident neutron beam ($\mathbf{H}_0 \perp \mathbf{k}_0$), and a mean wavelength of $\lambda = 12.8\,\text{Å}$ with a bandwidth of $\Delta\lambda/\lambda \cong 10\,\%$ (FWHM) was chosen. The covered momentum transfer ranges between about $0.002\,\text{nm}^{-1} \lesssim q \lesssim 0.2\,\text{nm}^{-1}$. The neutron experiments were performed by first applying a field of 2.2 T and then reducing the field. SANS data reduction (correction for background scattering, transmission, detector efficiency) was carried out using the QTI-SAS software package [102].

Figure 4.6 illustrates the standard neutron data analysis procedure, which is based on the subtraction of the total $d\Sigma/d\Omega$ at the highest field (Figure 4.6(a)) from data at lower fields (*e.g.*, Figure 4.6(b)). This eliminates the strong and presumably isotropic nuclear SANS contribution (compare Equation 2.49) and the discussion in section 2.9 and section 2.10) and provides access to the magnetic SANS cross section $d\Sigma_M/d\Omega$ (Figure 4.6(c)) [78, 92].

The 2D reduced and corrected $d\Sigma_M/d\Omega$ appear on Figure 4.7. The $d\Sigma_M/d\Omega$ are anisotropic, elongated along the direction *parallel* to the applied magnetic field $\mathbf{H}_0$, with increasing elongation at reducing field, in line with the expectation that higher $\mathbf{H}_0$ suppresses the spin missalignment. Comparing to the expression for $d\Sigma/d\Omega$ in the $\mathbf{H}_0 \perp \mathbf{k}_0$ geometry (Equation 2.49) this angular anisotropy can be related to the *transversal* Fourier component $|\widetilde{M}_y|^2 \cos^2\theta$ in $d\Sigma_M/d\Omega$. The feature is clearly observable for all Mn – Bi samples

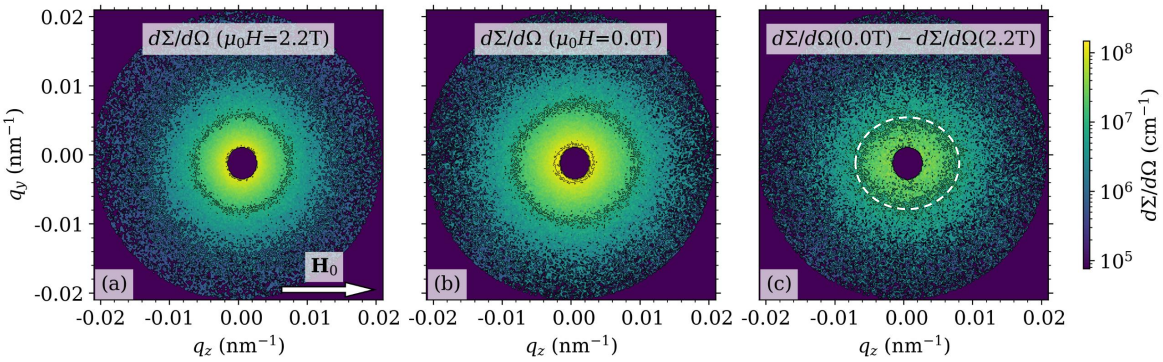

Fig. 4.6 Demonstration of the neutron data analysis procedure on corrected two-dimensional SANS cross sections of a $Mn_{55}Bi_{45}$ rare-earth-free permanent magnet ($\mathbf{H}_0 \perp \mathbf{k}_0$; logarithmic color scale). (a) Total (nuclear and magnetic) SANS cross section $d\Sigma/d\Omega$ at $\mu_0 H_0 = 2.2\,\mathrm{T}$ ($\mathbf{H}_0$ is horizontal in the plane, see inset). (b) $d\Sigma/d\Omega$ at remanence (0 T). (c) Magnetic (difference) SANS cross section $d\Sigma_M/d\Omega$ at remanence. The dashed white line emphasizes the slight elongation of $d\Sigma_M/d\Omega$ along $\mathbf{H}_0$. Taken from [72].

in the remanent state (Figure 4.7(c),(f),(i)), and suggests the presence of long-range spin-misalignment correlations on a real-space length scale of at least a few ten to a few hundreds of nanometers.

4.3 Generalized Guinier-Porod model

The magnetic SANS cross section $d\Sigma_M/d\Omega$ was analyzed in terms of the generalized Guinier-Porod model, developed by Hammouda [42]. The model describes the 2π-azimuthally-averaged scattering from both spherical and nonspherical objects. It is purely empirical and, essentially, decomposes the $I(q) = \frac{d\Sigma_M}{d\Omega}(q)$ curve into a Guinier region for $q \leq q_1$ and a Porod region for $q \geq q_1$. Both parts of the scattering curve are then joined by demanding the continuity of the Guinier and Porod laws (and of their derivatives) at q_1; more specifically [42]:

$$I(q) = \frac{G}{q^s} \exp\left(-\frac{q^2 R_G^2}{3-s}\right) \quad \text{for} \quad q \leq q_1, \tag{4.1}$$

$$I(q) = \frac{D}{q^n} \quad \text{for} \quad q \geq q_1, \tag{4.2}$$

where the scaling factors G and D, the Guinier radius R_G, the dimensionality factor s, and the Porod power-law exponent n are independent parameters. From the continuity of the Guinier

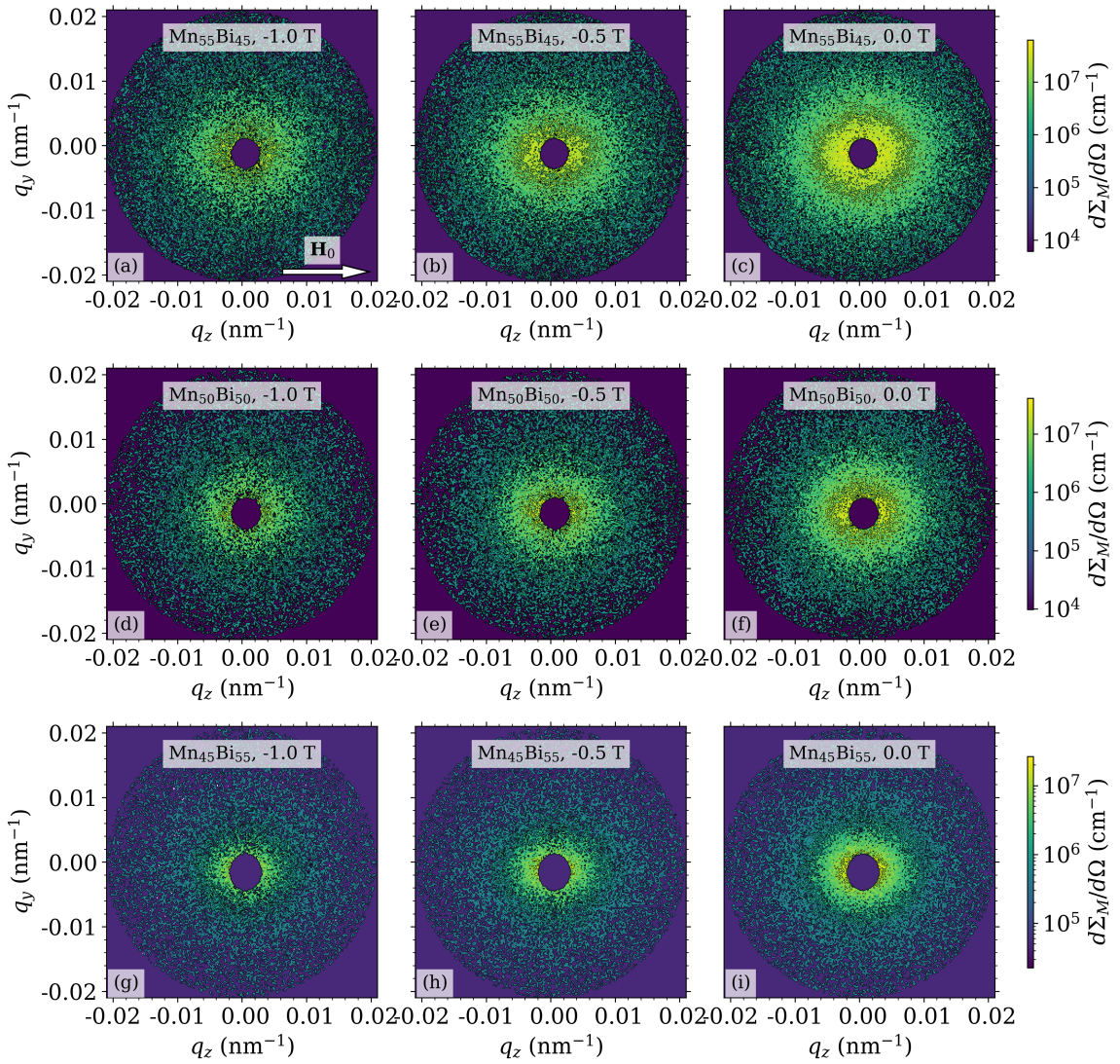

Fig. 4.7 Field dependence of the two-dimensional magnetic SANS cross section $d\Sigma_M/d\Omega$ of Mn – Bi rare-earth-free permanent magnets ($\mathbf{H}_0 \perp \mathbf{k}_0$; logarithmic color scale; data measured at KWS-3, MLZ). The $d\Sigma_M/d\Omega$ are obtained by subtracting the $d\Sigma/d\Omega$ at 2.2 T from the data at lower fields. Taken from the Supplementary Material of [72].

and Porod functions and their derivatives it follows that:

$$q_1 = \frac{1}{R_G}\left[\frac{(n-s)(3-s)}{2}\right]^{1/2}, \tag{4.3}$$

$$D = Gq_1^{n-s}\exp\left(-\frac{q_1^2 R_G^2}{3-s}\right), \tag{4.4}$$

where $n > s$ and $s < 3$ must be satisfied. Note that q_1 is not a fitting parameter, but an internally computed value (via Equation 4.3). For a dilute set of homogeneous *spherical* particles with sharp interfaces one expects $s = 0$, $n = 4$, and $R_G^2 = \frac{3}{5}R^2$, where R is the particle radius [42].

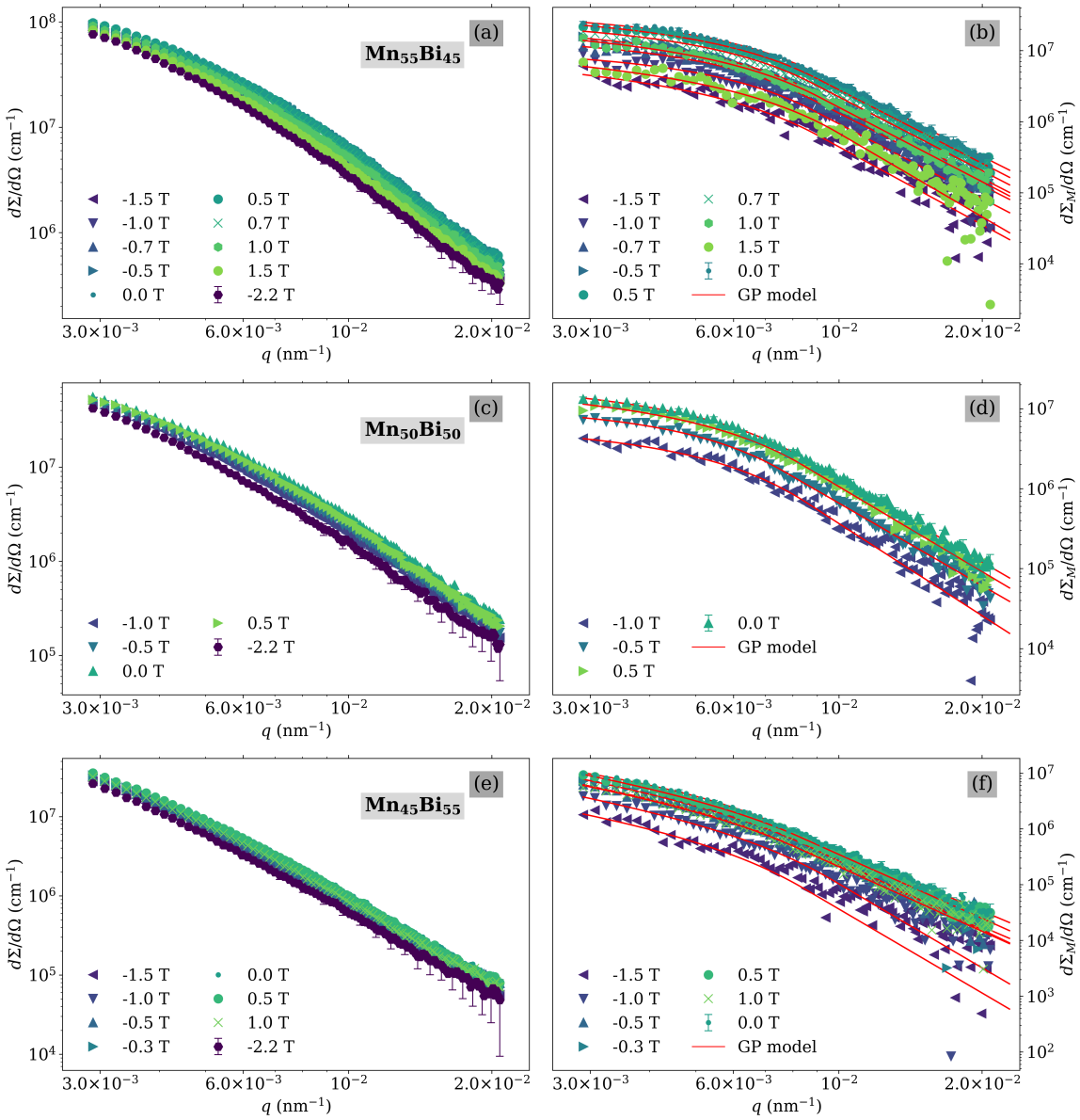

Fig. 4.8 Field dependence of the 2π-azimuthally-averaged SANS cross sections of Mn – Bi magnets ($\mathbf{H}_0 \perp \mathbf{k}_0$; log-log scale). (a),(c),(e) Total nuclear and magnetic $d\Sigma/d\Omega$. (b),(d),(f) Magnetic SANS cross section $d\Sigma_M/d\Omega$, obtained by subtracting the $d\Sigma/d\Omega$ at 2.2 T. Solid lines in (b),(d),(f): fit to the generalized Guinier-Porod model. Taken from the Supplementary Material of [72].

The two-dimensional magnetic SANS cross sections Figure 4.7 were azimuthally-averaged and the resulting data was fitted to the generalized Guinier-Porod (GP) model (Equation 4.1−Equation 4.4). The weighted nonlinear least-squares fits appear on Figure 4.8 and, for the remanent-state only, on Figure 4.9 (solid lines). In all cases, the GP model can very well describe the q-dependence of the $d\Sigma_M/d\Omega$. The obtained Guinier radii R_G are shown in Figure 4.10, while Table 4.1 lists the results for the remaining fit parameters (for the remanent state only).

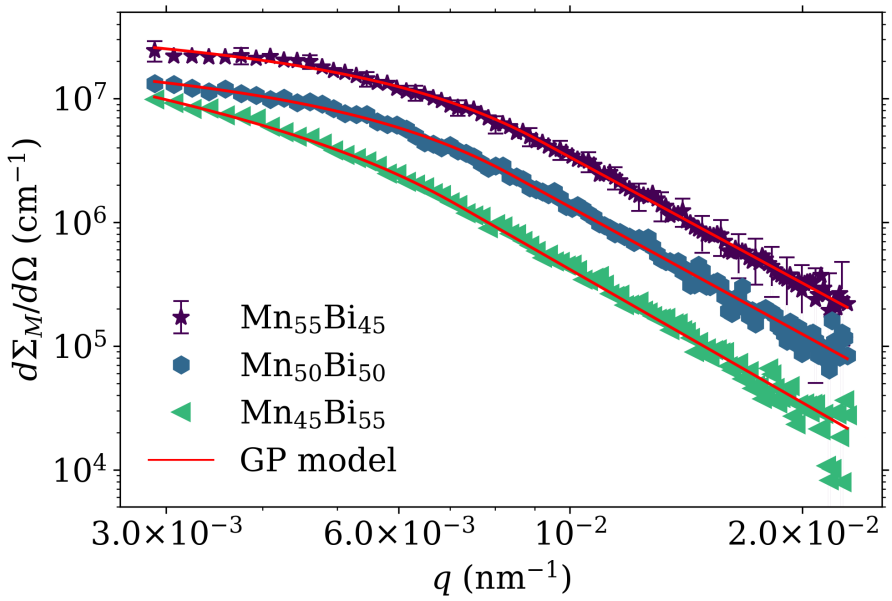

Fig. 4.9 2π-azimuthally-averaged $d\Sigma_M/d\Omega$ of Mn – Bi rare-earth-free permanent magnets in the remanent state ($\mathbf{H}_0 \perp \mathbf{k}_0$; log-log scale). Solid lines: fit to the generalized Guinier-Porod model [Eqs. (4.1)−(4.4)]. Error bars are selectively shown only for the $Mn_{55}Bi_{45}$ sample. Taken from [72].

	$Mn_{55}Bi_{45}$	$Mn_{50}Bi_{50}$	$Mn_{45}Bi_{55}$
R_G (nm)	224 ± 8	242 ± 12	218 ± 13
s	0.30 ± 0.07	0.35 ± 0.10	1.07 ± 0.09
n	3.38 ± 0.04	3.42 ± 0.04	3.58 ± 0.03

Table 4.1 Results of the fit analysis on Mn – Bi rare-earth-free permanent magnets using the generalized Guinier-Porod model [42] (remanent state).

The reader is reminded that the origin of magnetic SANS is due to spatial mesoscale variations in the magnitude and orientation of the magnetization (see the subsection 2.8.4 for the detailed discussion). Such magnetization fluctuations are (among others) caused by the

microstructural defects (*e.g.*, dislocations, interfaces, pores) via the magnetoelastic coupling of the magnetization to the strain field of the defect [62]. The range and the amplitude of defect-induced spin disorder can be suppressed by an applied field. The value of R_G is associated with the size of such perturbed, nonuniformly magnetized regions around defects.

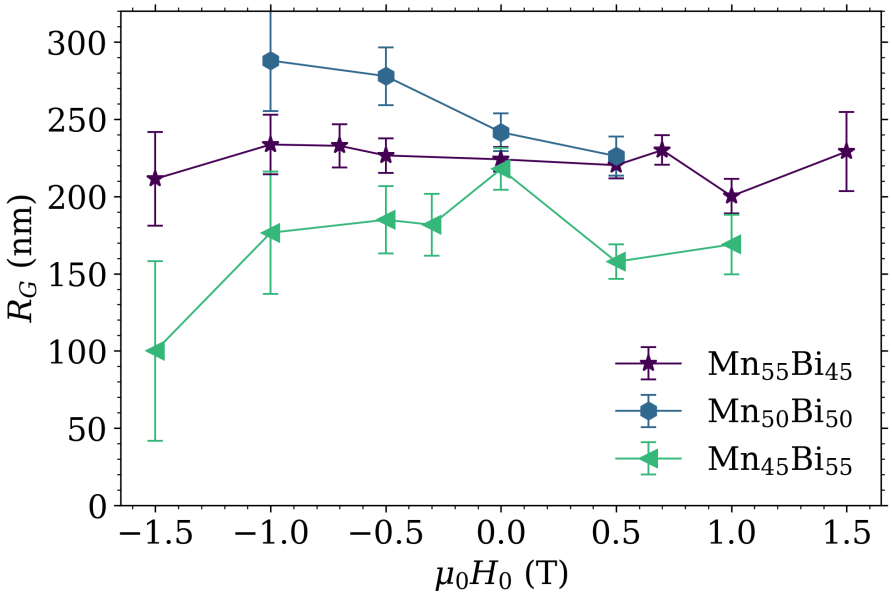

Fig. 4.10 Magnetic field dependence of the Guinier radii R_G resulting from the generalized Guinier-Porod model. Lines are a guide to the eyes. Taken from [72].

The Guinier radii in Figure 4.10 do not exhibit a systematic variation with the composition of the Mn – Bi samples. At remanence, their values range between $R_G \sim 220-240$ nm. While the R_G for the $Mn_{55}Bi_{45}$ sample are field independent within error bars, the $Mn_{45}Bi_{55}$ data exhibits a decrease of R_G with increasing field, from about 220 nm at remanence to ~ 100 nm at 1.5 T. Such a behavior is, again, in qualitative agreement with the suppression of spin-misalignment fluctuations around defects with increasing applied field [77]. On the other hand, the $Mn_{50}Bi_{50}$ sample exhibits an increase of R_G with the increasing field, from about 240 nm at remanence to ~ 285 nm at 1.0 T.

Yet, the considerable uncertainties in the R_G-values hinder any unambiguous conclusions about the field or composition dependence.

Finally, a cumulative plot of all fit parameters appears on the Figure 4.11. A particular oddity is the unusually low values of the Porod exponents n. In the context of particle scattering the reduction below the sharp-interface value of $n = 4$ could be interpreted as a roughening of the surfaces of the scattering objects [42]. However, for magnetic SANS, where continuous rather than sharp scattering-length density variations are at the origin of the scattering, asymptotic power-law exponents smaller than 4 have only been reported for

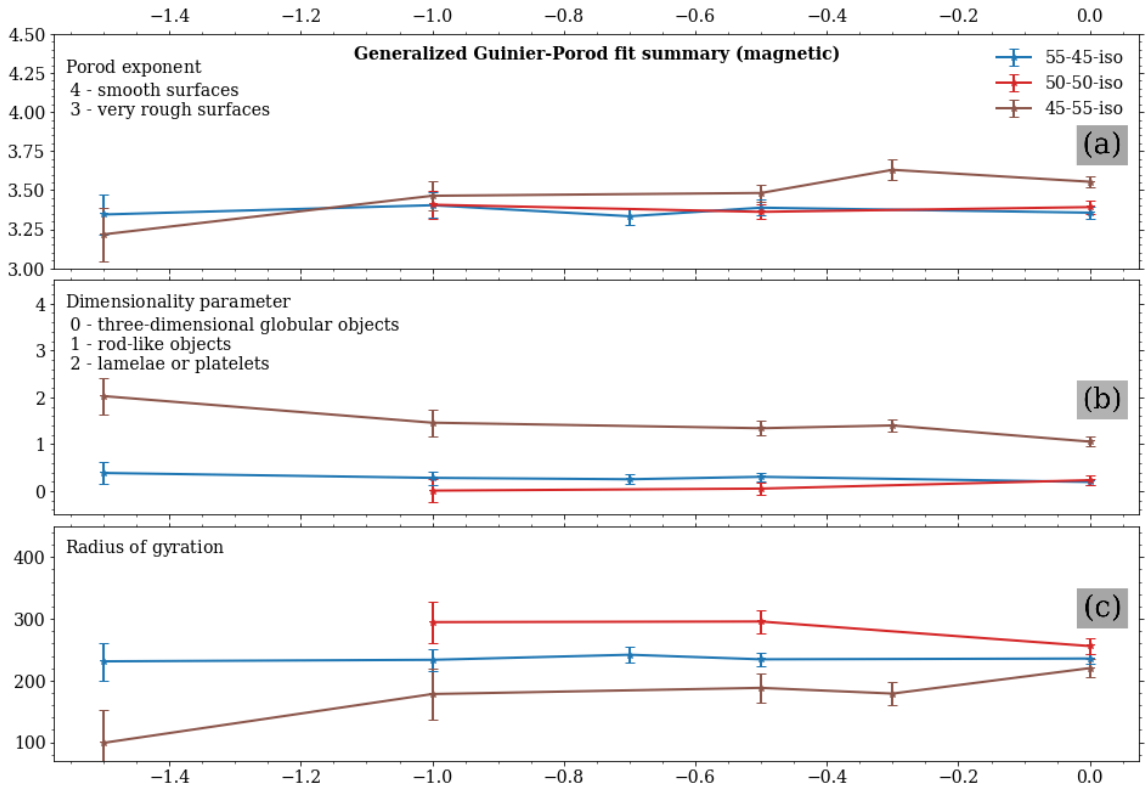

Fig. 4.11 Cumulative fit parameters of the data from Figure 4.8. (a) The Porod exponent related to the interface smoothness. (b) Dimensionality parameter describing the shape of the scatterers. (c) The radius of gyration related to the particle size.

amorphous magnets [76]. Similarly, exponentially correlated magnetization fluctuations would give rise to $n = 4$, corresponding to a Lorentzian-squared cross section. Thus, the systematic reduction of the Porod exponents n in Mn – Bi remains to be explored by future studies.

The s-parameter models nonspherical objects in the context of the generalized Guinier-Porod model [42]. For spherical particles (or domains in the magnetic case), s is expected to take on a value of $s = 0$. The $Mn_{55}Bi_{45}$ and $Mn_{50}Bi_{50}$ samples are close to this value for all the fields, whereas $Mn_{45}Bi_{55}$ exhibits $s = 1.07$ at remanence and this value seems to be increasing with the increasing field, which would indicate scattering due to elongated rod-like or even platelet-like objects. The latter observation is surprising in view of the fact that extended electron-microscopy investigations on similar samples, albeit on a different length scale, did not reveal the presence of shape-anisotropic particles [17] and, considering that some previous studies (*e.g.*, [94]) demonstrated enhanced coercivity over a wide range of temperatures with increasing Bi content, points an exciting direction for further analysis.

4.4 Distance distribution function

In addition to the generalized Guinier-Porod analysis, distance distribution function [5]:

$$p(r) = r^2 \int_0^\infty \frac{d\Sigma_M}{d\Omega}(q) j_0(qr) q^2 dq, \tag{4.5}$$

where $j_0(qr) = \sin(qr)/(qr)$ is the zeroth-order spherical Bessel function was calculated on the remanent state data. The $p(r)$ function corresponds to the distribution of real-space distances between volume elements inside the particle weighted by the excess scattering-length density distribution; see the reviews by Glatter [31] and by Svergun and Koch [120] for detailed discussions of the properties of $p(r)$ and for information on how to compute $p(r)$ by indirect Fourier transformation [5]. $p(r)$ provides the information on the characteristics (*e.g.*, size and shape) of the scattering objects [120, 28], and on the presence of interparticle correlations [65, 29]. This approach allows to model-independently asses the anisotropies and estimate characteristic sizes.

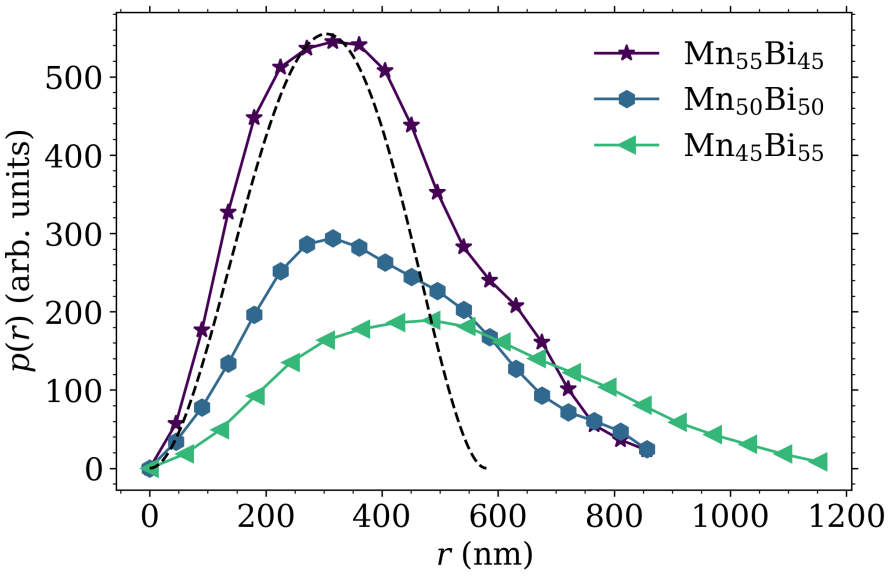

Fig. 4.12 Distance distribution functions $p(r)$ [Eq. (4.5)] of the remanent-state Mn – Bi data shown in Fig. 4.9. Dashed line: analytical $p(r) \propto r^2(1 - \frac{3r}{4R} + \frac{r^3}{16R^3})$ of a sphere of radius $R = 290\,\text{nm}$, corresponding to a Guinier radius of $R_G = \sqrt{\frac{3}{5}}R = 225\,\text{nm}$. Taken from [72].

The results for the $p(r)$, that appear on the Figure 4.12, are generally consistent with the Guinier-Porod model analysis both in terms of the characteristic lengths and the anisotropies of the scattering objects. Both $Mn_{55}Bi_{45}$ and $Mn_{50}Bi_{50}$ samples exhibit a $p(r)$ which is

typical for globular scatterers[2]. Though, small shoulder at the larger r points towards the presence of slightly anisotropic structures. By contrast, the $p(r)$ of the $Mn_{45}Bi_{55}$ sample clearly shows a broad maximum at $r \cong 470\,\text{nm}$ followed by a long tail at the larger r, suggesting that the scattering originates from shape-anisotropic elongated objects (compare Fig. 5 in the review by [120]). The broad maximum of $p(r)$ at the smaller distances of the $Mn_{45}Bi_{55}$ specimen corresponds to the shorter dimension of the structure, which, again, is in line with the behavior of the s-parameter obtained from the Guinier-Porod model.

4.5 Summary and outlook

The SANS measurements conducted in this work are, to the author's knowledge, the first experiment of this type on the Mn – Bi system, a promising rare-earth free permanent magnet candidate. The main objective of this work was to pave way for further studies and to provide the first insights rather then advance the state-of-the-art of Mn – Bi permanent magnet development for economically feasible applications.

The Guinier radius R_G, represents the characteristic size over which microstructural-defect-induced perturbations in the spin structure are transmitted by the exchange interaction into the surrounding crystal lattice. Thus, R_G is a measure for the size of inhomogeneously magnetized regions around lattice imperfections. This length scale is paramount for the understanding of the coercivity mechanism in Mn – Bi magnets – domain nucleation versus pinning – which is currently discussed in the literature [22, 94, 132]. For instance, the nucleation of a reverse domain in a grain usually starts at a defect site, where the magnetic anisotropy may be reduced relative to the bulk phase. Therefore, the presented neutron methodology (analysis of the magnetic SANS data using the generalized Guinier-Porod model and calculation of the distance distribution function) provides a means to systematically correlate the spin-misalignment length, which is a property of the defect, to the macroscopic parameters (e.g., coercivity, maximum energy product) of a permanent magnet. Moreover, previous studies (*e.g.*, [94]) indicate increased coercivity with shifting the alloy composition towards Bi, which was explained by differences in the grain-size distribution. The SANS analysis conducted here indicates that an increase of the Bi content results in increasingly elongated magnetic structures (4.12). Thus, a further controlled increase of Bi might be a valid approach to enhance the magnetic hardness of the compound via shape anisotropy. In

[2]Note that for these two samples the respective maximum of the $p(r)$ function, which is indicative of the "particle" radius R, roughly agrees with the R_G-value computed according to $R_G^2 = \frac{3}{5}R^2$ (assuming a spherical particle shape).

this respect, magnetic SANS permits the determination of the relevant figures of merit (R_G, s, n), which are otherwise not accessible by integral measurement techniques.

Chapter 5

Uniaxial Polarization Analysis

This chapter briefly summarizes the results of [73] and expands on the discussion presented herein.

5.1 Neutron polarization

Up to now, only unpolarized SANS cross sections were discussed. Yet, with the external field $\mathbf{H}_0$ one could define the polarization axis for both incident and scattered neutrons, for both parallel and perpendicular geometry. Notably, since in both cases $\mathbf{H}_0$ defines the e_z-direction, in the perpendicular ($\mathbf{k}_0 \perp \mathbf{H}_0$) geometry the polarization axis is *perpendicular* to the wave vector k_0 and in the parallel ($\mathbf{k}_0 \parallel \mathbf{H}_0$) geometry the polarization axis is *parallel* to the wave vector k_0.

In a classical picture, the polarization $\mathbf{P}$ of a neutron beam containing N spins can be defined as the average over the individual polarizations $\mathbf{P}_j$ of the neutrons as [112]:

$$\mathbf{P} = \frac{1}{N}\sum_{j=1}^{N}\mathbf{P}_j, \tag{5.1}$$

where $0 \leq |\mathbf{P}| \leq 1$. Practically, the beam is polarized with a certain efficiency (usually $\geq 90\%$) along the guide field direction (here and further the e_z-direction is assumed). In case the expectation values of the perpendicular polarization components vanish, *i.e.* $\langle P_x \rangle = \langle P_y \rangle = 0$, and that $\langle P_z \rangle = P$, the fractions:

$$p^+ = \frac{1}{2}(1+P) \quad \text{and} \quad p^- = \frac{1}{2}(1-P) \tag{5.2}$$

of neutrons in the spin-up (+) and spin-down (−) state can be introduced, with

$$p^+ + p^- = 1 \quad \text{and} \quad p^+ - p^- = P. \tag{5.3}$$

Obviously, for an unpolarized beam $p^+ = p^- = 0.5$ and $P = 0$, while $P = +1$ ($p^+ = 1$) or, respectively, $P = -1$ ($p^- = 1$) for a fully polarized beam.

Using a radio-frequency spin flipper (positioned after the polarizer and before the sample, refer to Figure 2.5 for a schematics), the initial polarization can be inverted. The efficiency of the spin flipper is $\varepsilon^{\pm}$ with $\varepsilon^+ = 0$ for flipper off and $\varepsilon^- = \varepsilon \cong 1$ for the flipper on.

With an analyzer behind the sample, selecting only neutrons with spins either parallel or antiparallel to the initial polarization[1], four scattering cross sections can be distinguished [8, 90, 112], two of which conserve the neutron-spin direction and two of which reverse the neutron spin, each a result of a separate scattering process:

- a neutron in a spin-up (+) state remains in the spin-up (+) state after the scattering process, commonly denoted with (++) superscript index in the cross section expression
- a neutron in a spin-down (−) state remains in the spin-down (−) state after the scattering process, commonly denoted with (−−) superscript index in the cross section expression
- a neutron in a spin-up (+) state switches (or flips) into the spin-down (−) state after the scattering process, commonly denoted with (+−) superscript index in the cross section expression
- a neutron in a spin-up (−) state switches (or flips) into the spin-up (+) state after the scattering process, commonly denoted with (−+) superscript index in the cross section expression.

This results in 4 partial SANS cross sections, the first two [(++) and (−−)] are known as the non-spin-flip cross sections and could be written in terms of the Cartesian components of the Halpern–Johnson vector $\widetilde{\mathbf{Q}}$ as (compare Equation 2.48 and subsection 2.5.1):

$$\frac{d\Sigma^{++}}{d\Omega} = \frac{8\pi^3}{V} b_{\mathrm{H}}^2 \left[b_{\mathrm{H}}^{-2} |\widetilde{N}|^2 + b_{\mathrm{H}}^{-1} (\widetilde{N}\widetilde{Q}_z^* + \widetilde{N}^* \widetilde{Q}_z) + |\widetilde{Q}_z|^2 \right], \tag{5.4a}$$

$$\frac{d\Sigma^{--}}{d\Omega} = \frac{8\pi^3}{V} b_{\mathrm{H}}^2 \left[b_{\mathrm{H}}^{-2} |\widetilde{N}|^2 - b_{\mathrm{H}}^{-1} (\widetilde{N}\widetilde{Q}_z^* + \widetilde{N}^* \widetilde{Q}_z) + |\widetilde{Q}_z|^2 \right]. \tag{5.4b}$$

[1] Or an additional flipper before the analyzer with the fixed direction

The latter two [$(+-)$ and $(-+)$] are the so-called spin-flip cross sections:

$$\frac{d\Sigma^{+-}}{d\Omega} = \frac{8\pi^3}{V} b_{\mathrm{H}}^2 \left[|\widetilde{Q}_x|^2 + |\widetilde{Q}_y|^2 - i\mathbf{e}_z \cdot (\widetilde{\mathbf{Q}} \times \widetilde{\mathbf{Q}}^*) \right], \tag{5.5a}$$

$$\frac{d\Sigma^{-+}}{d\Omega} = \frac{8\pi^3}{V} b_{\mathrm{H}}^2 \left[|\widetilde{Q}_x|^2 + |\widetilde{Q}_y|^2 + i\mathbf{e}_z \cdot (\widetilde{\mathbf{Q}} \times \widetilde{\mathbf{Q}}^*) \right]. \tag{5.5b}$$

As before, V denotes the scattering volume, $\widetilde{N}(\mathbf{q})$ denotes the Fourier transform of the nuclear scattering-length density $N(\mathbf{r})$, and $b_{\mathrm{H}} = 2.91 \times 10^8\,\mathrm{A^{-1}m^{-1}}$ is a constant relating the atomic magnetic moment μ_{a} to the atomic magnetic scattering length b_{m}.

Inspection of Equations 5.4a - 5.5b reveals that the transversal components $\widetilde{Q}_x$ and $\widetilde{Q}_y$ give rise to the spin-flip scattering, while the longitudinal component $\widetilde{Q}_z$ results in the non-spin-flip scattering.

Considering the cartesian components of the HJ-vector in both geometries (Equation 2.33 and Equation 2.34 respectively):

$$\widetilde{\mathbf{Q}}_\perp = \left\{ \begin{array}{c} -\widetilde{M}_x \\ -\widetilde{M}_y \cos^2\theta + \widetilde{M}_z \sin\theta\cos\theta \\ \widetilde{M}_y \sin\theta\cos\theta - \widetilde{M}_z \sin^2\theta \end{array} \right\},$$

$$\widetilde{\mathbf{Q}}_\parallel = \left\{ \begin{array}{c} -\widetilde{M}_x \sin^2\theta + \widetilde{M}_y \sin\theta\cos\theta \\ \widetilde{M}_x \sin\theta\cos\theta - \widetilde{M}_y \cos^2\theta \\ -\widetilde{M}_z \end{array} \right\},$$

one observes that if the scattering vector is along the neutron polarization (*i.e.*, $\theta = 0^\circ$), the $\widetilde{\mathbf{Q}}_\perp$ reduces to (compare Equation 2.33):

$$\widetilde{\mathbf{Q}}_\perp^{\theta=0^\circ} = \left\{ \begin{array}{c} -\widetilde{M}_x \\ -\widetilde{M}_y \\ 0 \end{array} \right\}, \tag{5.6}$$

in the perpendicular ($\mathbf{k}_0 \perp \mathbf{H}_0$) geometry and, respectively, $(\widetilde{N}\widetilde{Q}_z^* + \widetilde{N}^*\widetilde{Q}_z)$ terms in Equation 5.4a and Equation 5.4b vanish, so that nuclear coherent and magnetic scattering are fully separated.

Thus, in the case of the parallel geometry ($\mathbf{k}_0 \parallel \mathbf{H}_0$), spin-flip scattering probes *only* the transversal magnetization Fourier components $\widetilde{M}_{x,y}$, whereas the longitudinal scattering is entirely contained in the non-spin-flip channels. In contrast, in the perpendicular geometry

($\mathbf{k}_0 \perp \mathbf{H}_0$), the longitudinal and transversal magnetization Fourier components are separated only for certain directions on the detector.

5.2 Scattered beam polarization

The total SANS cross section $d\Sigma/d\Omega$ can then be expressed in terms of the initial spin populations $p^{\pm}$ as [8, 90, 112]:

$$\frac{d\Sigma}{d\Omega} = p^{+}\frac{d\Sigma^{++}}{d\Omega} + p^{+}\frac{d\Sigma^{+-}}{d\Omega} + p^{-}\frac{d\Sigma^{--}}{d\Omega} + p^{-}\frac{d\Sigma^{-+}}{d\Omega}. \tag{5.7}$$

Inserting the expressions for p^{+} and p^{-} (Equation 5.2 and Equation 5.3) and for the partial SANS cross sections $d\Sigma^{\pm\pm}/d\Omega$ and $d\Sigma^{\pm\mp}/d\Omega$ (Equations 5.4a – 5.5b), $d\Sigma/d\Omega$ evaluates to:

$$\frac{d\Sigma}{d\Omega} = \frac{8\pi^3}{V} b_{\mathrm{H}}^2 \left[b_{\mathrm{H}}^{-2} |\widetilde{N}|^2 + |\widetilde{\mathbf{Q}}|^2 + \mathbf{P} \cdot b_{\mathrm{H}}^{-1} (\widetilde{N}\widetilde{\mathbf{Q}}^* + \widetilde{N}^*\widetilde{\mathbf{Q}}) - i\mathbf{P} \cdot (\widetilde{\mathbf{Q}} \times \widetilde{\mathbf{Q}}^*) \right]. \tag{5.8}$$

Distinguishing two cases with respect to the initial neutron polarization orientations with respect to the e_z-direction:

- $\mathbf{P} = \{0, 0, P_z = P\}$ parallel orientation or P^{+}
- $\mathbf{P} = \{0, 0, P_z = -P\}$ anti-parallel orientation or P^{-}

Equation 5.8 can be rewritten as:

$$\frac{d\Sigma^{\pm}}{d\Omega} = \frac{8\pi^3}{V} b_{\mathrm{H}}^2 \left[b_{\mathrm{H}}^{-2} |\widetilde{N}|^2 + |\widetilde{\mathbf{Q}}|^2 \pm P b_{\mathrm{H}}^{-1} (\widetilde{N}\widetilde{Q}_z^* + \widetilde{N}^*\widetilde{Q}_z) \mp iP\mathbf{e}_z \cdot (\widetilde{\mathbf{Q}} \times \widetilde{\mathbf{Q}}^*) \right]. \tag{5.9}$$

Conceptually, the the polarization P_{f} of the scattered beam along the direction of the incident neutron polarization P counts only the neutrons in a given polarization state in the scattered beam, *i.e.*, explicitly:

- the neutrons that originally were in the $(+)$ state and that scattered in the non-spin-flip scattering into the $(+)$ state (symbolically corresponding to $p^{+}\frac{d\Sigma^{++}}{d\Omega}$)
- the neutrons that originally were in the $(-)$ state and yet scattered via the spin-flip scattering into the $(+)$ state (symbolically corresponding to $p^{-}\frac{d\Sigma^{-+}}{d\Omega}$ term)

as a positive contribution and subtracting

- the neutrons that originally were in the $(-)$ state and that scattered in the non-spin-flip scattering into the $(-)$ state ($p^- \frac{d\Sigma^{--}}{d\Omega}$ symbolically)
- the neutrons that originally were in the $(+)$ state and yet scattered via the spin-flip scattering into the $(-)$ state ($p^+ \frac{d\Sigma^{+-}}{d\Omega}$ symbolically).

Thus, omitting the nuclear-spin-dependent scattering[2], the polarization P_f of the scattered beam along the direction of the incident neutron polarization P is obtained from the following expression [8, 90, 112]:

$$\begin{aligned} P_\mathrm{f}\frac{d\Sigma}{d\Omega} &= p^+\frac{d\Sigma^{++}}{d\Omega} + p^-\frac{d\Sigma^{-+}}{d\Omega} - p^-\frac{d\Sigma^{--}}{d\Omega} - p^+\frac{d\Sigma^{+-}}{d\Omega} \\ &= \frac{8\pi^3}{V} b_\mathrm{H}^2 P \left[b_\mathrm{H}^{-2}|\widetilde{N}|^2 + |\widetilde{Q}_z|^2 - |\widetilde{Q}_x|^2 - |\widetilde{Q}_y|^2 \right] \\ &+ \frac{8\pi^3}{V} b_\mathrm{H}^2 \left[b_\mathrm{H}^{-1}(\widetilde{N}\widetilde{Q}_z^* + \widetilde{N}^*\widetilde{Q}_z) + i\mathbf{e}_z \cdot (\widetilde{\mathbf{Q}} \times \widetilde{\mathbf{Q}}^*) \right]. \end{aligned} \tag{5.10}$$

The first four ($\frac{8\pi^3}{V} b_\mathrm{H}^2 P$) terms on the right-hand side of the Equation 5.10 demonstrate that the nuclear coherent scattering[3] and the scattering due to the longitudinal component $\widetilde{Q}_z$ of the magnetic scattering vector $\widetilde{\mathbf{Q}}$ *do not* reverse the initial polarization, *i.e.* maintain the sign of P whereas the two transversal components $\widetilde{Q}_x$ and $\widetilde{Q}_y$ *give rise* to spin-flip scattering, *i.e.* switch the sign of P.

The last two ($\frac{8\pi^3}{V} b_\mathrm{H}^2$) terms in the Equation 5.10 create polarization: these are the nuclear-magnetic interference terms ($\widetilde{N}\widetilde{Q}_z^* + \widetilde{N}^*\widetilde{Q}_z$), which are commonly used to polarize beams, and the chiral term $i\mathbf{e}_z \cdot (\widetilde{\mathbf{Q}} \times \widetilde{\mathbf{Q}}^*)$, which manifests in the inelastic scattering (*e.g.*, dynamic chirality) [69, 34], in elastic scattering on spiral structures and weak ferromagnets (*e.g.*, canted antiferromagnets) [123], or in the presence of the Dzyaloshinskii–Moriya interaction in microstructural-defect-rich magnets [85, 108].

From the Equation 5.10 it follows that the polarization $P_\mathrm{f}(\mathbf{q})$ of the scattered neutron beam at momentum-transfer vector $\mathbf{q}$ can be expressed as [70, 8, 10]:

$$P_\mathrm{f} = \frac{p^+\frac{d\Sigma^{++}}{d\Omega} + p^-\frac{d\Sigma^{-+}}{d\Omega} - p^-\frac{d\Sigma^{--}}{d\Omega} - p^+\frac{d\Sigma^{+-}}{d\Omega}}{p^+\frac{d\Sigma^{++}}{d\Omega} + p^+\frac{d\Sigma^{+-}}{d\Omega} + p^-\frac{d\Sigma^{--}}{d\Omega} + p^-\frac{d\Sigma^{-+}}{d\Omega}}, \tag{5.11}$$

[2] In the general expression for the polarization of the scattered neutrons, a term $i\mathbf{P} \times (\widetilde{N}\widetilde{\mathbf{Q}}^* - \widetilde{N}^*\widetilde{\mathbf{Q}})$ appears [112], which is ignored in equation (5.10). This term rotates the polarization perpendicular to the initial polarization and cannot be observed in the uniaxial setup. In linear neutron polarimetry it is not possible to distinguish between a rotation of the polarization vector and a change of its length [90, 69].

[3] To be more precise, the nuclear coherent scattering, the isotopic disorder scattering, and $1/3$ of the nuclear-spin-dependent scattering.

which for $p^+ = 1$ ($p^- = 0$) and $p^- = 1$ ($p^+ = 0$) reduces to, respectively:

$$P_{\mathrm{f}}^{+} = \frac{\frac{d\Sigma^{++}}{d\Omega} - \frac{d\Sigma^{+-}}{d\Omega}}{\frac{d\Sigma^{++}}{d\Omega} + \frac{d\Sigma^{+-}}{d\Omega}}, \tag{5.12a}$$

$$P_{\mathrm{f}}^{-} = \frac{\frac{d\Sigma^{-+}}{d\Omega} - \frac{d\Sigma^{--}}{d\Omega}}{\frac{d\Sigma^{--}}{d\Omega} + \frac{d\Sigma^{-+}}{d\Omega}}. \tag{5.12b}$$

Alternatively, recalling that the half-polarized SANS cross sections $d\Sigma^{+}/d\Omega$ and $d\Sigma^{-}/d\Omega$ which are used to denote the experiments with a polarized incident beam only, and no spin analysis of the scattered neutrons (also known as SANSPOL technique [78, 92]) combine non-spin-flip and spin-flip scattering contributions, according to ($p^{\pm} = 1$):

$$\frac{d\Sigma^{+}}{d\Omega} = \frac{d\Sigma^{++}}{d\Omega} + \frac{d\Sigma^{+-}}{d\Omega}, \tag{5.13a}$$

$$\frac{d\Sigma^{-}}{d\Omega} = \frac{d\Sigma^{--}}{d\Omega} + \frac{d\Sigma^{-+}}{d\Omega}, \tag{5.13b}$$

Equation 5.12a and Equation 5.12b could be re-written as:

$$P_{\mathrm{f}}^{+} = 1 - 2\frac{\frac{d\Sigma^{+-}}{d\Omega}}{\frac{d\Sigma^{+}}{d\Omega}}, \tag{5.14a}$$

$$P_{\mathrm{f}}^{-} = -\left(1 - 2\frac{\frac{d\Sigma^{-+}}{d\Omega}}{\frac{d\Sigma^{-}}{d\Omega}}\right). \tag{5.14b}$$

Note that the minus sign in front of the round brackets in equation (5.14b) is simply a manifestation of the positive e_z direction and thus it is dropped in the further discussion.

5.3 Polarized SANS cross sections

This section is included for completeness sake only, it expands Equations 5.4a – 5.5b using the HJ-vector (see Equation 2.33 for $\mathbf{k}_0 \perp \mathbf{H}_0$ and Equation 2.34 for $\mathbf{k}_0 \parallel \mathbf{H}_0$) and substitutes micromagnetic expressions of the Fourier components $\widetilde{M}_{x,y,z}(\mathbf{q})$ of the magnetization (see subsection 2.8.3 for details, Equation 2.43/Equation 2.44 for $\mathbf{k}_0 \perp \mathbf{H}_0$ and Equation 2.45/Equation 2.46 for $\mathbf{k}_0 \parallel \mathbf{H}_0$ respectively).

The superscripts $(++)$ and $(--)$ denote the non-spin-flip scattering cross sections whereas $(+-)$ and $(-+)$ mark the two spin-flip scattering cross sections. The subscripts $\perp$

and $\|$ refer to the respective perpendicular and parallel scattering geometries.

$$\frac{d\Sigma_{\perp}^{\pm\pm}}{d\Omega} = \frac{8\pi^3}{V} b_{\mathrm{H}}^2 \Big(b_{\mathrm{H}}^{-2} |\widetilde{N}|^2 + |\widetilde{M}_y|^2 \sin^2\theta \cos^2\theta + |\widetilde{M}_z|^2 \sin^4\theta - CT_{yz} \sin^3\theta \cos\theta \mp b_{\mathrm{H}}^{-1} CT_{\widetilde{N}\widetilde{M}_z} \sin^2\theta \pm b_{\mathrm{H}}^{-1} CT_{\widetilde{N}\widetilde{M}_y} \sin\theta\cos\theta \Big), \tag{5.15}$$

$$\frac{d\Sigma_{\|}^{\pm\pm}}{d\Omega} = \frac{8\pi^3}{V} b_{\mathrm{H}}^2 \Big(b_{\mathrm{H}}^{-2} |\widetilde{N}|^2 + |\widetilde{M}_z|^2 \mp b_{\mathrm{H}}^{-1} CT_{\widetilde{N}\widetilde{M}_z} \Big), \tag{5.16}$$

$$\frac{d\Sigma_{\perp}^{\pm\mp}}{d\Omega} = \frac{8\pi^3}{V} b_{\mathrm{H}}^2 \Big(|\widetilde{M}_x|^2 + |\widetilde{M}_y|^2 \cos^4\theta + |\widetilde{M}_z|^2 \sin^2\theta \cos^2\theta - CT_{yz} \sin\theta \cos^3\theta \mp i\chi \Big) \tag{5.17}$$

$$\frac{d\Sigma_{\|}^{\pm\mp}}{d\Omega} = \frac{8\pi^3}{V} b_{\mathrm{H}}^2 \Big(|\widetilde{M}_x|^2 \sin^2\theta + |\widetilde{M}_y|^2 \cos^2\theta - CT_{xy} \sin\theta\cos\theta \Big), \tag{5.18}$$

where the chiral function $\chi(\mathbf{q})$ is given by:

$$\chi = \Big(\widetilde{M}_x \widetilde{M}_y^* - \widetilde{M}_x^* \widetilde{M}_y \Big) \cos^2\theta - \Big(\widetilde{M}_x \widetilde{M}_z^* - \widetilde{M}_x^* \widetilde{M}_z \Big) \sin\theta\cos\theta. \tag{5.19}$$

The two SANSPOL cross sections $\frac{d\Sigma^+}{d\Omega}$ (Equation 5.13a) and $\frac{d\Sigma^-}{d\Omega}$ (Equation 5.13b) are:

$$\frac{d\Sigma_{\perp}^{\pm}}{d\Omega} = \frac{8\pi^3}{V} b_{\mathrm{H}}^2 \Big(b_{\mathrm{H}}^{-2} |\widetilde{N}|^2 + |\widetilde{M}_x|^2 + |\widetilde{M}_y|^2 \cos^2\theta + |\widetilde{M}_z|^2 \sin^2\theta - CT_{yz} \sin\theta\cos\theta \mp b_{\mathrm{H}}^{-1} CT_{\widetilde{N}\widetilde{M}_z} \sin^2\theta \pm b_{\mathrm{H}}^{-1} CT_{\widetilde{N}\widetilde{M}_y} \sin\theta\cos\theta \mp i\chi \Big), \tag{5.20}$$

$$\frac{d\Sigma^{\pm}_{\parallel}}{d\Omega} = \frac{8\pi^3}{V} b_{\mathrm{H}}^2 \Big(b_{\mathrm{H}}^{-2} |\widetilde{N}|^2 + |\widetilde{M}_x|^2 \sin^2\theta + |\widetilde{M}_y|^2 \cos^2\theta + |\widetilde{M}_z|^2 - CT_{xy} \sin\theta\cos\theta \mp b_{\mathrm{H}}^{-1} CT_{\widetilde{N}\widetilde{M}_z} \Big) . \tag{5.21}$$

Notably, for $\mathbf{k}_0 \parallel \mathbf{H}_0$ geometry $\chi(\mathbf{q}) = 0$.

The magnetic-magnetic and nuclear-magnetic cross terms were abbreviated as:

$$CT_{yz} = \widetilde{M}_y \widetilde{M}_z^* + \widetilde{M}_y^* \widetilde{M}_z, \tag{5.22a}$$

$$CT_{xy} = \widetilde{M}_x \widetilde{M}_y^* + \widetilde{M}_x^* \widetilde{M}_y, \tag{5.22b}$$

$$CT_{\widetilde{N}\widetilde{M}_z} = \widetilde{N} \widetilde{M}_z^* + \widetilde{N}^* \widetilde{M}_z, \tag{5.22c}$$

$$CT_{\widetilde{N}\widetilde{M}_y} = \widetilde{N} \widetilde{M}_y^* + \widetilde{N}^* \widetilde{M}_y. \tag{5.22d}$$

Additionally, as mentioned in passing before, in the actual experiments the neutron optics is not perfect and polarization corrections become necessary. The incident beam polarization efficiency is denoted by $P = I^+/(I^+ + I^-)$, where $I^{\pm}$ are, respectively, the number of neutrons with spins aligned antiparallel and parallel with respect to $\mathbf{H}_0$. The efficiency of the spin flipper is $\varepsilon^{\pm}$ with $\varepsilon^- = \varepsilon \cong 1$ for the flipper activated and $\varepsilon^+ = 0$ for flipper off.

Essentially, the half-polarized SANSPOL cross sections $d\Sigma^+/d\Omega$ and $d\Sigma^-/d\Omega$ can be measured directly and corrected for the nonideal optics, provided that the parameters P and ε are known from reference measurements. For POLARIS, it is necessary to measure all four partial cross sections ($d\Sigma^{++}/d\Omega$, $d\Sigma^{--}/d\Omega$, $d\Sigma^{+-}/d\Omega$, and $d\Sigma^{-+}/d\Omega$) to correct for the spin leakage between the different channels [127]. Such corrections can *e.g.* be accomplished by means of the *BerSANS* [56, 57], *Pol-Corr* [63], and *GRASP* [23] software tools, assuming the existence of reference measurements and provided the instrument parameters.

Finally, for many polycrystalline bulk ferromagnets $d\Sigma^{+-}/d\Omega = d\Sigma^{-+}/d\Omega$ [46]. However, in the theoretical treatment presented here, the polarization dependence of the SANSPOL and spin-flip cross sections is explicitly accounted for via the chiral function $\chi(\mathbf{q})$. This is extremely relevant for systems where *e.g.*, the inversion symmetry is broken and the DMI is non-neglectable [85, 108].

For a quantitative analysis of $P_{\mathrm{f}}^{\pm}$, a theoretical model for the magnetization Fourier components $\widetilde{M}_{x,y,z}(\mathbf{q})$ and for $\widetilde{N}(\mathbf{q})$ is required. This is the focus of the subsequent section.

5.4 Models and assumptions

Respectively, with the explicit expressions for polarized SANS cross sections, Equation 5.14a and Equation 5.14b could be re-written in terms of the magnitude and orientation of the scattering vector $\mathbf{q}$, the applied magnetic field $\mathbf{H}_0$, the magnetic-interaction parameters (A, D, M_0, ΔM, H_p), microstructural quantities (particle-size distribution, crystallograpic texture, etc.) and the Fourier components of the nuclear scattering function $\widetilde{N}$, the longitudinal magnetic and the magnetic anisotropy fields $\widetilde{M}_z$ and $\widetilde{H}$ respectively.

The latter depend of a particular models chosen and in the initial treatment $\widetilde{N}^2$, $\widetilde{M}_z^2$, and $\widetilde{H}_\mathrm{p}^2$ are all assumed to be isotropic (*i.e.* θ-independent), as is appropriate for polycrystalline texture-free bulk ferromagnets. Secondly, $\widetilde{M}_z^2$ and $\widetilde{H}_\mathrm{p}^2$ are represented by Lorentzian-squared functions, *i.e.*

$$\widetilde{M}_z^2(q\xi_\mathrm{M}) = \frac{A_\mathrm{M}^2 \xi_\mathrm{M}^6}{\left(1+q^2\xi_\mathrm{M}^2\right)^2}, \tag{5.23}$$

$$\widetilde{H}_\mathrm{p}^2(q\xi_\mathrm{H}) = \frac{A_\mathrm{H}^2 \xi_\mathrm{H}^6}{\left(1+q^2\xi_\mathrm{H}^2\right)^2}, \tag{5.24}$$

where the amplitudes A_M^2 and A_H^2 (both in units of $\mathrm{A^2nm^{-2}}$) are related to the mean-square magnetization fluctuation and anisotropy-field variation respectively. The characteristic structure sizes (ξ_M for $\widetilde{M}_z^2$ and ξ_H for $\widetilde{H}_\mathrm{p}^2$) are generally different and are related, respectively, to the spatial extent of regions with uniform saturation magnetization (ξ_M) and magnetic anisotropy field (ξ_H).

A system with $\xi_\mathrm{M} = \xi_\mathrm{H}$ is *e.g.*, a collection of homogeneous and defect-free magnetic nanoparticles in a magnetic and homogeneous matrix. Alternatively, an example of a $\xi_\mathrm{H} < \xi_\mathrm{M}$ system is the introduction of atomically-sharp grain boundaries: the direction of the magnetic anisotropy field will change due to the change of crystallographic directions at the intraparticle interfaces, but the value of M_s remains the same.

In [80] it was shown that, assuming $\xi_\mathrm{H} = \xi_\mathrm{M}$ and using the sphere form factor for both $\widetilde{M}_z^2$ and $\widetilde{H}_\mathrm{p}^2$, it is the ratio $H_\mathrm{p}/\Delta M$ (related to the amplitudes A_H and A_M) which determines the angular anisotropy and the asymptotic power-law dependence of $d\Sigma/d\Omega$ as well as the characteristic length of spin-misalignment fluctuations.

Finally, it is assumed that the nuclear scattering could be described as a ratio of the longitudinal magnetic scattering, denoted as α. Generally (if the nuclear correlation length ξ_nuc is different from ξ_M) α is a function of q. Here, no particular ξ_nuc is defined and and it is assumed to be contained in $\alpha(q)$:

$$\widetilde{N}^2(q\xi_\mathrm{nuc}) = \alpha(q) b_\mathrm{H}^2 \widetilde{M}_z^2(q\xi_\mathrm{M}). \tag{5.25}$$

Of course, other scattering functions such as the form factor of a sphere and various structure-factor models (*e.g.* a Percus-Yevick hard-sphere structure factor) can be straightforwardly implemented [77].

Finally, given theoretical models (or experimental data) for the longitudinal magnetization Fourier component $\widetilde{M}_z(\mathbf{q})$ and for the nuclear scattering amplitude $\widetilde{N}(\mathbf{q})$, the corresponding terms in the SANS cross sections (see section 5.3) and, hence, in the final polarizations could be straight-forwardly computed.

5.5 First experimental results on NANOPERM

5.5.1 Neutron samples and experimental details

The neutron data presented further originates from [47]. The sample under study was a two-phase magnetic nanocomposite from the NANOPERM family of alloys [118] with a nominal composition of $(Fe_{0.985}Co_{0.015})_{90}Zr_7B_3$ [119]. The alloy was prepared by melt spinning, followed by an annealing treatment for 1 h at 883 K, which resulted in the precipitation of b.c.c. iron nanoparticles in an amorphous magnetic matrix. The average iron particle size of $D = 15 \pm 2$ nm was determined by the analysis of wide-angle x-ray diffraction data [47]. The crystalline particle volume fraction is about 65 % and the saturation magnetization is $\mu_0 M_0 = 1.64$ T. The exchange-stiffness constant $A = (4.7 \pm 0.9) \times 10^{-12}$ J/m has been previously determined by the analysis of the field-dependent unpolarized SANS cross section [47]. For the SANS experiments, several circular discs with a diameter of 10 mm and a thickness of about 20 μm were stacked and mounted on a Cd aperture (for further details see [82, 47]).

The polarized neutron experiment was carried out at room temperature at the D22 instrument at the Institut Laue-Langevin, Grenoble, France. Incident neutrons with a mean wavelength of $\lambda = 8$ and a wavelength spread of $\Delta\lambda/\lambda = 10\,\%$ (FWHM) were used. The beam was polarized using a 1.2 m-long remanent Fe-Si supermirror transmission polarizer, installed immediately after the velocity selector. A radio-frequency spin flipper, installed close to the sample position, allowed the reversal of the initial neutron polarization. The external magnetic field was provided by an electromagnet and was applied perpendicular to the wave vector $\mathbf{k}_0$ of the incident neutrons. Measurement of the four partial POLARIS cross sections $d\Sigma^{++}/d\Omega$, $d\Sigma^{--}/d\Omega$, $d\Sigma^{+-}/d\Omega$, and $d\Sigma^{-+}/d\Omega$ was accomplished through a polarized ^{3}He spin-filter cell, installed inside the detector housing, about 1 m away from the sample position. The polarization between polarizer, flipper, and ^{3}He filter was maintained by magnetic guide fields on the order of 1 mT. The efficiencies of the polarizer, spin flipper, and ^{3}He analyzer were, respectively, 90 %, 99 %, and 87.5 %. The scattered neutrons

were detected by a multi-tube detector consisting of 128×128 pixels with a resolution of $8 \times 8\,\mathrm{mm}$. Neutron data reduction, including corrections for background scattering and spin leakage [127], was performed using the GRASP [23] and BerSANS [56] software packages.

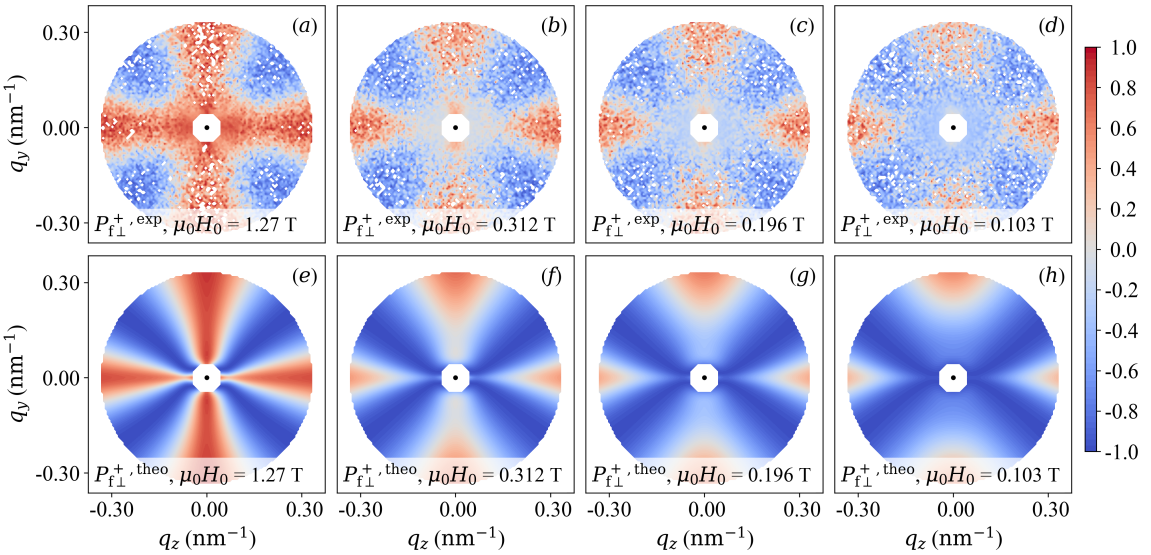

Fig. 5.1 Qualitative comparison between experiment and theory. $(a)-(e)$ Two-dimensional experimental polarization $P_{f\perp}^{+}(\mathbf{q})$ of the scattered neutrons of NANOPERM $[(Fe_{0.985}Co_{0.015})_{90}Zr_7B_3]$ at a series of applied magnetic fields (see insets). $\mathbf{H}_0$ is horizontal in the plane. The range of momentum transfers is restricted to $q \lesssim 0.35\,\mathrm{nm}^{-1}$. $(f)-(j)$ Prediction by the analytical micromagnetic theory (no free parameters) using the experimental ratio $\alpha_{\mathrm{exp}}(q)$, the structural ($\xi_M = \xi_H = D/2 = 7.5\,\mathrm{nm}$) and magnetic (A, M_0) interaction parameters of NANOPERM ([82, 47, 73]). The central white octagons mark the position of the beam stop. Taken from [73].

5.5.2 Intensity maps of the polarisation of the scattered beam

The two-dimensional experimental distribution of the polarization of NANOPERM is depicted in Figure 5.1 ($P_{f\perp}^{+}$) and Figure 5.2 ($P_{f\perp}^{-}$) at selected field values together with the comparison to the polarization based on the micromagnetic SANS theory presented above (see Refs. [82] for some selected spin-resolved SANS cross sections). The simulation uses as the input values the experimental ratio $\alpha_{\mathrm{exp}}(q)$ ([82, 73]), and the structural ($\xi_M = \xi_H = D/2 = 7.5\,\mathrm{nm}$) and magnetic (A, M_0) interaction parameters. In agreement with the previous micromagnetic SANS data analysis of this sample [82, 47], the ratio $A_H/A_M = 0.2$ was set. The overall qualitative agreement between experiment and theory (no free parameters) is evident, although the angular anisotropy of the data does not exhibit a large variation with field. Only at the smallest momentum-transfers can one notice a

change in the anisotropy with decreasing field (in particular in $P_{\mathrm{f}\perp}^{-}$), which is related to the emerging spin-misalignment scattering; compare *e.g.* scattering terms $\propto |\widetilde{M}_y|^2 \cos^4\theta$ and $\propto CT_{yz} \sin\theta\cos\theta$ in equations (5.17) and (5.20).

Additionally, the existence of (seemingly isotropic) scattering contributions at small $q \lesssim 0.1\,\mathrm{nm}^{-1}$ (especially at 1.27 T) is noted, which is likely due to large-scale structures that are not contained in the micromagnetic theory [compare Figure 5.1(a) and (e) and Figure 5.2(a) and (e)].

The 1D fits of the experimental data from Figure 5.1 and Figure 5.2 (*i.e.*, (a)-(d) on both figures) are represented on Figure 5.3. The fits provide a reasonable description of the experimental data. The obtained values for ξ_{M} and ξ_{H} are depicted on Figure 5.4; $\xi_{\mathrm{H}} \cong 6-15\,\mathrm{nm}$ is at all fields comparable with the particle size, while ξ_{M} takes on larger values between about $22-66\,\mathrm{nm}$ and seems to increase with the field. For the exchange-stiffness constant, the best-fit values (from the four local fits) range between $A = (4.8-9.7) \times 10^{-12}\,\mathrm{J/m}$, which agrees very well with data in the literature [47, 6].

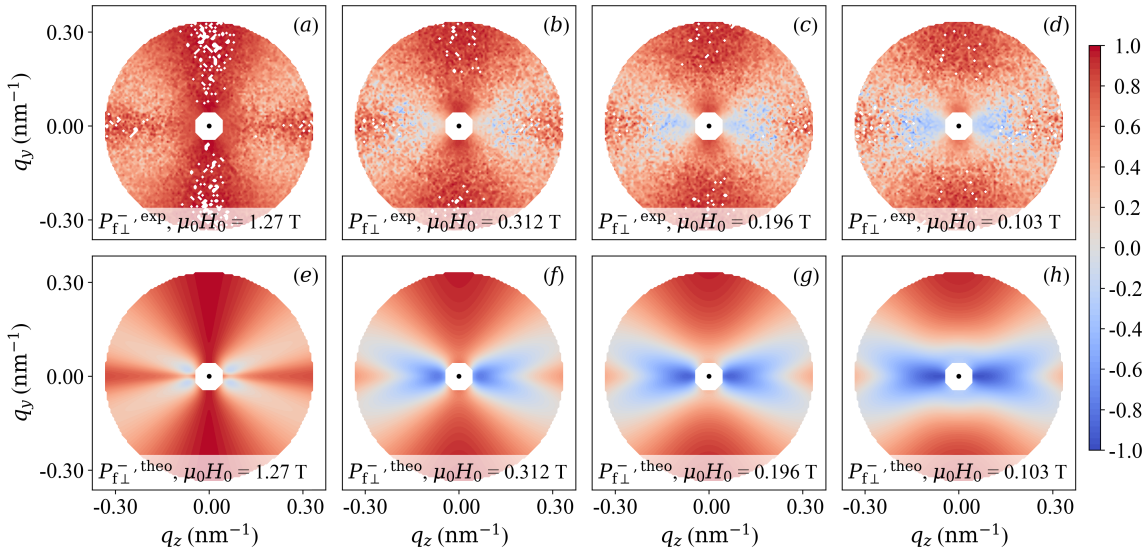

Fig. 5.2 Same as Fig. 5.1, but for $P_{\mathrm{f}\perp}^{-}(\mathbf{q})$. Taken from [73].

5.6 Summary and conclusion

Thus, since the uniaxial polarization analysis is becoming more and more available on SANS instruments worldwide and, in view of the recent seminal progress made regarding several techniques which exploit the neutron polarization to characterize large-scale magnetic structures (SESANS, DFI, SEMSANS), the micromagnetic SANS framework presented here

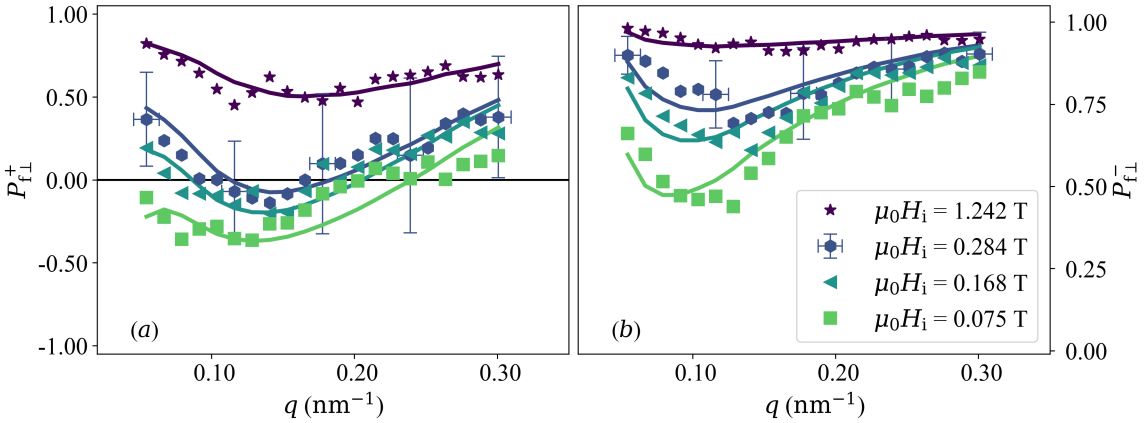

Fig. 5.3 (Data points) Experimental polarizations $P^{+}_{f\perp}(q, \theta = 90°)$ (*a*) and $P^{-}_{f\perp}(q, \theta = 90°)$ (*b*) of the scattered neutrons of NANOPERM $[(Fe_{0.985}Co_{0.015})_{90}Zr_7B_3]$ at a series of applied magnetic fields (see inset). For the general clarity, error bars are shown for one field only. (Solid lines) Prediction by the analytical micromagnetic theory. Note the different scales on the ordinates in (*a*) and (*b*). Taken from [73].

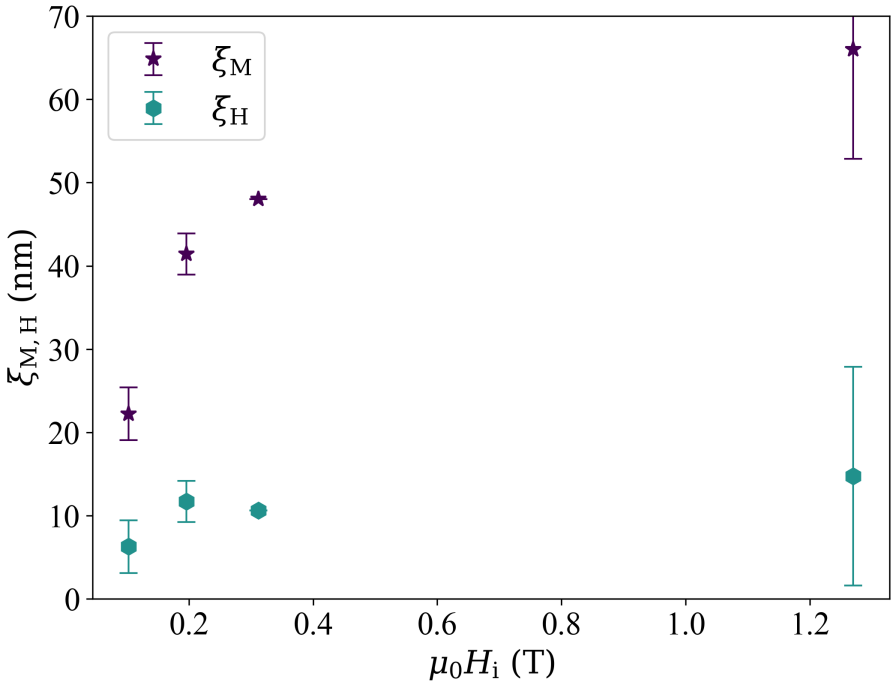

Fig. 5.4 Resulting best-fit values for the correlation lengths ξ_M and ξ_H (see inset). Taken from [73].

and in [73] forms the basis for all of these neutron techniques and open up a new avenue for magnetic neutron data analysis on mesoscopic magnetic systems. This approach provides

information on the magnetic interactions (exchange and DMI constants) and on the spatial structures of the magnetic anisotropy and magnetostatic fields.

Additionally, the anisotropies captured by the theory provide a fairly quick way of assessing the relative contributions of the interactions present, *e.g.* the ratio of amplitudes of anisotropy field fluctuations to magnetization fluctuation, as shown on Figure 5.5. Additional explorations of the phase space could be found in [73].

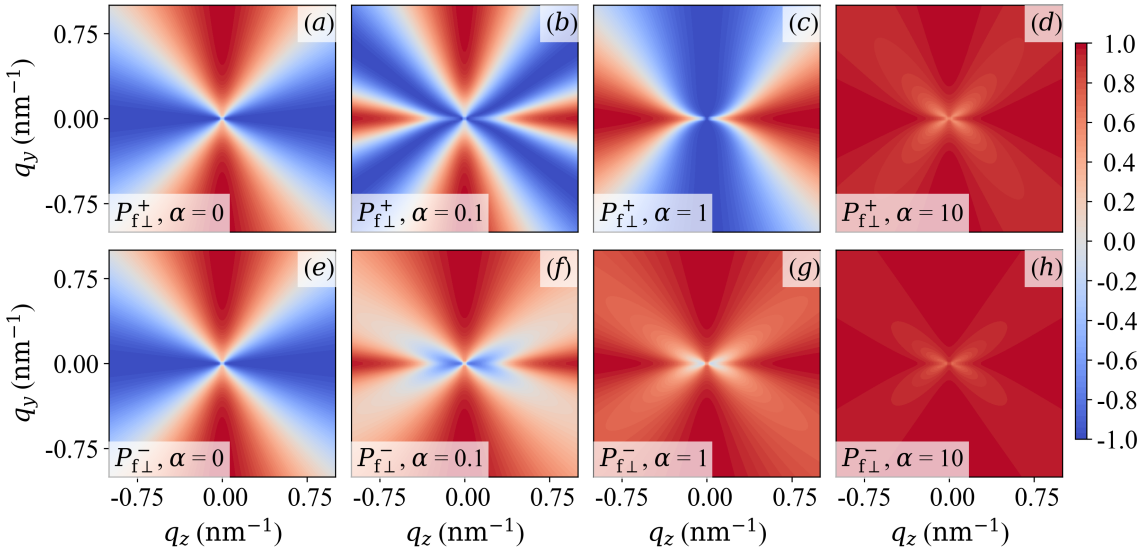

Fig. 5.5 Plot of $P^{+}_{f\perp}(q_y, q_z)$ (upper row) and $P^{-}_{f\perp}(q_y, q_z)$ (lower row) at different values of α (see insets). Taken from the Supplementary Material of [73].

Chapter 6

Summary and outlook

The main aim of this thesis has been to add to the existing methodology and to push the frontiers of the magnetic small-angle neutron scattering (SANS) analysis. From its conception, the project relied on the combination of an analytical approach in terms of the continuum theory of micromagnetics combined with the analysis of the experimental neutron scattering data on magnetic materials. Overall, the results of the study are:

1. The development of the magnetic Guinier law for the analysis of magnetic scattering data on statistically-isotropic magnetic materials.

2. The study of the magnetic correlations in a promising rare-earth-free Mn-Bi-based permanent magnet and its analysis in terms of the generalized Guinier-Porod model.

3. The development of a rigorous framework for the analysis of the neutron polarization of the scattered beam and the testing of existing experimental neutron data.

The magnetic Guinier law introduces the concept of the magnetic Guinier radius (R_{GSM}), which reflects the nature of local magnetization fluctuations. It contains both a field-independent part related to the sample's microstructure (anisotropy-field radius) and a field-dependent part related to the magnetic interactions (exchange constant, saturation magnetization). Moreover, being fully analogous to the conventional Guinier law, the framework provided offers a robust, quick, and straightforward way of treating magnetic neutron scattering data to extract the micromagnetic exchange length or the exchange-stiffness constant. For the original publication on the magnetic Guinier law, the reader is referred to [83]. All the theoretical predictions of the model were verified on several different magnetic materials and in all the cases the material parameters extracted agreed very well with the data in the existing literature, despite the fact the magnetic Guinier law is an entirely new concept

in the magnetic SANS theory. Thus, the outcome of the work presented here advances the analysis methodology and opens up a promising avenue for further studies.

Secondly, the first neutron scattering experiment on Mn – Bi magnets was performed and revealed both the characteristic magnetic sizes and the potential origin for increased coercivity in one of the compositions studied in elongated magnetic structures. Additionally, it was elucidated that in the SANS regime, the field-dependence of the magnetic scattering cross section is very weak, rendering the experimental statistics a major factor for the subsequent data analysis. Nevertheless, a weak anisotropy was observed even in this regime. The majority of the magnetic correlations in this material are realized at a larger length scale, as demonstrated by the analysis using the generalized Guinier-Porod model in the very small-angle regime (VSANS). Further extension of the q-range into the ultra small-angle regime (USANS, with $q_{\mathrm{min}} \cong 10^{-4}\,\mathrm{nm}^{-1}$) could be a potential next step in the study of these materials. For the original neutron study of Mn – Bi permanent magnets the reader is referred to [72]. To the author's knowledge, this is the first neutron study of such a kind, utilizing the strengths of the SANS technique in mapping the magnetic interactions in the bulk and on the mesoscopic length scale. Naturally, it adds to the body of the scientific knowledge on the material and paves the way for further analysis of the fundamental magnetic interactions of rare-earth-free permanent magnets through the neutron lens.

Finally, progress in the polarized neutron instrumentation, more specifically, the development of efficient ^{3}He spin filters, allows the analysis of the polarization of the scattered neutron beam. This is of great importance to the neutron community, since uniaxial polarization analysis has become a routine option on many SANS instruments worldwide. Likewise, real-space neutron techniques that exploit the neutron polarization as a degree of freedom including but not limited to *e.g.*, spin-echo small-angle neutron scattering (SESANS), spin-echo modulated small-angle neutron scattering (SEMSANS), and polarized neutron dark-field contrast imaging (DFI), measuring the projected correlation function and yielding information on large-scale (*i.e.*, beyond the resolution limit of the conventional SANS) magnetic correlations, are on the rise. The here-developed uniaxial SANS polarization framework is rooted in the micromagnetic SANS theory and allows both an easy qualitative analysis on the level of the angular anisotropies (and the respective ranges of ratios of structural and magnetic interaction parameters) and a comprehensive quantitative evaluation of the data. The theory is transferable to the above mentioned real-space methods and might open up a new avenue for their interpretation and exploitation.

References

[1] Adams, E., Hubbard, W. M., and Syeles, A. M. (1952). A new permanent magnet from powdered manganese bismuthide. *Journal of Applied Physics*, 23(11):1207–1211.

[2] Aharoni, A. (1996). *Introduction to the Theory of Ferromagnetism*. Clarendon Press, Oxford, 2nd edition. chapter 6.

[3] Baker, I. (2015). Manganese-based permanent magnets. *Metals*, 5(3):1435–1436.

[4] Batz, M., Baessler, S., Heil, W., Otten, E., Rudersdorf, D., Schmiedeskamp, J., Sobolev, Y., and Wolf, M. (2005). He-3 spin filter for neutrons. *Journal of Research of the National Institute of Standards and Technology*, 110(3):293.

[5] Bender, P., Bogart, L. K., Posth, O., Szczerba, W., Rogers, S. E., Castro, A., Nilsson, L., Zeng, L. J., Sugunan, A., Sommertune, J., Fornara, A., González-Alonso, D., Barquín, L. F., and Johansson, C. (2017). Structural and magnetic properties of multi-core nanoparticles analysed using a generalised numerical inversion method. *Scientific Reports*, 7(1):45990.

[6] Bersweiler, M., Adams, M. P., Peral, I., Kohlbrecher, J., Suzuki, K., and Michels, A. (2022). Unraveling the magnetic softness in Fe–Ni–B-based nanocrystalline material by magnetic small-angle neutron scattering. *IUCrJ*, 9(1):65–72.

[7] Bick, J.-P., Suzuki, K., Gilbert, E. P., Forgan, E. M., Schweins, R., Lindner, P., Kübel, C., and Michels, A. (2013). Exchange-stiffness constant of a Nd-Fe-B based nanocomposite determined by magnetic neutron scattering. *Applied Physics Letters*, 103(12):122402.

[8] Blume, M. (1963). Polarization Effects in the Magnetic Elastic Scattering of Slow Neutrons. *Physical Review*, 130(5):1670–1676.

[9] Borgia, A., Zheng, W., Buholzer, K., Borgia, M. B., Schüler, A., Hofmann, H., Soranno, A., Nettels, D., Gast, K., Grishaev, A., Best, R. B., and Schuler, B. (2016). Consistent View of Polypeptide Chain Expansion in Chemical Denaturants from Multiple Experimental Methods. *Journal of the American Chemical Society*, 138(36):11714–11726.

[10] Brown, P. (2006). Chapter 5 - Spherical Neutron Polarimetry. In Chatterji, T., editor, *Neutron Scattering from Magnetic Materials*, pages 215–244. Elsevier Science, Amsterdam.

[11] Brown Jr., W. F. (1963). *Micromagnetics*. Interscience Publishers, New York.

[12] Brückel, T. (2017). 2. A neutron primer: Elastic scattering and the properties of the neutron. In *21. JCNS Neutron Lab Course*.

[13] Burke, S. K. (1981). Magnetic small-angle neutron scattering from ferromagnetic fine particles: modification of the Guinier law. *Journal of Physics F: Metal Physics*, 11(3):L53–L58.

[14] Byrne, J. (1994). *Neutrons, Nuclei, and Matter: An Exploration of the Physics of Slow Neutrons*. Institute of Physics Pub.

[15] Cao, J., Huang, Y. L., Hou, Y. H., Shi, Z. Q., Yan, X. T., Zhong, Z. C., and Wang, G. P. (2019). Microstructure and magnetic properties of MnBi alloys with high coercivity and significant anisotropy prepared by surfactant assisted ball milling. *Journal of Magnetism and Magnetic Materials*, 473(October):505–510.

[16] Chen, Y. C., Gregori, G., Leineweber, A., Qu, F., Chen, C. C., Tietze, T., Kronmüller, H., Schütz, G., and Goering, E. (2015). Unique high-temperature performance of highly condensed MnBi permanent magnets. *Scripta Materialia*, 107:131–135.

[17] Chen, Y. C., Sawatzki, S., Ener, S., Sepehri-Amin, H., Leineweber, A., Gregori, G., Qu, F., Muralidhar, S., Ohkubo, T., Hono, K., Gutfleisch, O., Kronmüller, H., Schütz, G., and Goering, E. (2016). On the synthesis and microstructure analysis of high performance MnBi. *AIP Advances*, 6(12):125301.

[18] Coey, J. M. (2012). Permanent magnets: Plugging the gap. *Scripta Materialia*, 67(6):524–529.

[19] Coey, J. M. D. (2014). New permanent magnets; manganese compounds. *Journal of Physics: Condensed Matter*, 26(6):064211.

[20] Cui, J., Choi, J. P., Li, G., Polikarpov, E., Darsell, J., Overman, N., Olszta, M., Schreiber, D., Bowden, M., Droubay, T., Kramer, M. J., Zarkevich, N. A., Wang, L. L., Johnson, D. D., Marinescu, M., Takeuchi, I., Huang, Q. Z., Wu, H., Reeve, H., Vuong, N. V., and Liu, J. P. (2014a). Thermal stability of MnBi magnetic materials. *Journal of Physics: Condensed Matter*, 26(6).

[21] Cui, J., Choi, J. P., Polikarpov, E., Bowden, M. E., Xie, W., Li, G., Nie, Z., Zarkevich, N., Kramer, M. J., and Johnson, D. (2014b). Effect of composition and heat treatment on MnBi magnetic materials. *Acta Materialia*, 79:374–381.

[22] Curcio, C., Olivetti, E., Martino, L., Küpferling, M., and Basso, V. (2015). Study of the Temperature Dependence of Coercivity in MnBi. *Physics Procedia*, 75:1230–1237.

[23] Dewhurst, C. D. (2003 [Online]). Graphical Reduction and Analysis SANS Program for Matlab. ILL. Available online at https://www.ill.eu/users/support-labs-infrastructure/software-scientific-tools/grasp.

[24] Dewhurst, C. D., Grillo, I., Honecker, D., Bonnaud, M., Jacques, M., Amrouni, C., Perillo-Marcone, A., Manzin, G., and Cubitt, R. (2016). The small-angle neutron scattering instrument D33 at the Institut Laue-Langevin. *Journal of Applied Crystallography*, 49:1–14.

[25] Enderle, M. (2014). Neutrons and magnetism. *École thématique de la Société Française de la Neutronique*, 13:01002.

[26] Ener, S., Skokov, K. P., Karpenkov, D. Y., Kuz'min, M. D., and Gutfleisch, O. (2015). Magnet properties of $Mn_{70}Ga_{30}$ prepared by cold rolling and magnetic field annealing. *Journal of Magnetism and Magnetic Materials*, 382:265–270.

[27] Feigin, L. A. and Svergun, D. I. (1987). *Structure Analysis by Small-Angle X-Ray and Neutron Scattering*. Plenum Press, New York.

[28] Fritz, G. and Glatter, O. (2006). Structure and interaction in dense colloidal systems: evaluation of scattering data by the generalized indirect Fourier transformation method. *Journal of Physics: Condensed Matter*, 18(36):S2403–S2419.

[29] Fritz-Popovski, G., Bergmann, A., and Glatter, O. (2011). Real space functions from experimental small angle scattering data. *Physical Chemistry Chemical Physics*, 13(13):5872.

[30] Gille, W. (2014). *Particle and Particle Systems Characterization: Small-Angle Scattering (SAS) Applications*. CRC Press, Boca Raton.

[31] Glatter, O. (1982). Chapter 5. Interpretation. In Glatter, O. and Kratky, O., editors, *Small Angle X-ray Scattering*, pages 167–196. Academic Press, London.

[32] Glatter, O. and (editors), O. K. (1982). *Small Angle X-ray Scattering*. Academic Press, London.

[33] Goll, D. (2007). Magnetization processes and the microstructure. In Kronmüller, H. and Parkin, S., editors, *Handbook of Magnetism and Advanced Magnetic Materials*, pages 1023–1058. Wiley, Chichester, Volume 2: Micromagnetism edition.

[34] Grigoriev, S. V., Sukhanov, A. S., Altynbaev, E. V., Siegfried, S.-A., Heinemann, A., Kizhe, P., and Maleyev, S. V. (2015). Spin waves in full-polarized state of Dzyaloshinskii-Moriya helimagnets: Small-angle neutron scattering study. *Physical Review B*, 92(22):220415.

[35] Grillo, I. (2008). Small-Angle Neutron Scattering and Applications in Soft Condensed Matter. In *Soft Matter Characterization*, pages 723–782. Springer Netherlands, Dordrecht.

[36] Guinier, A. and Fournet, G. (1955). *Small-Angle Scattering of X-rays*. Wiley, New York.

[37] Guinier, A., Fournet, G., and Yudowitch, K. L. (1955). *Small-angle scattering of X-rays*. Wiley New York, New York. chapter 2.

[38] Gutfleisch, O. (2021). Permanent Magnets for Efficient Energy Conversion. In *The European School on Magnetism 2021: From fundamental properties of matter to magnetic materials and applications*.

[39] Gutfleisch, O., Willard, M. A., Brück, E., Chen, C. H., Sankar, S. G., and Liu, J. P. (2011). Magnetic materials and devices for the 21st century: Stronger, lighter, and more energy efficient. *Advanced Materials*, 23(7):821–842.

[40] Halpern, O. and Johnson, M. H. (1939). On the Magnetic Scattering of Neutrons. *Physical Review*, 55(10):898–923.

[41] Hammouda, B. (2008). Insight into the SANS Technique. *National Institute of Standards and Technology*, pages 1–717.

[42] Hammouda, B. (2010). A new Guinier–Porod model. *Journal of Applied Crystallography*, 43(4):716–719.

[43] Hirai, M. (2011). Contrast Variation. In *Neutrons in Soft Matter*, pages 351–382. John Wiley & Sons, Inc., Hoboken, NJ, USA.

[44] Holmes, A. T., Walsh, G. R., Blackburn, E., Forgan, E. M., and Savey-Bennett, M. (2012). A 17 T horizontal field cryomagnet with rapid sample change designed for beamline use. *Review of Scientific Instruments*, 83(2):023904.

[45] Honecker, D., Döbrich, F., Dewhurst, C. D., Wiedenmann, A., and Michels, A. (2011). Neutron spin-flip scattering of nanocrystalline cobalt. *Journal of Physics: Condensed Matter*, 23(1).

[46] Honecker, D., Ferdinand, A., Döbrich, F., Dewhurst, C. D., Wiedenmann, A., Gómez-Polo, C., Suzuki, K., and Michels, A. (2010). Longitudinal polarization analysis in small-angle neutron scattering. *European Physical Journal B*, 76(2):209–213.

[47] Honecker, D. and Michels, A. (2013). Theory of magnetic small-angle neutron scattering of two-phase ferromagnets. *Physical Review B*, 87(22):1–10.

[48] Ibel, K. (1976). The neutron small-angle camera D11 at the high-flux reactor, Grenoble. *Journal of Applied Crystallography*, 9(4):296–309.

[49] ISIS, S. (2015). ISIS Staying safe in the skies. Available online at https://www.isis.stfc.ac.uk/Pages/Staying-safe-in-the-skies.aspx.

[50] Janotová, I., Švec, P., Maťko, I., Janičkovič, D., and Sr., P. Š. (2018a). Evolution and degradation of magnetic MnBi phase. In *AIP Conference Proceedings*, volume 1996, page 020021.

[51] Janotová, I., Švec, P., Švec, P., Maťko, I., Janičkovič, D., Kunca, B., Marcin, J., and Škorvánek, I. (2018b). Formation of magnetic phases in rapidly quenched Mn-Based systems. *Journal of Alloys and Compounds*, 749:128–133.

[52] Jericha, E., Badurek, G., and Gösselsberger, C. (2013). Towards a Modelling of USANSPOL Intensities from Magnetic Ribbons. *Physics Procedia*, 42:58–65.

[53] Jericha, E., Badurek, G., Gösselsberger, C., and Süss, D. (2012). Experimental and methodic progress in ultra-small-angle polarised neutron scattering on novel magnetic materials. *Journal of Physics: Conference Series*, 340:012007.

[54] Jia, Y., Wu, Y., Zhao, S., Zuo, S., Skokov, K. P., Gutfleisch, O., Jiang, C., and Xu, H. (2020). $L1_0$ rare-earth-free permanent magnets: The effects of twinning versus dislocations in Mn-Al magnets. *Physical Review Materials*, 4(9):094402.

[55] Jian, H., Skokov, K. P., and Gutfleisch, O. (2015). Microstructure and magnetic properties of Mn–Al–C alloy powders prepared by ball milling. *Journal of Alloys and Compounds*, 622:524–528.

[56] Keiderling, U. (2002). The new 'BerSANS-PC' software for reduction and treatment of small angle neutron scattering data. *Applied Physics A: Materials Science & Processing*, 74(SUPPL.II):s1455–s1457.

[57] Keiderling, U., Wiedenmann, A., Rupp, A., Klenke, J., and Heil, W. (2008). SANS polarization analysis at V4 SANS instrument of HMI Berlin. *Measurement Science and Technology*, 19(3):034009.

[58] Keller, T., Krist, T., Danzig, A., Keiderling, U., Mezei, F., and Wiedenmann, A. (2000). Polarized neutron small-angle scattering instrument at BENSC Berlin. *Nuclear Instruments and Methods in Physics Research, Section A: Accelerators, Spectrometers, Detectors and Associated Equipment*, 451(2):474–479.

[59] Kikhney, A. G. and Svergun, D. I. (2015). A practical guide to small angle X-ray scattering (SAXS) of flexible and intrinsically disordered proteins. *FEBS Letters*, 589(19PartA):2570–2577.

[60] Kim, S., Moon, H., Jung, H., Kim, S. M., Lee, H. S., Choi-Yim, H., and Lee, W. (2017). Magnetic properties of large-scaled MnBi bulk magnets. *Journal of Alloys and Compounds*, 708:1245–1249.

[61] Kostorz, G. (1982). 14. Inorganic substances. In Glatter, O. and Kratky, O., editors, *Small Angle X-ray Scattering*, pages 467–498. Academic Press, London.

[62] Kronmüller, H. and Fähnle, M. (2003). *Micromagnetism and the Microstructure of Ferromagnetic Solids*. Cambridge University Press, Cambridge.

[63] Krycka, K., Chen, W., Borchers, J., Maranville, B., and Watson, S. (2012). Polarization-analyzed small-angle neutron scattering. I. Polarized data reduction using Pol-Corr. *Journal of Applied Crystallography*, 45(3):546–553.

[64] Kuz'Min, M. D., Skokov, K. P., Jian, H., Radulov, I., and Gutfleisch, O. (2014). Towards high-performance permanent magnets without rare earths. *Journal of Physics: Condensed Matter*, 26(6).

[65] Lang, P. and Glatter, O. (1996). Small-Angle X-ray Scattering from Aqueous Solutions of Tetra(oxyethylene)-*n*-octyl Ether. *Langmuir*, 12(5):1193–1198.

[66] Lovesey, S. W. (1984). *Theory of Neutron Scattering from Condensed Matter*, volume II. Clarendon Press, Oxford.

[67] Lowe, M., Golini, R., and Gereffi, G. (2010). U . S . Adoption of High-Efficiency Motors and Drives : Lessons Learned. *Center on Globalization, Governance and Competitiveness*, page 55.

[68] Ly, V., Wu, X., Smillie, L., Shoji, T., Kato, A., Manabe, A., and Suzuki, K. (2014). Low-temperature phase MnBi compound: A potential candidate for rare-earth free permanent magnets. *Journal of Alloys and Compounds*, 615(S1):S285–S290.

[69] Maleev, S. V. (2002). Polarized neutron scattering in magnets. *Physics-Uspekhi*, 45(6):569–596.

[70] Maleev, S. V., Bar'yakhtar, V. G., and Suris, R. A. (1963). The scattering of slow neutrons by complex magnetic structures. *Soviet Physics-Solid State (English Transl.)*, 4.

[71] Malyeyev, A. and Michels, A. (2019). Magnetic guinier law. In *Proceedings of the 2019 MLZ Conference: Neutrons for information and quantum technologies*, page 20. MLZ.

[72] Malyeyev, A., Titov, I., Bender, P., Bersweiler, M., Pipich, V., Mühlbauer, S., Ener, S., Gutfleisch, O., and Michels, A. (2021). Neutron study of magnetic correlations in rare-earth-free Mn-Bi magnets. *Physical Review Materials*, 5(3):034407.

[73] Malyeyev, A., Titov, I., Dewhurst, C., Suzuki, K., Honecker, D., and Michels, A. (2022). Uniaxial polarization analysis of bulk ferromagnets: theory and first experimental results. *Journal of Applied Crystallography*, 55(3).

[74] Messiah, A. (1990). *Quantenmechanik, Bd. 2*. Walter de Gruyter, Berlin.

[75] Metlov, K. L. and Michels, A. (2015). Third-order effect in magnetic small-angle neutron scattering by a spatially inhomogeneous medium. *Physical Review B*, 91(5).

[76] Mettus, D., Deckarm, M., Leibner, A., Birringer, R., Stolpe, M., Busch, R., Honecker, D., Kohlbrecher, J., Hautle, P., Niketic, N., Fernández, J. R., Barquín, L. F., and Michels, A. (2017). Magnetic small-angle neutron scattering on bulk metallic glasses: A feasibility study for imaging displacement fields. *Physical Review Materials*, 1(7):074403.

[77] Mettus, D. and Michels, A. (2015). Small-angle neutron scattering correlation functions of bulk magnetic materials. *Journal of Applied Crystallography*, 48:1437–1450.

[78] Michels, A. (2014). Magnetic small-angle neutron scattering of bulk ferromagnets. *Journal of Physics: Condensed Matter*, 26(38):383201.

[79] Michels, A. (2021). *Magnetic Small-Angle Neutron Scattering*. Oxford University Press.

[80] Michels, A. and Bick, J.-P. (2013). Autocorrelation function of the spin misalignment in magnetic small-angle neutron scattering: application to nanocrystalline metals. *Journal of Applied Crystallography*, 46(3):788–790.

[81] Michels, A., Erokhin, S., Berkov, D., and Gorn, N. (2014). Micromagnetic simulation of magnetic small-angle neutron scattering from two-phase nanocomposites. *Journal of Magnetism and Magnetic Materials*, 350:55–68.

[82] Michels, A., Honecker, D., Döbrich, F., Dewhurst, C. D., Suzuki, K., and Heinemann, A. (2012). Observation of cross-shaped anisotropy in spin-resolved small-angle neutron scattering. *Physical Review B*, 85(18):184417.

[83] Michels, A., Malyeyev, A., Titov, I., Honecker, D., Cubitt, R., Blackburn, E., and Suzuki, K. (2020). Magnetic Guinier law. *IUCrJ*, 7(1):136–142.

[84] Michels, A., Mettus, D., Honecker, D., and Metlov, K. L. (2016). Effect of Dzyaloshinski-Moriya interaction on elastic small-angle neutron scattering. *Physical Review B*, 94(5):054424.

[85] Michels, A., Mettus, D., Titov, I., Malyeyev, A., Bersweiler, M., Bender, P., Peral, I., Birringer, R., Quan, Y., Hautle, P., Kohlbrecher, J., Honecker, D., Fernández, J. R., Barquín, L. F., and Metlov, K. L. (2019). Microstructural-defect-induced Dzyaloshinskii-Moriya interaction. *Physical Review B*, 99(1):014416.

[86] Michels, A., Viswanath, R. N., Barker, J. G., Birringer, R., and Weissmüller, J. (2003). Range of magnetic correlations in nanocrystalline soft magnets. *Physical Review Letters*, 91(26):1–4.

[87] Michels, A. and Weissmüller, J. (2008). Magnetic-field-dependent small-angle neutron scattering on random anisotropy ferromagnets. *Reports on Progress in Physics*, 71(6):066501.

[88] Michels, A., Weissmüller, J., Wiedenmann, A., Pedersen, J. S., and Barker, J. G. (2000). Measuring the exchange-stiffness constant of nanocrystalline solids by elastic small-angle neutron scattering. *Philosophical Magazine Letters*, 80(12):785–792.

[89] Mitsui, Y., Abematsu, K. I., Umetsu, R. Y., Takahashi, K., and Koyama, K. (2016). Magnetic field effects on liquid-phase reactive sintering of MnBi. *Journal of Magnetism and Magnetic Materials*, 400:304–306.

[90] Moon, R. M., Riste, T., and Koehler, W. C. (1969). Polarization Analysis of Thermal-Neutron Scattering. *Physical Review*, 181(2):920–931.

[91] Mühlbauer, S., Heinemann, A., Wilhelm, A., Karge, L., Ostermann, A., Defendi, I., Schreyer, A., Petry, W., and Gilles, R. (2016). The new small-angle neutron scattering instrument SANS-1 at MLZ—characterization and first results. *Nuclear Instruments and Methods in Physics Research Section A: Accelerators, Spectrometers, Detectors and Associated Equipment*, 832:297–305.

[92] Mühlbauer, S., Honecker, D., Périgo, É. A., Bergner, F., Disch, S., Heinemann, A., Erokhin, S., Berkov, D., Leighton, C., Eskildsen, M. R., and Michels, A. (2019). Magnetic small-angle neutron scattering. *Reviews of Modern Physics*, 91(1):015004.

[93] Munter, A. (2021). Neutron scattering lengths and cross sections. Available online at https://www.ncnr.nist.gov/resources/n-lengths/.

[94] Muralidhar, S., Gräfe, J., Chen, Y. C., Etter, M., Gregori, G., Ener, S., Sawatzki, S., Hono, K., Gutfleisch, O., Kronmüller, H., Schütz, G., and Goering, E. J. (2017). Temperature-dependent first-order reversal curve measurements on unusually hard magnetic low-temperature phase of MnBi. *Physical Review B*, 95(2):1–9.

[95] Nguyen, V. V. and Nguyen, T. X. (2018). Effects of microstructures on the performance of rare-earth-free MnBi magnetic materials and magnets. *Physica B: Condensed Matter*, 532(June):103–107.

[96] Nguyen, V. V., Poudyal, N., Liu, X. B., Liu, J. P., Sun, K., Kramer, M. J., and Cui, J. (2014). Novel processing of high-performance MnBi magnets. *Materials Research Express*, 1(3):036108.

[97] Niarchos, D., Giannopoulos, G., Gjoka, M., Sarafidis, C., Psycharis, V., Rusz, J., Edström, A., Eriksson, O., Toson, P., Fidler, J., Anagnostopoulou, E., Sanyal, U., Ott, F., Lacroix, L.-M., Viau, G., Bran, C., Vazquez, M., Reichel, L., Schultz, L., and Fähler, S. (2015). Toward Rare-Earth-Free Permanent Magnets: A Combinatorial Approach Exploiting the Possibilities of Modeling, Shape Anisotropy in Elongated Nanoparticles, and Combinatorial Thin-Film Approach. *JOM*, 67(6):1318–1328.

[98] Okudaira, T., Oku, T., Ino, T., Hayashida, H., Kira, H., Sakai, K., Hiroi, K., Takahashi, S., Aizawa, K., Endo, H., Endo, S., Hino, M., Hirota, K., Honda, T., Ikeda, K., Kakurai, K., Kambara, W., Kitaguchi, M., Oda, T., Ohshita, H., Otomo, T., Shimizu, H., Shinohara, T., Suzuki, J., and Yamamoto, T. (2020). Development and application of a ^{3}He Neutron Spin Filter at J-PARC. *Nuclear Instruments and Methods in Physics Research Section A: Accelerators, Spectrometers, Detectors and Associated Equipment*, 977:164301.

[99] Osborn, J. A. (1945). Demagnetizing Factors of the General Ellipsoid. *Physical Review*, 67(11-12):351–357.

[100] Park, J., Hong, Y.-K., Lee, J., Lee, W., Kim, S.-G., and Choi, C.-J. (2014). Electronic Structure and Maximum Energy Product of MnBi. *Metals*, 4(3):455–464.

[101] Petoukhov, A., Guillard, V., Andersen, K., Bourgeat-Lami, E., Chung, R., Humblot, H., Jullien, D., Lelievre-Berna, E., Soldner, T., Tasset, F., and Thomas, M. (2006). Compact magnetostatic cavity for polarised 3He neutron spin filter cells. *Nuclear Instruments and Methods in Physics Research Section A: Accelerators, Spectrometers, Detectors and Associated Equipment*, 560(2):480–484.

[102] Pipich, V. (2020). QtiSAS/QtiKWS Visualisation, Reduction, Analysis and Fit Framework with Focus on Small Angle Scattering, http://qtisas.com/about.

[103] Pipich, V. and Fu, Z. (2015). KWS-3: Very small angle scattering diffractometer with focusing mirror. *Journal of large-scale research facilities JLSRF*, 1(0):A31.

[104] Porod, G. (1982). Chapter 2. General theory. In Glatter, O. and Kratky, O., editors, *Small Angle X-ray Scattering*, pages 17–51. Academic Press, London.

[105] Poudyal, N., Liu, X., Wang, W., Nguyen, V. V., Ma, Y., Gandha, K., Elkins, K., Liu, J. P., Sun, K., Kramer, M. J., and Cui, J. (2016). Processing of MnBi bulk magnets with enhanced energy product. *AIP Advances*, 6(5):056004.

[106] Putnam, C. D., Hammel, M., Hura, G. L., and Tainer, J. A. (2007). X-ray solution scattering (SAXS) combined with crystallography and computation: defining accurate macromolecular structures, conformations and assemblies in solution. *Quarterly reviews of biophysics*, 40(3):191–285.

[107] Pynn, R. (1990). Neutron scattering: a primer. *Los Alamos Science*, 19:1–31.

[108] Quan, Y., Kohlbrecher, J., Hautle, P., and Michels, A. (2020). Defect-induced Dzyaloshinskii-Moriya interaction in a nanocrystalline two-phase alloy. *Journal of Physics: Condensed Matter*, 32(28):285804.

[109] Riba, J. R., López-Torres, C., Romeral, L., and Garcia, A. (2016). Rare-earth-free propulsion motors for electric vehicles: A technology review. *Renewable and Sustainable Energy Reviews*, 57:367–379.

[110] Sarkar, A. and Basu Mallick, A. (2020). Synthesizing the Hard Magnetic Low-Temperature Phase of MnBi Alloy: Challenges and Prospects. *JOM*, 72(8):2812–2825.

[111] Schober, H. (2014). An introduction to the theory of nuclear neutron scattering in condensed matter. *Journal of Neutron Research*, 17(3-4):109–357.

[112] Schweizer, J. (2006). Chapter 4 - Polarized Neutrons and Polarization Analysis. In Chatterji, T., editor, *Neutron Scattering from Magnetic Materials*, pages 153–213. Elsevier Science, Amsterdam.

[113] Sears, V. F. (1992). Neutron scattering lengths and cross sections. *Neutron News*, 3(3):26–37.

[114] Skokov, K. P. and Gutfleisch, O. (2018). Heavy rare earth free, free rare earth and rare earth free magnets - Vision and reality. *Scripta Materialia*, 154:289–294.

[115] Skomski, R. (2008). *Simple Models of Magnetism*. Oxford University Press.

[116] Squires, G. L. (1978). *Introduction to the Theory of Thermal Neutron Scattering*. Dover Publications, New York.

[117] Stuhrmann, H. B. (2012). Contrast Variation Application in Small-Angle Neutron Scattering Experiments. *Journal of Physics: Conference Series*, 351(1):012002.

[118] Suzuki, K. and Herzer, G. (2006). Soft Magnetic Nanostructures and Applications. In Sellmyer, D., , and Skomski, R., editors, *Advanced Magnetic Nanostructures*, pages 365–401. Kluwer Academic Publishers, Boston.

[119] Suzuki, K., Makino, A., Inoue, A., and Masumoto, T. (1994). Soft Magnetic Properties of Nanocrystalline Fe-Co-Zr-B Alloys. *Journal of the Magnetics Society of Japan*, 18(3):800–804.

[120] Svergun, D. I. and Koch, M. H. J. (2003). Small-angle scattering studies of biological macromolecules in solution. *Reports on Progress in Physics*, 66(10):1735–1782.

[121] Svergun, D. I., Koch, M. H. J., Timmins, P. A., and May, R. P. (2013). *Small Angle X-Ray and Neutron Scattering from Solutions of Biological Macromolecules*. Oxford Science Publications.

[122] Tangudu, J., Ouyang, G., and Cui, J. (2018). Trade Studies for a Manganese Bismuth based Surface Permanent Magnet Machine. In *2018 IEEE Transportation and Electrification Conference and Expo, ITEC 2018*, pages 442–447. IEEE.

[123] Thoma, H., Hutanu, V., Deng, H., Dmitrienko, V. E., Brown, P. J., Gukasov, A., Roth, G., and Angst, M. (2021). Revealing the Absolute Direction of the Dzyaloshinskii-Moriya Interaction in Prototypical Weak Ferromagnets by Polarized Neutrons. *Physical Review X*, 11(1):11060.

[124] Wang, X. L., An, K., Cai, L., Feng, Z., Nagler, S. E., Daniel, C., Rhodes, K. J., Stoica, A. D., Skorpenske, H. D., Liang, C., Zhang, W., Kim, J., Qi, Y., and Harris, S. J. (2012). Visualizing the chemistry and structure dynamics in lithium-ion batteries by in-situ neutron diffraction. *Scientific Reports*, 2.

[125] Weissmüller, J., McMichael, R. D., Michels, A., and Shull, R. D. (1999). Small-angle neutron scattering by the magnetic microstructure of nanocrystalline ferromagnets near saturation. *Journal of Research of the National Institute of Standards and Technology*, 104(3):261–275.

[126] Weissmüller, J., Michels, A., Barker, J. G., Wiedenmann, A., Erb, U., and Shull, R. D. (2001). Analysis of the small-angle neutron scattering of nanocrystalline ferromagnets using a micromagnetics model. *Physical Review B*, 63(21):2144141–21441418.

[127] Wildes, A. R. (2006). Scientific Reviews: Neutron Polarization Analysis Corrections Made Easy. *Neutron News*, 17(2):17–25.

[128] Williams, W. G. (1988). *Polarized Neutrons*. Clarendon Press, Oxford.

[129] Willis, B. T. M. and Carlile, C. (2009). *Experimental neutron scattering*. Oxford University Press, Oxford.

[130] Xiang, Z., Song, Y., Pan, D., Shen, Y., Qian, L., Luo, Z., Liu, Y., Yang, H., Yan, H., and Lu, W. (2018a). Coercivity enhancement and magnetization process in $Mn_{55}Bi_{45}$ alloys with refined particle size. *Journal of Alloys and Compounds*, 744:432–437.

[131] Xiang, Z., Xu, C., Wang, T., Song, Y., Yang, H., and Lu, W. (2018b). Enhanced magnetization and energy product in isotropic nanocrystalline $Mn_{55}Al_{45}$ alloys with boron doping. *Intermetallics*, 101:13–17.

[132] Zamora, J., Betancourt, I., and Figueroa, I. A. (2018). Switching of Coercivity Process in MnBi Alloys. *Journal of Superconductivity and Novel Magnetism*, 31(3):873–878.

[133] Zheng, W. and Best, R. B. (2018). An Extended Guinier Analysis for Intrinsically Disordered Proteins. *Journal of Molecular Biology*, 430(16):2540–2553.

Appendix A

Additional ageing characterization of Mn – Bi

This Appendix furnishes the rudimentary ageing characterization results on Mn – Bi.

As depicted on Figure A.1(a), the aged sample exhibits a slightly lower saturation magnetization, indicating lower content of the magnetic phase. The Figure A.1(b) supports this notion, showing an increase in the Bi peaks intensity. Yet, even on the studied 2-week time frame the degradation is on the order of 20 % (determined by considering the decrease in the saturation magnetization), thus it was assumed that the bulk of the volume would be affected only marginally in the time frame of a single neutron measurement.

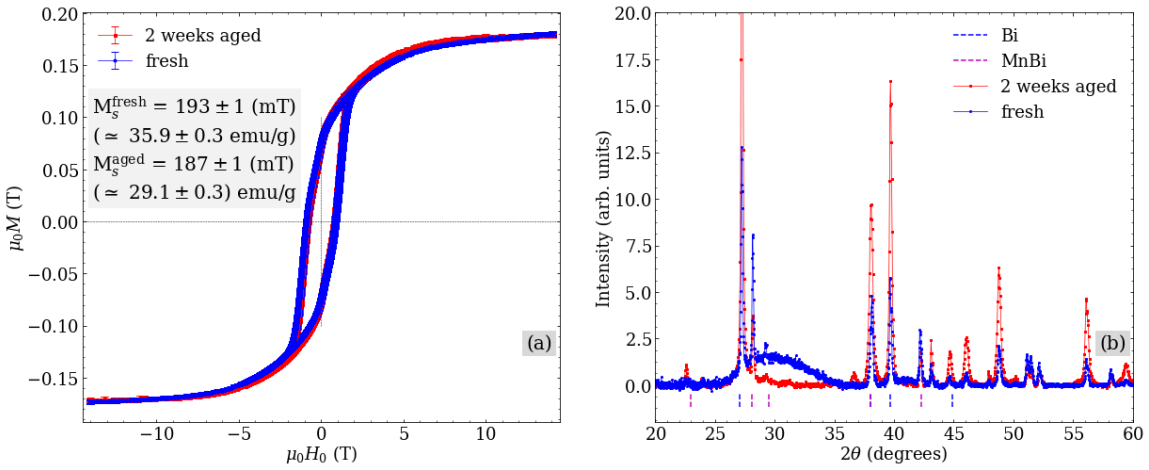

Fig. A.1 Ageing influence on the Mn–Bi samples. (a) Magnetization loop. (b) XRD data.